Dion-Jacobson Naturally Layered Perovskites: Bulk Studies, Ion Exchange and Exfoliation

José Miguel Almeida Pereira
Master in Engineering Physics
Department of Physics and Astronomy
Faculty of Sciences of the University of Porto
Faculty of Engineering of the University of Porto
2025

Dion-Jacobson Naturally Layered Perovskites: Bulk Studies, Ion Exchange and Exfoliation

José Miguel Almeida Pereira

Dissertation carried out as part of the
Master in Engineering Physics
Department of Physics and Astronomy
2025

Supervisor
Prof. Dra. Armandina Maria Lima Lopes,
Principal Investigator, FCUP

Co-supervisor
Prof. Dr. João Pedro Esteves de Araújo,
Associate Professor, FCUP



IFIMUP—IN
Material Physics
Institute of the
University of Porto
Institute of
Nanoscience and
Nanotechnology

Acknowledgements

This thesis is the culmination of more than half a decade's worth of study as an Engineering Physics student at the Faculty of Sciences of the University of Porto (FCUP). I certainly couldn't have reached this far without the support of many friends, colleagues, supervisors and family, to whom I would like to express my gratitute.

First, I'd like to thank the institutions and organizations that welcomed me and provided all the necessary resources for my development as student, namely the Physics and Astronomy Department (DFA) and the Institute of Physics for Advanced Materials, Nanotechnology and Fotonics (IFIMUP). Also FCT for financial support through the projects UIDB/04968/2025 and UIDP/04968/2025 (IFIMUP), and LA/P/0095/2020 (LapMET).

I am deeply grateful to professor Dr. Armandina Lopes and professor Dr. João Pedro Araújo for the opportunity of working under their guidance, and most importantly for their unwavering support and encouragement. Not only have they taught me a lot, but their way of teaching has also been a great source of inspiration throughout my academic journey.

A very special and heartfelt thanks to Dr. Neenu Lekshmi, who accompanied me through countless lab hours, helping me face every trial and tribulation along the way, and providing truly unconditional support. Her knowledge, expertise and patience were absolutely crucial for the realization of this work, and I am profoundly grateful for that. To the rest of the guys from my research group: António Cesário, Pedro Sousa and Pedro Rodrigues; a most sincere thanks for their meaningful contributions, both in and out of the lab, as well as any and all feedback so kindly provided.

I'd also like to thank all the friends I've met in these past six years, many of which might no longer be present in my life, but still have undoubtedly made it possible for me to succeed in my academic endeavors thus far. In particular, to Lucas Almeida, who has been my companion for the last couple of years, consistently helping me pull through some of the most arduous and frustrating moments. Also to Guilherme Rouxinol, whom I've known since my very first year at university, for the long standing friendship and support over all these years.

To my apartment mates, Luís Fernandes and Vitor Barros, for all the fun and joyous moments we've shared while living together, both in and out of the house, and for making me feel at home here in Porto. To Beatriz Galvão as well, with whom I've learned the

meaning of true companionship, and have shared some of the happiest moments in my life for the better part of two and a half years. All the memories we've made will forever be close to my heart.

To my past bandmates from Phase Transition: Fernando Maia, Luís Dias and Sofia Beco. I will always cherish what we've accomplished together, including all the incredible moments I've been lucky to share with them.

Back at home, to all of my life-long friends: Foto, Biju, Hugo, Miguel, Carvalho, Sonecas, Afonso, Kika, Fontes, Tins and many more... It cannot be put into words how fortunate I am for having such an amazing group of friends. More than just saying thanks, I'd like to once again apologize for all the invitations I've denied them for study or work-related reasons, and I vow to make up for it as best I can in the future.

Lastly, but above all else, I would like to thank my close family. From my parents, to my sister Mafalda, as well as my grandparents, cousins and godparents. They are the true bedrock in which I was allowed to stand on and grow. The sacrifices they've made, specially my parents, is something I won't ever be able to repay, but I will certainly dedicate my life to. Making them proud is the greatest honor I can strive for.

Resumo

Após a descoberta de ferroelectricidade híbrida imprópria (HIF) em perovskites naturalmente estratificadas, resultante do acoplamento entre rotações e distorções octaédricas, a família Dion–Jacobson (DJ) destes materiais tem ganho uma atenção significativa na última década. Os compostos $RbNdM_2O_7$ (M = Nb, Ta) são exemplos disso, tendo já sido estabelecidos como catalisadores e foto-catalisadores eficientes. O facto de apresentarem vias para reações de permutação iónica e subsequente esfoliação em nanoestruturas 2D, torna-os altamente relevantes para áreas tecnologicamente avançadas.

Neste trabalho, realizamos um estudo estrutural comparativo destes compostos, recorrendo a Difração de Raios-X (XRD), Espectroscopia Raman e Microscopia Electrónica de Varrimento (SEM). As medições de XRD confirmaram a estrutura polar $I2cm$ reportada para ambos os materiais à temperatura ambiente, enquanto estudos espectrais de Raman forneceram novas evidências claras da transição de fase $I2cm \rightarrow Cmca$ para o $RbNdNb_2O_7$ por volta dos $795\,K$, em concordância com dados de espetroscopia por difração de neutrões encontrados na literatura. Identificámos também a influência do efeito Jahn–Teller de segunda ordem (SOJT) do ião B nas ligação atómicas, dinâmica da rede cristalina e estabilização da fase polar. As imagens de SEM revelaram a morfologia destes compostos a nível microscópico, evidenciando diferenças nos seus processos de nucleação.

A permutação iónica por protões realizada para o $RbNdNb_2O_7$ mostrou resultados positivos, com uma taxa de troca estimada em cerca de 90%, comprovada por alterações observadas nos espectros de XRD e pela análise por Espectroscopia de Raios X por Dispersão de Energia (EDS). Relativamente à esfoliação destes sistemas, foram observadas assinaturas positivas de intercalação utilizando o solvente orgânico hidróxido de tetrabutilamónio. Embora a deposição do material esfoliado se tenha revelado um processo desafiante para obter resultados completamente conclusivos com as técnicas empregues, obtivemos algumas evidências que apoiam o sucesso da esfoliação destas estruturas. Além disso, o trabalho desenvolvido forneceu informação relevante e contributos valiosos que poderão impulsionar desenvolvimentos futuros neste novo tópico de investigação no IFIMUP.

Palavras-chave: Perovskites Naturalmente Estratificadas; Dion-Jacobson; Ferroeletricidade Híbrida Imprópria; Difração Raios-X; Espectroscopia Raman; Microscópio Eletrónico de Varrimento; Protonação; Exfoliação.

Abstract

Following the discovery of Hybrid Improper Ferroelectricity (HIF) in naturally layered oxide perovskites, arising from coupled octahedral tilts and distortions, the Dion-Jacobson (DJ) family of these materials has gained significant attention within the last decade. $RbNdM_2O_7$ (M = Nb, Ta) compounds are notable examples, having been already been established as efficient catalysts and photocatalysts. They also present pathways for ion exchange reactions and exfoliation into 2D-like structures, making them highly demanded for technologically complex areas.

In this work, we perform a comparative structural study on the bulk form of these compounds, by employing X-ray Diffraction (XRD), Raman Spectroscopy and Scanning Electron Microscopy (SEM). XRD measurements confirmed the reported polar $I2cm$ structure for both materials at room temperature, while our Raman spectral studies provided new clear evidence for $I2cm \rightarrow Cmca$ phase transition in $RbNdNb_2O_7$ around $795\,K$, in agreement with neutron diffraction data found in literature. We also identified the influence of the second-order Jahn Teller $(SOJT)$ effect of the B-site ion in governing the bonding environments, lattice dynamics and stabilization of the polar phase. SEM revealed the morphology of these compounds at the microscopic level, pointing to differences in their nucleation processes.

Hydrogen ion exchange performed for $RbNdNb_2O_7$ showed positive results, with an estimated 90% exchange rate, evidenced by changes in XRD spectra and SEM's Energy Dispersive X-ray Spectroscopy (EDS). Regarding the exfoliation of these systems, positive signatures of intercalation were observed with the tetrabutylammonium hydroxide organic solvent. Although the deposition of exfoliated material proved to be a challenging process for obtaining fully conclusive results with the employed techniques, we obtained some evidence supporting the successful exfoliation of these structures. In addition, the work carried out provided relevant information and valuable insights that may drive future developments in this new research top at IFIMUP.

Keywords: Naturally Layered Perovskites; Dion-Jacobson Perovskite; Hybrid Improper Ferroelectricity; X-ray Diffraction; Raman Spectroscopy; Scanning Electron Microscopy; Ion Exchange; Exfoliation.

Table of Contents

List of Figures ix
List of Abbreviations xiii

1. Introduction 1
   1.1. The Perovskite Structure 1
   1.2. Layered Oxide Perovskites 3
      1.2.1. Hybrid Improper Ferroelectricity 3
      1.2.2. Dion-Jacobson Series 5
      1.2.3. $RbNdNb_2O_7$ and $RbNdTa_2O_7$ Systems 6
   1.3. 2D Perovskite Nanosheets 8
      1.3.1. Exfoliation Methods 9
   1.4. Motivation for this Thesis 10
2. Methodology 13
   2.1. Sample Preparation 13
      2.1.1. Solid-State Synthesis 13
      2.1.2. Ion-Exchange 14
      2.1.3. Liquid-Phase Exfoliation 15
   2.2. Sample Characterization 15
      2.2.1. X-ray Diffraction 15
      2.2.2. Raman Spectroscopy 18
      2.2.3. Scanning Electron Microscopy 19
      2.2.4. Heat Capacity Measurements 20
3. Experimental Results 23
   3.1. Characterization - Bulk materials 23
      3.1.1. XRD and Crystal Structure 23
      3.1.2. SEM Imaging 31
      3.1.3. Raman Spectral Studies 34
      3.1.4. Heat Capacity Results 40
   3.2. Hydrogen Ion Exchange 42
   3.3. Exfoliation Attempts and Findings 48
      3.3.1. $RbNdTa_2O_7$-based Samples 48
      3.3.2. $RbNdNb_2O_7$-based Samples 55
4. Conclusions and Future Work 61

Bibliography 62

A. Supporting Information 71
A.1. Raman Temperature Study 71

List of Figures

1.1. **a)** Structural representation of the ABX_3 aristotype $Pm\bar{3}m$ cubic symmetry, depicting the network of corner-sharing BO_6 octahedra, as well as the A and B-site environments; **b)** Relation between the ionic radii values r_A, r_B and r_c and the lattice parameter of the cubic unit cell. Taken from [2]. 1
1.2. **a)** Representation of the ABX_3 $Pbmn$ orthorhombic structure; **b)** Octahedral rotation modes characterized by the irreducible representations M_2^+ and R_5^-, relative to the $Pm\bar{3}m$ cubic phase, and the X_5^- anti-polar displacement mode of the A cations. Taken from [2]. 2
1.3. Layered perovskite families derived from the cubic ABO_3 aristotype. Taken from [12]. 3
1.4. Typical energy versus polarization curves for non-ferroelectric (red), proper ferroelectric (blue) and improper ferroelectric (green) materials. Reversal of one of the distortion modes results in a switch of polarization (green to dashed green, or vice-versa). Taken from [14]. 4
1.5. Layer-resolved polarization of polar orthorhombic $P2_1am$ phase $CsLaNb_2O_7$. The second Cs atom is just for the sake of representation, as there is only one per unit cell. Taken from [15]. 6
1.6. 0.2cmSchematic of the crystal structures adopted by $RbNdTa_2O_7$ and $RbNdNb_2O_7$ as a function of temperature. Magenta, orange, and blue units represent Rb, Nd, and $(Ta,Nb)O_6$ respectively. Green and magenta arrows indicate atomic displacements that lead to local electric dipoles. Taken from [18]. 7
1.7. **a)** Polar $I2cm$ structure adopted by $RbNdNb_2O_7$ at room temperature and corresponding distortion modes. In-phase rotations are denoted by two red circles, while anti-phase ones are shown with a red and a blue circle. Adapted from [20]; **b)** Evolution of $RbNdTa_2O_7$ lattice parameters determined from SXRD data, normalized to those of the $P4/mmm$ symmetry aristotype, as a function of temperature. Red squares indicate the temperatures at which NPD data was collected. Taken from [19]. 8
1.8. Ultrasonic exfoliation process for nanosheet synthesis. Adapted from [34]. 9
1.9. Exfoliation of a layered oxide by osmotic swelling. Taken from [36]. 10

2.1. Schematic of the solid-state synthesis process. Adapted from [2]. 13
2.2. Geometry of Bragg's diffraction. The bold lines represent two parallel Bragg planes separated by a distance d_{hkl}. Adapted from [2]. 16
2.3. Schematic representation of the Bragg-Brentano (left) and Parallel Beam (right) XRD geometries. Taken from [45]. 16
2.4. Different light scattering phenomena (Stokes, Rayleigh and Anti-Stokes), and corresponding energy-state transitions. Taken from [11]. 18
2.5. Interaction of incoming primary electrons with a sample, and depths from which the generated products can escape. Taken from [51]. 20
2.6. **a)** Schematic of the heat capacity hardware; **b)** Heat capacity puck. Taken from [52]. 21

3.1. XRD patterns of each step of the $RbNdNb_2O_7$ synthesis process, starting with the 1st Annealing (top) and ending with the washing step. The reference spectra simulated from the CIF file in the supporting information of [18] is shown at the bottom. 24

3.2. Plot of the observed XRD pattern I_{obs} (after sample washing), refined pattern I_{calc} and respective difference I_{diff} for the synthesized $RbNdNb_2O_7$. 25
3.3. XRD patterns of each step of the $RbNdTa_2O_7$ synthesis process, starting with the 1st Annealing (top) and ending with the washing step. The reference spectra simulated from the CIF file in the supporting information of [18] is shown at the bottom. 27
3.4. Plot of the observed XRD pattern I_{obs} (after sample washing), refined pattern I_{calc} and respective difference I_{diff} for the $I2cm$ phase of $RbNdTa_2O_7$. 28
3.5. Representation of $RbNdNb_2O_7$ and $RbNdTa_2O_7$ crystal structures and their estimated lattice parameters, obtained from the Rietveld refinement of the XRD spectra. Solid lines describe the limits of each unit cell. Drawn with the VESTA software. 29
3.6. Plot of the observed XRD pattern I_{obs}, refined pattern I_{calc} and respective difference I_{diff} for a previously synthesized $RbNdNb_2O_7$ sample. 31
3.7. SEM images captured for $RbNdNb_2O_7$ in powder form (top), at a scale of 20 and $4\,\mu m$. EDS spectrum and measured chemical composition (bottom), including atomic and weight percentage. 32
3.8. SEM images captured for $RbNdTa_2O_7$ in powder form (top), at a scale of 20 and $4\,\mu m$. EDS spectrum and measured chemical composition (bottom), including atomic and weight percentage. 33
3.9. Normalized Raman spectrum of $RbNdNb_2O_7$ measured at ambient temperature. Red lines indicate the peak position of identified vibrational modes. 34
3.10. Temperature evolution of $RbNdNb_2O_7$ Raman spectra. 36
3.11. Normalized Raman spectrum of $RbNdNb_2O_7$ measured at $T = \{300\,;480\,;660\,;840\}\,K$. Modes identified for each spectrum are evidenced by the colored lines. 37
3.12. Peak position of modes F, G, H and R as a function of temperature. Abrupt changes between 790 and $805\,K$ evidence the $I2cm \rightarrow Cmca$ structural transition of $RbNdNb_2O_7$. 38
3.13. Plots of the measured heat capacity for a $RbNdNb_2O_7$ sample (left) and a $RbNdTa_2O_7$ sample (right) in the $[5\,;215$ 40
3.14. Comparison between the overall XRD spectrum (up to 70°) of $RbNdNb_2O_7$ and the one obtained from the powder of its protonated form (i.e. $HNdNb_2O_7$). 42
3.15. Comparison between the XRD spectrum of the $RbNdNb_2O_7$ sample and its protonated form in the 22 to 38° range (left) and 40 to 60° range (right). 43
3.16. Shift of the 002 peak after protonation of the $RbNdNb_2O_7$ sample. For the parent fit $\eta = 1.0$ (full Lorentzian), $b = 0.02$ and $\delta \sim -0.45$. For the protonated sample fit $\eta = 0.6$, $b = 0.01$ and $\delta \sim -0.25$. $m = 0$ in both cases. 45
3.17. Rietveld refinement spectra of the protonated $RbNdNb_2O_7$ sample. 46
3.18. XRD spectra for a dried solution of $RbNdTa_2O_7$ in NMP, and the corresponding supernatant collected after centrifugation, in comparison to its powder form spectrum.49
3.19. Measured Raman spectra of $RbNdTa_2O_7$-based samples: (i) Parent powder form (blue); (ii) Dried NMP solution (orange); (iii) Precipitant from centrifugation (green); and (iv) Precipitant from natural precipitation (red). Images display the spots were the measurement was performed. 50
3.20. SEM images captured for the drop cast supernatant of a $RbNdTa_2O_7$ in NMP solution, dried in a Si substrate. 51
3.21. Laser dispersion test evidencing the presence of suspended exfoliated material in the $RbNdTa_2O_7$ NMP solution's supernatant. 51
3.22. XRD spectra of $RbNdTa_2O_7$ parent powder and natural precipitant from the NMP solution, both measured at University of Minho. 52

3.23. XRD spectra of dried supernatant samples from the $RbNdTa_2O_7$ NMP solution, one with the ”Alumina setup” (red) and the other with regular drop casting (blue). Parent sample spectrum is shown for comparison. 53
3.24. SEM images and EDS spectra of drop cast supernatant from a $RbNdTa_2O_7$ in NMP solution, dried in a glass substrate. 54
3.25. SEM images captured for the supernatant of protonated $RbNdNb_2O_7$ in NMP solution, deposited on a PEI treated Si substrate via dip coating. It showcases the large clusters observed, and a corresponding EDS spectrum. 55
3.26. SEM images captured for the supernatant of protonated $RbNdNb_2O_7$ in NMP solution, deposited on a PEI treated Si substrate via dip coating. It showcases one of many isolated pieces of material found, and a corresponding EDS spectrum. 56
3.27. Raman spectra of the dried precipitant (from centrifugation) of a $HNdNb_2O_7$ in TBAOH solution, in comparison to the spectrum of the phase-pure $RbNdNb_2O_7$ sample. 57
3.28. Light dispersion (Tyndall effect) evidencing the presence of suspended exfoliated material in the $HNdNb_2O_7$ TBAOH solution's supernatant. 58
3.29. Comparison between the overall XRD spectrum (up to 70°) of $RbNdNb_2O_7$ and the one obtained from the dried precipitant of the centrifuged $HNdNb_2O_7$ in TBAOH solution (after exfoliation). 59
3.30. Comparison between the XRD spectrum of the $RbNdNb_2O_7$ sample and dried precipitant of the centrifuged $HNdNb_2O_7$ in TBAOH solution (after exfoliation), in the 23 to 35° range (left) and 37.5 to 57.5^o range (right). 59
3.31. Shift of the [002] peak following from intercalation of TBA^+ radicals between the $NdNb_2O_7$ layers. For the parent fit: $\eta = 0.49$, $b = 0.03$ and $\delta \sim -0.09$. For the intercalated sample: $\eta = 1.0$ (full Lorentzian), $b = 0.01$ and $\delta \sim -0.23$. $m = 0$ in both cases. The same reflection from Hex-RNNO is also shown for comparison. 60

A.1. Fit parameters (frequency, linewidth and amplitude) of selected peaks in the $[100\,;175]$ cm^{-1} region. 71
A.2. Fit parameters (frequency, linewidth and amplitude) of selected peaks in the $[170\,;280]$ cm^{-1} region. 71
A.3. Fit parameters (frequency, linewidth and amplitude) of selected peaks in the $[270\,;315]$ cm^{-1} region. 72
A.4. Fit parameters (frequency, linewidth and amplitude) of selected peaks in the $[300\,;380]$ cm^{-1} region. 72
A.5. Fit parameters (frequency, linewidth and amplitude) of selected peaks in the $[400\,;660]$ cm^{-1} region. 73
A.6. Drift of the O, P and O' vibrational mode frequencies across the temperature range. 73
A.7. Fit parameters (frequency, linewidth and amplitude) of selected peaks in the $[790\,;820]$ cm^{-1} region. 74
A.8. Fit parameters (frequency, linewidth and amplitude) of selected peaks in the $[900\,;955]$ cm^{-1} region. 74

List of Abbreviations

AFM Atomic Force Microscopy. 51

BSEs Backscattered Electrons. 19

DJ Dion-Jacobson. 3

EDS Energy-dispersive X-ray Spectroscopy. 31

HIF Hybrid Improper Ferroelectricity. 5

NLPs Naturally Layered Perovskites. 3

NPD Neutron Powder Diffraction. 6

RNNO $RbNdNb_2O_7$. 6

RNTO $RbNdTa_2O_7$. 6

RP Ruddlesden-Popper. 3

SEM Scanning Electron Microscopy. 13

SEs Secondary Electrons. 19

SOJT Second-Order Jahn-Teller. 1

SXRD Synchrotron X-ray Diffraction. 6

TBAOH Tetrabutylammonium-Hydroxide. 10

TEM Tunneling Electron Microscopy. 51

XRD X-Ray Diffraction. 13

1. Introduction

1.1. The Perovskite Structure

"Perovskite" refers to the name of a crystal structure similar to the homonymous mineral *perovskite*, discovered in the Ural mountains of Russia by Gustav Rose in 1839, and named after the Russian mineralogist Lev Alekseyevich von Perovski (1979 - 1856) [1]. They have the general chemical formula ABX_3, where A is a large cation, B is a small cation and X is an (even smaller) anion. In nature, these materials are most abundantly found in an oxide form, referenced by the formula ABO_3. The crystal structure of the aristotype perovskite oxide belongs to the $Pm\bar{3}m$ (#221) space group, as depicted in Figure 1.1, and can be viewed as a three dimensional network of 8 corner sharing BO_6 octahedra arranged in a cubic shape, with the A cation at its center [2].

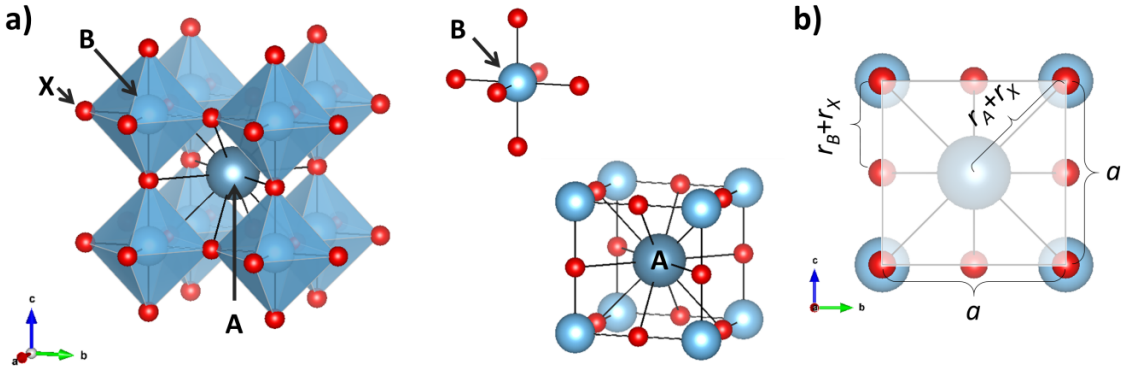

Figure 1.1: **a)** Structural representation of the ABX_3 aristotype $Pm\bar{3}m$ cubic symmetry, depicting the network of corner-sharing BO_6 octahedra, as well as the A and B-site environments; **b)** Relation between the ionic radii values r_A, r_B and r_c and the lattice parameter of the cubic unit cell. Taken from [2].

These A and B sites can be occupied by a large variety of elements, namely alkali, alkaline-earth and rare-earth metals in the first case, and 3d metals in the latter, allowing for a wide range of configurations. This can, in turn, translate to a panoply of interesting physical and chemical properties, such as ferroelectricity and ferromagnetism [3], piezo and pyroelectricity [4], colossal magnetoresistivity [5], photocatalytic properties [6], and so on. Many of these functional properties are strongly influenced, or even enabled, by deviations from the aristotype structure described above, promoted by instabilities in the crystal lattice [7]. These instabilities result in distortions within the system, that fall mostly within 2 distinct groups: octahedral rotations and cation displacements, most commonly attributed to the mismatch in ionic radii, while in other cases driven by a Second-Order

Jahn-Teller (SOJT) effect; and octahedral stretching or flattening, attributed to a first-order Jahn-Teller effect [8].

Victor Moritz Goldschmidt studied the relationship between the relative differences in ionic radii of each ion (r_A, r_B, and r_X) and the structural arrangement and stability of the perovskite structure, describing it in 1926 through a tolerance factor t [9], written as:

$$t = \frac{r_A + r_X}{\sqrt{2}(r_B + r_X)} \tag{1.1}$$

The system will stabilize in the $Pm\bar{3}m$ cubic symmetry when $t \sim 1$. As r_A decreases, the lattice structure changes to a rhombohedral ($0.96 < t < 1$) and then to an orthorhombic ($t < 0.96$) crystal system, wherein the $B - X - B$ bond angle decreases as t decreases. As such, $t < 1$ is accommodated by cooperative rotations of the $BX6$ octahedra, accompanied by a corresponding shift of the A site cations. In order to describe these cooperative rotational distortions, Glazer notation was developed by Jeffrey Glazer in 1972 [10]. Each perovskite structure is characterized in this notation by associating each lattice axis (a, b and c) with one of three superscripts: 0 if there's no rotation; $+$ if the rotation is in-phase; and $-$ if the rotation is anti-phase. Thus, for the highest symmetry aristotype structure we have $a^0a^0a^0$ (only a is used since it is cubic), as there are no tilts or rotations of the octahedra. An example of a distorted ABX_3 structure, with it's distortion modes labeled in

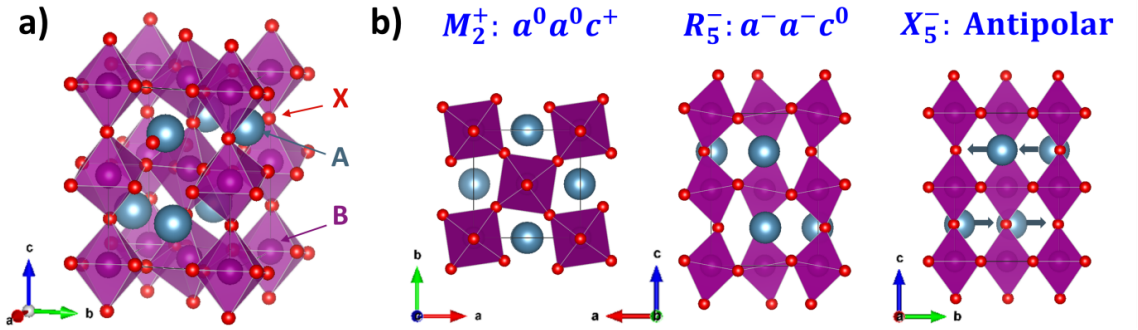

Figure 1.2: **a)** Representation of the ABX_3 $Pbmn$ orthorhombic structure; **b)** Octahedral rotation modes characterized by the irreducible representations M_2^+ and R_5^-, relative to the $Pm\bar{3}m$ cubic phase, and the X_5^- anti-polar displacement mode of the A cations. Taken from [2].

Glazer notation, is shown in Figure 1.2. Furthermore, when $t > 1$, the perovskite structure is destabilized and often transforms into hexagonal or layered structures.

1.2. Layered Oxide Perovskites

Building upon the regular oxide perovskite crystal structure, there are materials in which the three dimensional connectivity of the octahedral network is broken, as layers of perovskite are periodically interleaved with an oxide layer [11]. In particular, many of these materials can be naturally occurring, denoting them as Naturally Layered Perovskites (NLPs). Depending upon the structural arrangement of each system, NLPs can be categorized in different families [2]. Among them the most notable ones are: Dion-Jacobson (DJ) $A'[A_{n-1}B_nO_{3n+1}]$ series, where $n > 1$ is the number of stacked perovskite layers in between the metal oxide ones; the Double Perovskite $AA'BB'O_6$ series; the Ruddlesden-Popper (RP) $A_{n+1}B_nO_{3n+1}$ series; and the Aurivillius $Bi_2O_2[A_{n-1}B_nO_{3n+1}]$ series. Representative examples of the these structure families are shown in Figure 1.3. In contrast

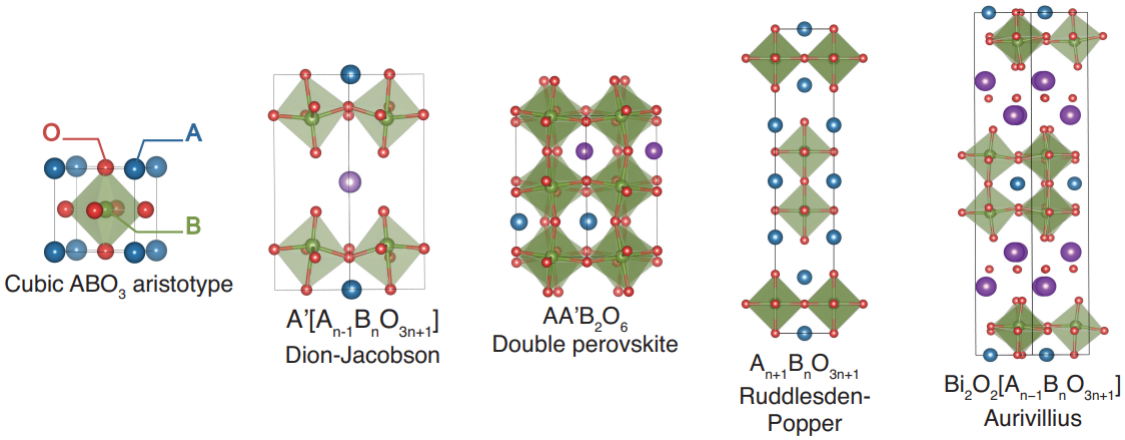

Figure 1.3: Layered perovskite families derived from the cubic ABO_3 aristotype. Taken from [12].

to ABO_3 perovskites, polar and ferroelectric phases are much more common in layered perovskites [12]. As an example, the $Ca_3X_2O_7$ (X = Ti, Mn, Ru) RP phases are all polar, while their $CaXO_3$ parent counterparts are not. The disconnected octahedral layers in these materials make them much more fertile for functional properties and, as a result, newer properties not found in regular perovskites may arise, such as the one described in the following subsection.

1.2.1 Hybrid Improper Ferroelectricity

Perhaps the most notable property of perovskite-like materials is their ability to display a spontaneous macroscopic polarization, switchable by the application of an external electric field, or ferroelectricity in short [13]. At high temperatures, the ABO_3 structure

will present itself in the aforementioned non-polar, paraelectric aristotype form. However, as the temperature decreases, it undergoes phase transitions toward polar, non-centrosymmetric ferroelectric phases [11]. The loss of inversion symmetry can be approached by treating the electric polarization P (resulting from displacements) as an order parameter [12], and expanding the free energy $\mathcal{F}$ of the paraelectric phase in powers of P to the 4th order:

$$\mathcal{F} = \mathcal{F}_0 + \alpha P^2 + \beta P^4 \tag{1.2}$$

where $\mathcal{F}_0$ is the energy of the undistorted phase, and α and β are coefficients. For $\alpha < 0$ (below the Curie temperature), Equation (1.2) produces a double-well potential energy curve (Figure 1.4), and in such cases we're in the presence of a proper ferroelectric. This is of course symmetric, in that we have two equivalent states with oppositely oriented polarizations. On the other hand, the polarization may be coupled to another cooperative displacement pattern, becoming a secondary order parameter (i.e. the spontaneous polarization occurs as a secondary effect) in the ferroelectric transitions, in this case the material is said to be an improper ferroelectric. The free energy of typical improper ferroelectrics contain a linear term in P that acts as an effective electric field, such that they exhibit a single-well minimum shifted to a non-zero value of P.

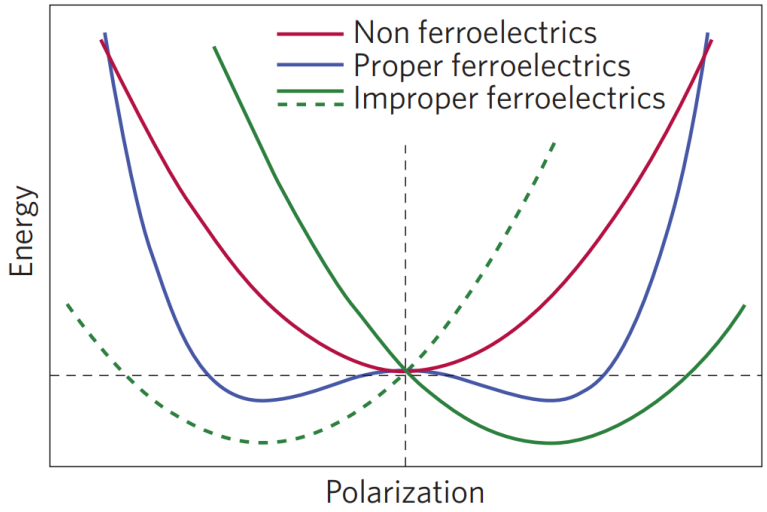

Figure 1.4: Typical energy versus polarization curves for non-ferroelectric (red), proper ferroelectric (blue) and improper ferroelectric (green) materials. Reversal of one of the distortion modes results in a switch of polarization (green to dashed green, or vice-versa). Taken from [14].

Moreover, there are ferroelectric materials where the polarization is linearly coupled with not one, but two other non-polar order parameters [14], as in:

$$\mathcal{F} \propto \gamma P Q_1 Q_2 \tag{1.3}$$

where γ is a coupling coefficient. It is this ”trilinear coupling” mechanism that originates the so-called Hybrid Improper Ferroelectricity (HIF). The term ”hybrid” stems from the fact that the two non-polar structural distortions, Q_1 and Q_2, are of different symmetry. This mechanism is also important since, in principle, the polarization state can be reversed by changing the sign of one of the two distortion modes [3].

1.2.2 Dion-Jacobson Series

The presented work focuses on the DJ family of NLPs, which have not been as extensively investigated as the RP or Aurivillius phases, but have gathered a lot of interest in recent years [15, 16]. Similarly to the Aurivillius family, the lattice of DJ perovskites cannot be related to a parent phase because the material that makes up the perovskite blocks as $n \to \infty$ does not exist independently as a bulk perovskite. The A' cation that separates the $[A_{n-1}B_nO_{3n+1}]$ perovskites-like blocks is typically an alkali metal, and the undistorted prototype structure will vary according to its size [12]. If it is small (Li or Na), the prototype will present the $I4/mmm$ (#139) symmetry and the perovskite blocks in adjacent layers will be offset from each other by $\frac{1}{2}[1\,1\,0]$. For intermediate size K atoms, it will have the $Cmcm$ (#63) symmetry and the offset in between layers will be $\frac{1}{2}[1\,0\,0]$ or $\frac{1}{2}[0\,1\,0]$. Lastly, for larger sizes (Rb and Cs), it will adopt the $P4/mmm$ (#123) symmetry and the perovskite blocks will be directly aligned.

First-principles calculations by Benedek et al. [15] have shown that octahedral rotations, together with A-site cation displacements, induce HIF in $n = 2$ layered perovskites. In ABO_3 $Pbnm$ perovskites, the $a^-a^-c^+$ octahedral rotation pattern induces local polarizations in the $A-O$ layers. However, the bulk $Pbnm$ structure exhibits zero macroscopic polarization because the A-sites are related by inversion symmetry through the B-site, leading to a complete cancellation of these layer polarizations. When $n = 2$ layered derivatives are formed from $Pbnm$ perovskites, such as RP and DJ phases, this inversion symmetry between A-sites is broken, so the $A-O$ layer polarizations are no longer exactly canceled. In RP phases ($Ca_3Mn_2O_7$, for example), this symmetry breaking gives rise to a macroscopic polarization originating primarily from the AO layers [3]. In contrast, in DJ phases, the macroscopic polarization has contributions from both the AO and BO layers. This is exemplified in Figure 1.5 for the case of $CsLaNb_2O_7$. The polarization from individual $B-O$ layers (NbO) is smaller than that from the $A-O$ layer ($La-O$). However, the total polarization is dominated by the $B-O$ layers because there are two $Nb-O$ layers per unit cell compared to only one $La-O$ layer.

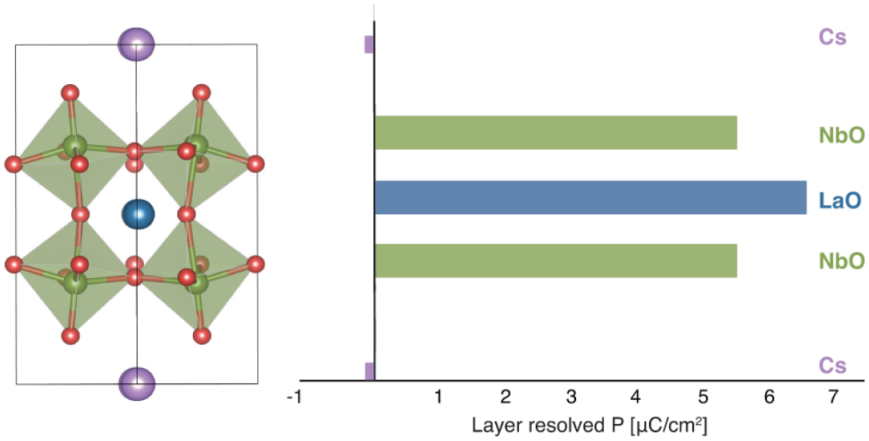

Figure 1.5: Layer-resolved polarization of polar orthorhombic $P2_1am$ phase $CsLaNb_2O_7$. The second Cs atom is just for the sake of representation, as there is only one per unit cell. Taken from [15].

Even with the structural and chemical composition differences between the above mentioned families of layered perovskites, the same phenomenological framework seems to underpin the emergence of polar structures in these materials: that of HIF. For DJ phases especially, the induced electrical polarizations seem to be (in general) larger for smaller coercive fields, which has notably increased their popularity [17]. Some $n = 2$ DJ systems shown to exhibit HIF include: $CsAM_2O_7$ (A = Nd, La and M = Nb, Ta); $RbAM_2O_7$ (A = Nd, La and M = Nb, Ta); $CsAM_2O_7$ (A = Nd, La and M = Nb, Ta) [11].

1.2.3 $RbNdNb_2O_7$ and $RbNdTa_2O_7$ Systems

The specific structures addressed in this thesis are the $n = 2$ DJ oxides $RbNdNb_2O_7$ (RNNO) and $RbNdTa_2O_7$ (RNTO), as well as some later discussed derivatives. These have been investigated by Benedek's research group in order to assess their temperature-dependent phases and corresponding structural phase transitions, by means of Synchrotron X-ray Diffraction (SXRD) and Neutron Powder Diffraction (NPD) [18]. Their results are neatly presented in Figure 1.6.

Regarding their ground-state, these compounds adopt a polar $a^-a^-c^+ / -(a^-a^-c^+)$ distorted $I2cm$ (#17) structure, in which the rotations of the MO_6 octahedra are inverted between adjacent NbM_2O_6 layers. As was previously reported [19], this phase exhibits an expansion compared to the undistorted $P4/mmm$ aristotype cell, where $a \sim b = \sqrt{2}\,a_p$ and $c = c_p$ (the subscript p refers to the aristotype structure). Upon heating, they shift into an anti-polar $a^-b^0c^- / -(a^-b^0)c^+$ distorted $Cmca$ (#64) structure at $790\,K$ for $M = Nb$

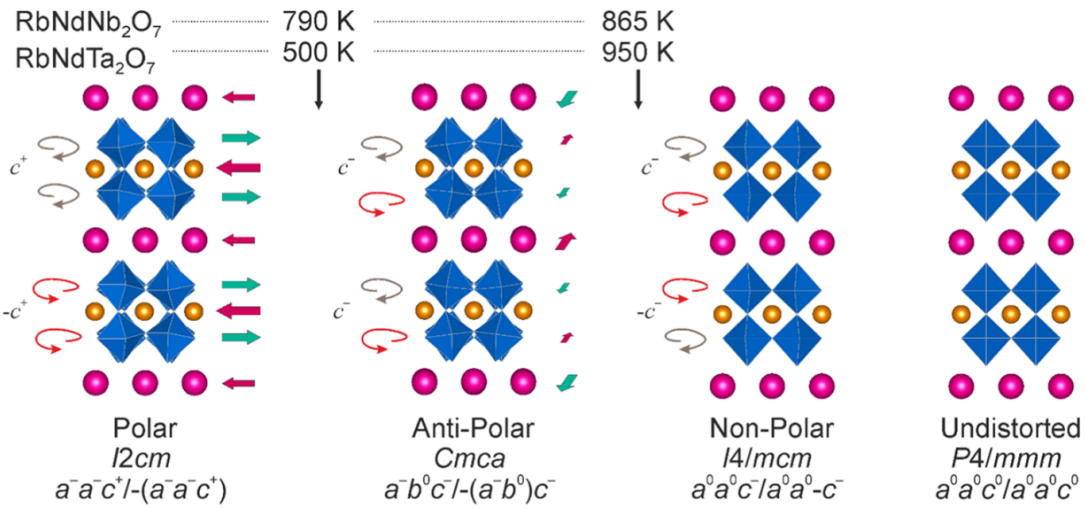

Figure 1.6: Schematic of the crystal structures adopted by $RbNdTa_2O_7$ and $RbNdNb_2O_7$ as a function of temperature. Magenta, orange, and blue units represent Rb, Nd, and $(Ta,Nb)O_6$ respectively. Green and magenta arrows indicate atomic displacements that lead to local electric dipoles. Taken from [18].

and at $500\,K$ for $M = Ta$, with an $a \sim b = 2\,a_p$ and $c = c_p$ expanded unit cell. This transition involves a change in terms of the rotation of the MO_6 octahedra around the z-axis ($c^+ \rightarrow c^-$), as well as a change to zero rotation around the y-axis ($a^-a^- \rightarrow a^-b^0$). There is also an inversion in the direction of the MO_6 rotation around the x-axis between adjacent NdM_2O_7 layers. Before condensing into the aristotype structure at high temperatures, these systems undergo yet another phase transition into a non-polar $a^0b^0c^-/a^0b^0-c^-$ distorted $I4/mcm$ (#140) structure, with an $a = b = \sqrt{2}\,a_p$ and $c = c_p$ cell expansion. This second transition happens around $865\,K$ for $M = Nb$, and $950\,K$ for $M = Ta$.

Looking to the ground-state polar $I2cm$ phase, the HIF mechanism presents itself as the trilinear coupling of the A_5^- $(a^-a^-c^0/-(a^-a^-c^0))$ and A_2^+ $(a^0a^0c^+/a^0a^0-c^+)$ tilting distortion modes, and the Γ_5^- polar mode (Figure 1.7a) [20]. Its transition to the anti-polar $Cmca$ phase also doesn't have a corresponding group/subgroup symmetry relation, which means it is a first-order, discontinuous, phase transition [18]. This is consistent with the large discontinuous changes displayed by the a and b lattice parameters, as well as the local minima in the c parameter (Figure 1.7b).

The complex structural chemistry of DJ based layered perovskites, along with recent findings on structural frustration effects in $(Cs,Rb)NdNb_2O_7$ [21] and the suppression of ferroelectric transitions by symmetry trapping in $Cs(La,Nd)Nb_2O_7$ [22], makes these $n = 2$ DJ perovskites particularly intriguing in regards to their structural instabilities, while also positioning them as a promising candidate for further investigation.

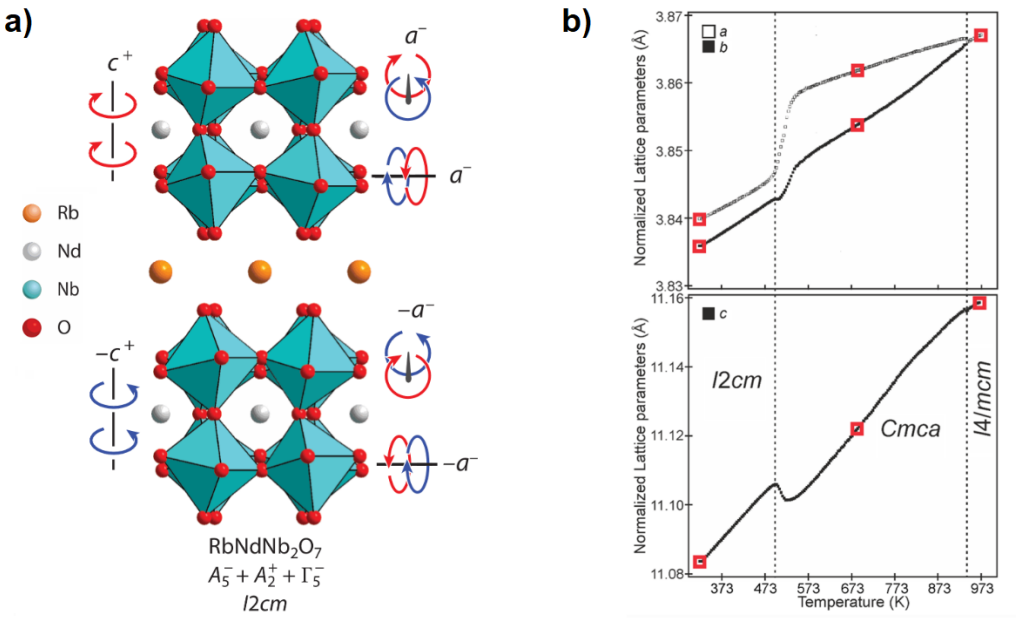

Figure 1.7: **a)** Polar $I2cm$ structure adopted by $RbNdNb_2O_7$ at room temperature and corresponding distortion modes. In-phase rotations are denoted by two red circles, while anti-phase ones are shown with a red and a blue circle. Adapted from [20]; **b)** Evolution of $RbNdTa_2O_7$ lattice parameters determined from SXRD data, normalized to those of the $P4/mmm$ symmetry aristotype, as a function of temperature. Red squares indicate the temperatures at which NPD data was collected. Taken from [19].

1.3. 2D Perovskite Nanosheets

At the beginning of the century, two-dimensional (2D) nanomaterials such as nanosheets, nanorods, nanowires and ultrathin films became a big focal point of researchers and engineers, given how their properties differ from those of three-dimensional (3D) bulk analogues, on account of nanoscale specific effects [23]. Thanks to their particular features, 2D nanomaterials are highly demanded for technologically complex areas, including the development of catalysts and photocatalysts [24–27], photovoltaic and photoeletrochemical cells [28], supercapacitors and nanoelectronic devices [29, 30], etc.

Beyond HIF, layered oxides of the DJ type are already well established, among other energy-related applications, as efficient catalysts and photocatalysts [31]. What distinguishes them from other nanostructured materials with potential for energy applications, besides the already mentioned physical-chemical properties, is their propensity for ion exchange and ion intercalation reactions [32]. In these structures, the negatively charged perovskite slabs, with a thickness of n corner-sharing octahedra, alternate with an interlayer space populated by relatively weak bonded cations [2]. This weaker bond opens

up many possibilities of ion-exchange reactivity and intercalation chemistry at the interlayer. By exploiting this feature, NLP oxides can be exfoliated into 2D nanosheets by facile and scalable methods [26]. This is of high importance for heterogeneous catalysis and photocatalysis, since perovskite nanosheets have a large specific surface areas and small sizes, providing an enhanced number of active sites, efficient reactant absorption and reduced intensity of charge carrier recombination [33].

1.3.1 Exfoliation Methods

There are two common ways to synthesize nanosheets from these compounds: physical exfoliation via ultrasonication and/or chemical exfoliation [30]. Ultrasonic exfoliation is a technique in which the polycrystalline grains of the material are dispersed in a polar solvent, and are then exfoliated by ultrasonication (Figure 1.8). The advantage of this method is that it can be a cost-effective solution for the production of 2D nanosheets. However, it typically yields a mixture of monolayers, few layers or monolayers with a broad lateral size distribution [34]. US not only induces delamination but also breaks the flakes, which means thinner sheets will also tend to have smaller lateral sizes. Sheet sizes as small as a few hundred nm can be obtained with this method, although since it is based on cleavage, the probability of obtaining monolayer sheets is low.

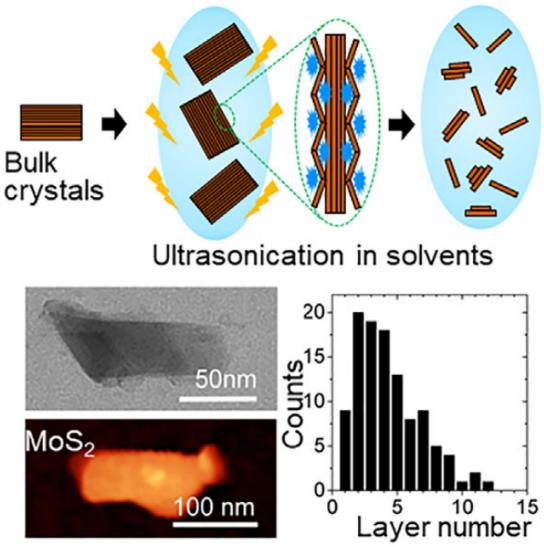

Figure 1.8: Ultrasonic exfoliation process for nanosheet synthesis. Adapted from [34].

On the other hand, in chemical exfoliation, large cations are usually inserted into the interlayer spaces to weaken the binding forces between the host layers. High-yield exfoliation is then achieved with the appliance of a small external force (Figure 1.9), such as shearing by manual or mechanical agitation [35]. All the interlayer spaces in a layered crystal pose the same chemical reactivity, so in principle all the host layers can be separated into single-layer nanosheets. In general, with this method, exfoliation of layered metal oxides occurs via osmotic swelling that expands the interlayer distance, eventually separating the adjacent host layers [37]. In most NLPs however, the alkali metal ions

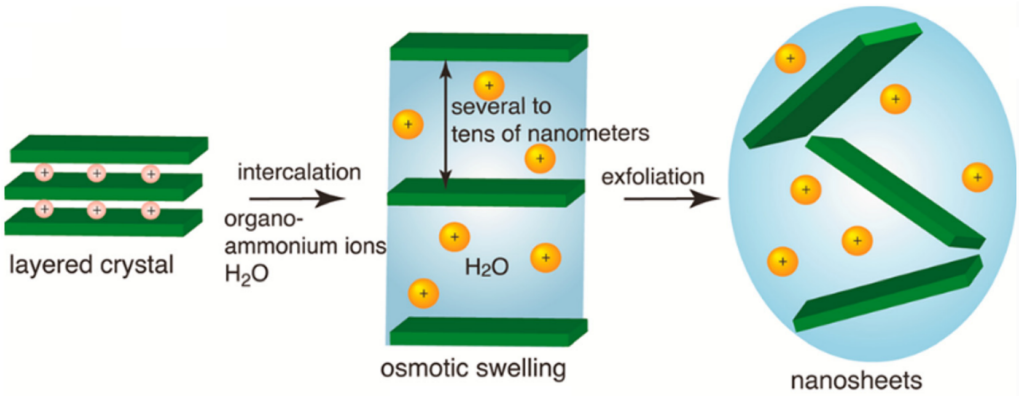

Figure 1.9: Exfoliation of a layered oxide by osmotic swelling. Taken from [36].

separating the perovskite slabs (namely K^+, Cs^+ and Rb^+) provide a high layer charge density, and therefore a strong electrostatic attraction between them and the negatively charged counter-ions [35]. Thus, they are first converted to a protonated form by replacing the alkali ions with H^+, which is possible given the above mentioned high reactivity of their interlayer. The osmotic swelling is induced by bringing them into contact with an a aqueous solution of an organoammonium hydroxide, with the most commonly used being Tetrabutylammonium-Hydroxide (TBAOH), composed of $(C_4H_9)_4N^+$ ions (or simply TBA^+) and OH^- ions. This technique has been shown to produce nanosheets with micrometer-scale lateral dimensions and atomic-scale thickness ($\sim 1\,nm$) [37], which is pretty remarkable. Nonetheless, the outcome is highly dependent on the parent material's grain size and exfoliation conditions, such as solution concentration (TBA^+/H^+ ratio) for example [38].

To exfoliate RP and DJ perovskite phases, like RNNO and RNTO, these two methods are often used in conjunction, with an initial protonation or intercalation step (or both) followed by an ultrasonication process to produce, or complete, the exfoliation [26, 39, 40].

1.4. Motivation for this Thesis

As outlined in the previous sections, DJ based layered perovskites offer an exceptional combination of structural flexibility and chemical responsiveness, showcasing their relevance across functional oxide research. Within this broad class, we concentrate on two DJ compounds, RNTO and RNNO, building directly on earlier studies that characterized them primarily via powder diffraction [18]. Those investigations revealed polar structures and mapped out phase transition pathways, underscoring their rich structural complexity.

Those discoveries strongly motivate further, more detailed explorations to provide complimentary insights to their crystallography, bonding environments, and lattice-dynamics.

In parallel, the structural architecture of DJ compounds naturally opens up to dimensional modulation, an aspect also introduced in the earlier section but still insufficiently understood for many specific compositions. In particular, although the general capacity of DJ phases for ion exchange and exfoliation is well documented, the degree to which these processes are feasible, efficient, or structurally tolerated is highly material dependent and still warrants further exploration due to the lack of experimental clarity in the available literature. Also, RNTO and RNNO phases remain unexplored in this regard, leaving open fundamental questions about their chemical adaptability, stability limits, and potential pathways toward metastable or low dimensional derivatives.

These factors collectively motivate the present study. We extend the structural knowledge of RNTO and RNNO by employing Raman spectroscopy, providing a vibrational perspective that complements and deepens the picture established by diffraction. This technique offers insight into bonding environments, symmetry related changes, and lattice dynamics, thereby enriching our understanding of the subtle structural features within this family of materials. In addition, we evaluate the feasibility of ion exchange and exfoliating of these layered compounds into 2D perovskites and/or nanosheets, a step that expands their relevance toward stabilizing meta-stable phases and low-dimensional materials, respectively.

Thus, through a deeper exploration of their structural and vibrational characteristics, we aim to complement existing structural knowledge with enhanced insights and, by integrating chemical exfoliation studies, elucidate both the potential and the limitations of these compounds within the broader landscape of tunable, low dimensional oxide materials. This integrated perspective provides a foundation for future efforts to tailor DJ phases for advanced functional applications.

2. Methodology

This chapter presents an overview of the methods and techniques used throughout the research. In the first part, we discuss the preparation steps for the samples we analyzed, starting with solid-state synthesis reactions, followed up by ion-exchange and exfoliation steps. In the second part, we discuss all the procedures regarding the characterization of the developed samples, namely X-Ray Diffraction (XRD), Raman Spectroscopy, Scanning Electron Microscopy (SEM) and heat capacity measurements.

2.1. Sample Preparation

2.1.1 Solid-State Synthesis

Given its simplicity, solid-state synthesis is one of the oldest and most common methods for preparing inorganic compounds [41]. It consists of mixing different precursors in solid form, grinding the mixture into a fine powder and mixing it well to promote homogeneity. The reagents should be high in purity and mixed in stoichiometric proportions, and an alcohol is typically used as a medium in this step [2]. The resulting powder may then be pressed into a pellet, making it more compact and thus maximizing the contact between grains, before the calcination process. After that, it is heated up to high temperatures (at least $800\,^{o}C$) in order for ionic diffusion to occur, allowing ionic diffusion and crystallization of the desired phase [41]. Calcination is generally a slow process, and although higher temperatures can be used to promote greater diffusion of the different ions, going too high might lead to the formation of undesired phases. The sample is usually annealed several

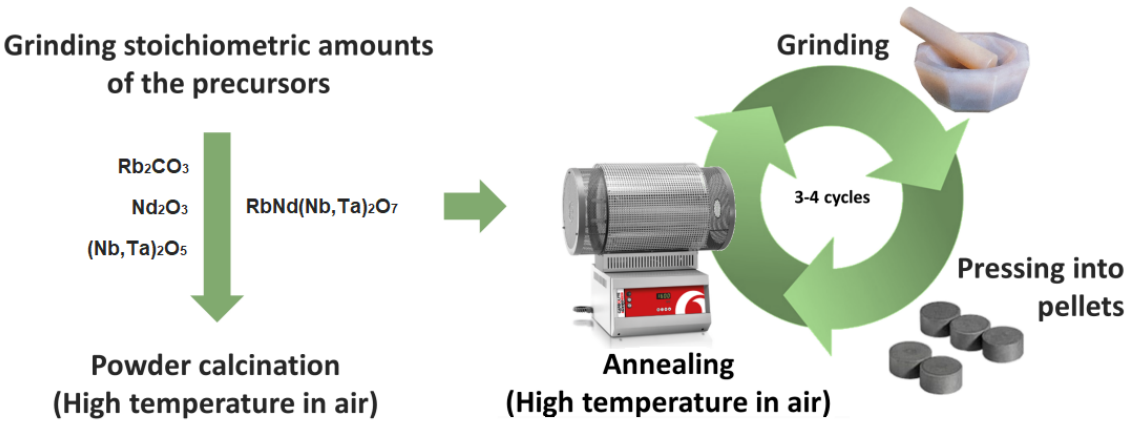

Figure 2.1: Schematic of the solid-state synthesis process. Adapted from [2].

times, which means the whole process of grinding - pelletizing - heating is repeated until a proper phase of the compound is obtained, as shown in Figure 2.1. To confirm such is the case, XRD measurements are performed in between each stage.

In this work, polycrystalline samples of RNNO and RNTO were synthesized through this method, as outlined in [18], using Rb_2CO_3 (99%, Sigma-Aldrich), Nd_2O_3 (99.99%, Sigma-Aldrich) and Nb_2O_5 (99.99%, Sigma-Aldrich) as the precursors (Ta_2O_5 in the case of RNTO). The corresponding chemical reaction to be considered is the following:

$$Rb_2CO_3\,(\mathrm{s}) \;+\; Nd_2O_3\,(\mathrm{s}) \;+\; 2Nb_2O_5\,(\mathrm{s}) \;\longrightarrow\; 2RbNdNb_2O_7\,(\mathrm{s}) + CO_2\,(\mathrm{g}) \qquad (2.1)$$

which is entirely analogous for the RNTO case. They were ground and mixed with an agate pestle and mortar, using isopropanol as a mixing medium. The Nd_2O_3 was pre-heated at $1000\,^oC$ to remove absorbed water molecules from the air. Further stoichiometric proportions of the metal-oxides (Nd_2O_3 and Nb_2O_5) were used with the exception of the Rb_2CO_3 compound, where a 50% excess was added since some of the Rb is lost due to its volatility at high temperatures. The mixture was ground and pressed into a pellet (aprox. $13\,mm$ in diameter) and calcined at $850\,^oC$ for $12\,h$. Afterwards, they were re-ground in the mortar with isopropanol for $\sim 1\,h$ and annealed in air for $12\,h$ at $1000\,^oC$ for the case of RNNO, and $1050\,^oC$ for the case of RNTO. The annealing was performed 3 times before the samples were washed with ultrapure water and dried at $140\,^oC$ overnight, in order to remove any remaining contents of Rb oxide.

2.1.2 Ion-Exchange

Ion-exchange is a prominent technique for the modification of inorganic materials via chemical substitution. It has been shown to work well with layered perovskites for interlayer cation substitution, allowing for the synthesis of meta-stable phases which could not be synthesized otherwise [35]. As discussed previously, we were interested in a hydrogen substitution, also known as protonation. This process was done for the RNNO phase only, by adding $(99.0 \pm 0.1\,mg)$ of the parent sample to $100\,mL$ of a $6\,M$ nitric acid (HNO_3) aqueous solution [27, 31, 42]. The mixture was then magnetically stirred at $200\,rpm$ on a hot plate at $60\,^oC$ for a 5-day period. Lastly, the product was isolated by centrifugation, washing (until the pH is approximately neutral) and drying in an oven at $140\,^oC$ overnight. The powder collected from this procedure is henceforth referred to as Hex-RNNO (hydrogen-exchanged RNNO).

2.1.3 Liquid-Phase Exfoliation

Exfoliation was carried out by first dissolving one of the powder samples (RNNO, RNTO or Hex-RNNO) in an aqueous solution of either N-methyl-2-pyrrolidone (NMP) [26] or TBAOH [27, 39, 42], at various concentrations, and mixed by magnetic stirring. Then, the solutions were ultrasonicated with the SONICS VC505 Ultrasonic Processor ($500\,W$ at $20\,kHz$) a varied number of times for varying time periods. After that, the bulk pieces in the obtained colloidal suspensions were separated with centrifugation, and the exfoliated contents were collected from the supernatant. For measurements of the obtained sheets, drop-casting and also dip-coating methods were used in appropriately washed glass and/or Si substrates. They were then dried in a hot plate at varying temperatures. In some cases, the substrates were also treated with polyethyleneimine (PEI), that promotes electrostatic attraction and aggregation of the negatively charged sheets from the supernatant, improving their adhesion and surface coverage.

2.2. Sample Characterization

2.2.1 X-ray Diffraction

Phase identification of a given crystalline material is done primarily with XRD, as each material has its own XRD signature which can often be compared to a counterpart in a crystallographic database [43]. This technique is based on Bragg's diffraction law, stating that for two identical optical rays scattered by parallel lattice planes, constructive interference is found when the difference between optical paths is proportional to their wavelength λ, with the proportionality factor (known as the diffraction order) being a positive integer:

$$2\,d_{hkl}\,\sin\theta \;=\; n\,\lambda\,, \quad n \in \mathbb{N} \tag{2.2}$$

where d_{hkl} is the distance between lattice planes (associated with a specific family of hkl Miller indices) of and θ is the angle between the optical ray and those same planes, which is to say the complementary to the incidence angle (Figure 2.2) [44]. A scan is made throughout a given range of θ values for a fixed radiation wavelength, whilst the intensity I of the scattered rays is measured in an appropriately positioned detector. Equation 2.2 condition ensures that the electromagnetic waves interacting with the electrons in the crystalline material will only be coherent for distinct θ values, resulting in the diffraction reflections observed in a $I(\theta)$ spectra. From this $I(\theta)$ profile can be extracted information

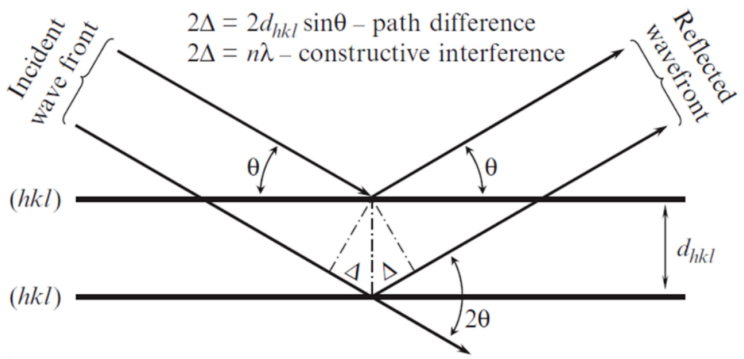

Figure 2.2: Geometry of Bragg's diffraction. The bold lines represent two parallel Bragg planes separated by a distance d_{hkl}. Adapted from [2].

regarding the existing crystalline phases, the percentage at which their present, as well as the corresponding lattice parameters [43].

Optical Configuration

A major aspect to be considered is the geometry being used for the XRD measurement. There are two main options: focused beam, commonly known as the Bragg-Brentano (BB) geometry; and parallel beam geometry [45]. Both of these are schematically shown

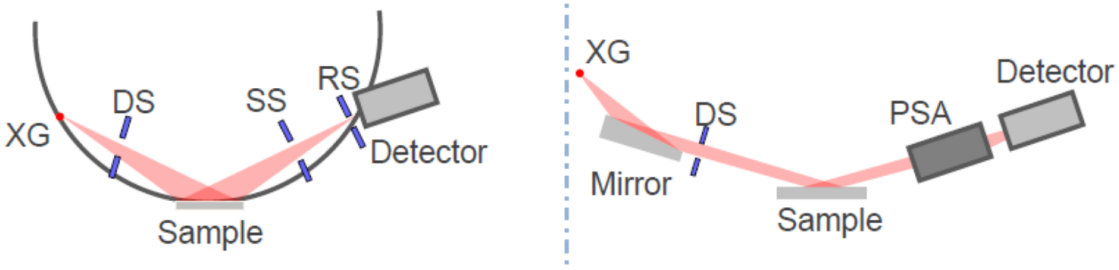

Figure 2.3: Schematic representation of the Bragg-Brentano (left) and Parallel Beam (right) XRD geometries. Taken from [45].

in Figure 2.3. In the first one we have a high intensity beam, which means higher detection resolution, and is used preferably for peaks matching and phase detection. For the parallel beam geometry on the other hand, we have a lower intensity beam since a wide range of $\vec{k}$ directions is killed off (unless the non-selected $\vec{k}$ directions are redirected with the use of a Goebel mirror), which provides lower resolution but might be more useful for curved/rough surfaces and thin films for example. Furthermore, BB geometry allows for either a $\theta - \theta$ or a $\theta - 2\theta$ configuration. In the first case the sample is fixed while the X-ray source and the detector move along a focusing circle, both at an angle θ in relation to the sample's plane. In the latter, the source is fixed and the sample is rotated in order to vary the Bragg angle (2θ), which simplifies the optics and reduces alignment complexities.

For the presented work, XRD measurements were performed with a Rigaku SmartLab Diffractometer with a rotating Cu anode source operating at $9\,kW$ ($200\,mA$ at $45\,kV$). The X-ray beam was dichromatic, composed of $K_{\alpha 1}$ ($1.54059\,\mathring{A}$) and $K_{\alpha 2}$ ($1.54441\,\mathring{A}$) radiation wavelengths. K_β ($\sim 1.39\,\mathring{A}$) rays were suppressed using a Ni filter, which has an absorption edge at $\sim 1.49\,\mathring{A}$. The BB geometry was employed, although in this particular case the sample stage remains fixed, while the source and detector move along an angle $-\theta$ and θ, respectively. Scan ranges span a maximum of $4^o < \theta < 90^o$, with a resolution of 0.01^o.

Rietveld Refinement

In order to extract information from the measured XRD spectra of a known crystalline structure, a method called "Rietveld refinement", introduced by crystallographer Hugo Rietveld in 1967, is utilized [46]. It consists of a least squares method approach for minimizing the difference between the observed and model generated patterns. This is achieved by iteratively optimizing a series of parameters, accounting for instrument configuration, background, lattice constants, atomic positions, and so on. The function to be minimized is given as a weighted difference:

$$L(\theta^*) \;=\; \sum_i \omega_i \Big[I_i^{obs}(\theta) \;-\; I_i^{calc}(\theta^*) \Big]^2 \tag{2.3}$$

where ω_i is a statistical weight factor, I^{obs} is the observed intensity spectra and I^{calc} is the calculated one. Agreement between the two profiles after a sufficiently high number of iterations can be quantified in several ways, namely through the weighted profile R-factor R_{wp} and the expected R-factor R_{exp}:

$$R_{wp} \;=\; \left[\frac{\sum_i \omega_i [I_i^{obs} \;-\; I_i^{calc}]^2}{\sum_i \omega_i (I_i^{obs})^2} \right]^{1/2} \tag{2.4a}$$

$$R_{exp} \;=\; \left[\frac{N \;-\; P}{\sum_i \omega_i (I_i^{obs})^2} \right]^{1/2} \tag{2.4b}$$

where N is the number of data points and P is the number of refined parameters. The quantity χ^2, typically associated with the goodness of fit, follows from the previous two:

$$\chi^2 \;=\; \left(\frac{R_{wp}}{R_{exp}} \right)^2 \tag{2.5}$$

RNNO and RNTO parent sample spectra were refined using the Profex software, which

employs the BGMN kernel to perform the calculations [47]. The reference spectra was obtained by simulating an XRD scan from the CIF files provided in the supporting information of [18], in the software itself. Parameters in Profex were configured until the best possible fit was obtained, within reasonable adjustments as to not fall into overfitting. Other than that, some peak fittings where individually performed using an asymmetrical pseudo-Voigt function, which allows for a flexible variation between Gaussian and Lorentzian curve shapes, while accounting for the asymmetry of the peak.

2.2.2 Raman Spectroscopy

Inelastic light scattering refers to the process in which a light beam is scattered in an optical medium, such as a crystal lattice, resulting in a change of the light's frequency [48]. During this interaction, the absorption of a photon excites the system into a short-lived virtual state, and a new photon is emitted upon its relaxation. In the vast majority of cases this scattering is elastic, meaning the emitted photon has the same energy (and thus frequency) as the incident one, in what's referred to as "Rayleigh scattering". For a very small portion of cases however, the system does not return to its original state, ending up in one with a different energy. This is known as Raman scattering, named after Chandrasekhara Venkata Raman, who discovered the effect in 1928 [49]. If the final state has higher energy than the initial one, the scattered photon carries away less energy, resulting in a Stokes type shift. Conversely, if the system ends in a lower-energy state, the scattered photon has more energy, leading to an anti-Stokes shift (Figure 2.4). These

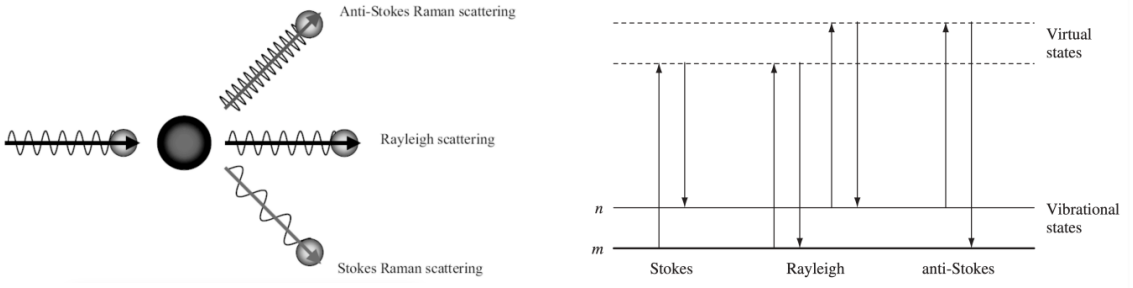

Figure 2.4: Different light scattering phenomena (Stokes, Rayleigh and Anti-Stokes), and corresponding energy-state transitions. Taken from [11].

shifts arise from the creation (emission) or annihilation (absorption) of optical phonons, corresponding to negative or positive frequency shifts of the scattered photon ($\nu_2 - \nu_1$), respectively. As such, this mechanism can be used to probe vibrational, rotational and other low frequency modes of a given system. Particularly, Stokes type scattering is used

to probe this effect, since it is much more probable to happen, giving stronger and thus easier-to-detect signals.

In a typical Raman setup, a laser is used as a monochromatic light source to excite the sample [48]. Scattered photons are then collected, filtered to remove the intense Rayleigh component, and then analyzed using a spectrometer. The obtained intensity spectra is usually shown as a function of the difference in wavenumber $k_1 - k_2$ (Stokes lines will be on the positive side), representing the observed Raman shift. Much like in XRD, this pattern is unique to each material, making this technique very useful for chemical identification and crystallographic analysis.

Measurements were carried out with a Renishaw inVia Qontor spectrometer, available at IFIMUP, at a resolution of $\sim 2\,cm^{-1}$ and using a $633\,nm$ He-Ne ion laser as the light source. The windows-based Raman environment (WiRE) software by Renishaw was used to manage data acquisition. Temperature variation in the range 300-$850\,K$ was performed by conductive heating of the sample with a resistor, and both sample position and temperature were controlled in a Linkam stage.

2.2.3 Scanning Electron Microscopy

A scanning electron microscope (SEM) is an instrument that scans a sample's surface with a finely converged electron beam, in a vaccum environment, displaying an image from the signals produced by the sample [50]. When irradiated with an electron beam, Secondary Electrons (SEs), Backscattered Electrons (BSEs), characteristic X-rays and other signals are generated, although a SEM mainly utilizes the first two to form an image. As seen in Figure 2.5, SEs are emitted near the sample's surface within a few nanometers of depth (1 to $5\,nm$ for most metals and 10 to $20\,nm$ for insulator materials), and thus the image produced from these reflects it's fine topographical structure. On the other hand, BSEs are reflected when the beam strikes the atoms that make up the sample, from depths of up to hundreds of nanometers. Since the number of BSEs depends upon sample composition (average atomic number, crystal orientation, etc.), the corresponding image reflects the composition distribution of the surface. An X-ray detector can also be mounted on the SEM to allow element identification and analysis of sample contents.

Measurements were conducted at the Materials Centre of the University of Porto (CEMUP), in collaboration with the laboratory technician Rui Rocha. Their facility is equipped with

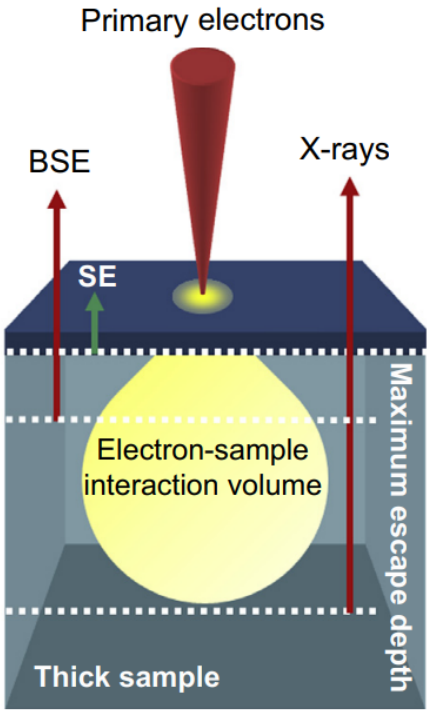

Figure 2.5: Interaction of incoming primary electrons with a sample, and depths from which the generated products can escape. Taken from [51].

an FEI Quanta 400 FEG high-resolution SEM, which employs a Schottky type electron gun with a zirconium oxide cathode.

2.2.4 Heat Capacity Measurements

Heat capacity refers to the amount of energy, in the form of heat, necessary to shift the temperature of a material by one measuring unit [52]. It is an extensive property, dependent upon temperature, volume and pressure conditions. As such, it is characterized either at a fixed volume or a constant pressure, although since pressure is easier to control it is usually the preferred way to do it. Its intensive counterpart is the specific heat, which is simply the material's heat capacity divided by its mass. In solid materials, this property of has two main contributions, one from the ionic lattice and another from the electronic distribution of the system, with the first generally being the most relevant.

Measurement of a sample's heat capacity can be done through several methods, all with the same principle of heating the sample in a controlled way, and measuring the resultant temperature change. One of several methods may be employed, namely a heat-pulse method (HPM), a continuous warming method (CWM), an alternate current method (ACM) or a relaxation method (RM). Hwang et al. [53] proposed a hybrid between HPM and RM, called the "curve fitting method" (CFM), which allows for measurements at different

temperature ranges and for different sample sizes, whilst overcoming issues with thermal connections inherent to RMs. In CFM the heat is applied at constant power for a set time period, followed by a cooling period with the same duration where power is off. This heat/cooling cycle is repeated at several pre-defined temperature values, resulting in a $C_p(T)$ profile. It is worth noting that the temperature fluctuation in each cycle is very small, in order to treat the heat capacity of the material as a constant value.

Physical Property Measurement System

Measurements were performed automatically with the Physical Property Measurement System (PPMS) by Quantum Design (QD), available at IFIMUP. It is capable of wide range of different measurements, and its heat capacity kit employs a CFM. The sample is placed in a puck, resting in a thin layer of heat conducting grease on top of a sapphire (Al_2O_3) platform for good thermal contact. This platform is connected to a heat source on one end, and a thermometer on the other, while these are attached to thin wires that provide electrical and thermal connection as well as support for the platform itself (Figure 2.6). This system is placed in a vacuum environment ($1\,mTorr$) so that the heat flux between

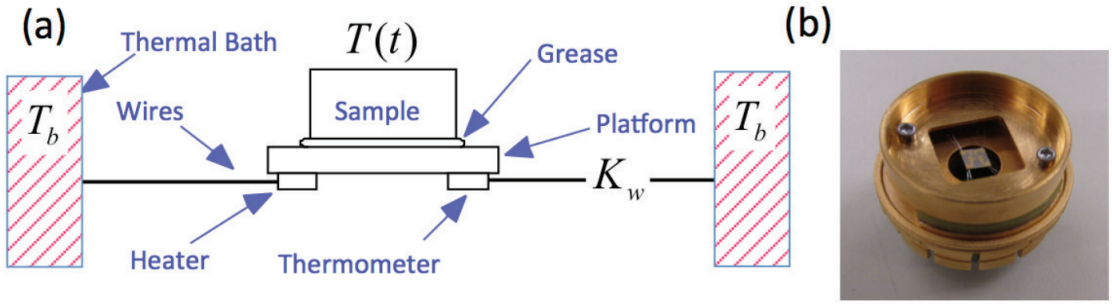

Figure 2.6: **a)** Schematic of the heat capacity hardware; **b)** Heat capacity puck. Taken from [52].

the sample platform and the thermal bath (puck) is dominated by the conductance of the wires. This makes for a large enough time constant that allows the system to achieve sufficient thermal equilibrium during measurements.

The Versalab software (by QD) was used in conjuction with the PPMS system to control the measurement process, and the MultiVu program (also by QD) fitted each heat/cooling cycle data to determine the heat capacity of the sample at T_b (bath temperature). It did so by employing a 1-tau model to describe the flow of power into and out of the sample:

$$C_{totat}\frac{dT}{dt} = P(t) - k_w(T(t) - T_b) \tag{2.6}$$

where C_{total} is the total heat capacity, $P(t)$ is the applied power, k_w is the thermal conductance of the wires and $T(t)$ is the time-dependent temperature. Equation 2.6 yields an exponential-like $T(t)$ solution, with a corresponding thermal time constant $\tau = C_{total}/k_w$, from which the heat capacity value is extracted by MultiVu through a least-squares fitting of the measured temperature data. This C_{total} is however the collective heat capacity of the platform, grease and sample. As such, in order to obtain C_p of the sample, several measurements have to be performed. First the puck must be calibrated without the grease or the sample to determine the thermometry calibration and k_w. Then a measurement is made with just the grease applied, called the ”addenda”. And lastly, the platform/-grease/sample system is measured, from which the contribution of the addenda can be removed to obtain C_p.

3. Experimental Results

This chapter presents the results obtained from the work developed in the scope of this thesis, starting with a detailed characterization of the DJ-structured bulk compounds (RNNO and RNTO) synthesized during this study. The first part includes: (i) XRD analysis to monitor the progress of phase formation throughout the synthesis steps and finally refinement of the optimized samples for their room temperature crystal structure analysis; (ii) SEM imaging and EDS analysis to examine the microstructure and elemental composition, respectively; (iii) Raman spectral analysis combined with temperature dependent studies provides detailed vibrational insights into the crystal structure and its structural phase transition; (iv) Heat-capacity measurements, particularly at low temperatures, to investigate on thermal properties. On the second part, we proceed to the ion exchange and exfoliation procedures, showing the results from several experimental techniques, and discussing our findings derived from these experiments.

3.1. Characterization - Bulk materials

3.1.1 XRD and Crystal Structure

As stated in the previous section, a solid-state synthesis process was employed to produce the RNNO and RNTO samples. For each step of the process, from the first annealing to the sample washing, an XRD scan was took to assess the development of the desired phase. The reference XRD patterns, for comparison, were simulated in VESTA with an X-ray wavelength of $1.54059\,\mathring{A}$, using the respective CIF files available in the supporting information of Zhu et al.[18]. Both samples were annealed until a satisfactory diffraction pattern was achieved, and then the synthesis was finalized with the washing step.

Starting with the RNNO compound, the XRD pattern obtained for each step of the synthesis process is shown in Figure 3.1. The dashed lines mark the 0-count of each plot, and the intensity values are normalized to their respective maximum. Looking at them, we can see that there are practically no shifts in terms of peak positions, meaning the unit-cell parameters of the structure didn't change significantly throughout the process, having been established from the very beginning. The first-anneal spectrum displays some extra phases, most notably evidenced by the reflections found at $2\theta \sim \{25.5\,;27.8\,;29.4\,;31.7\}^{o}$. The extra phases seemed to be removed by the second annealing, and thus we proceeded to

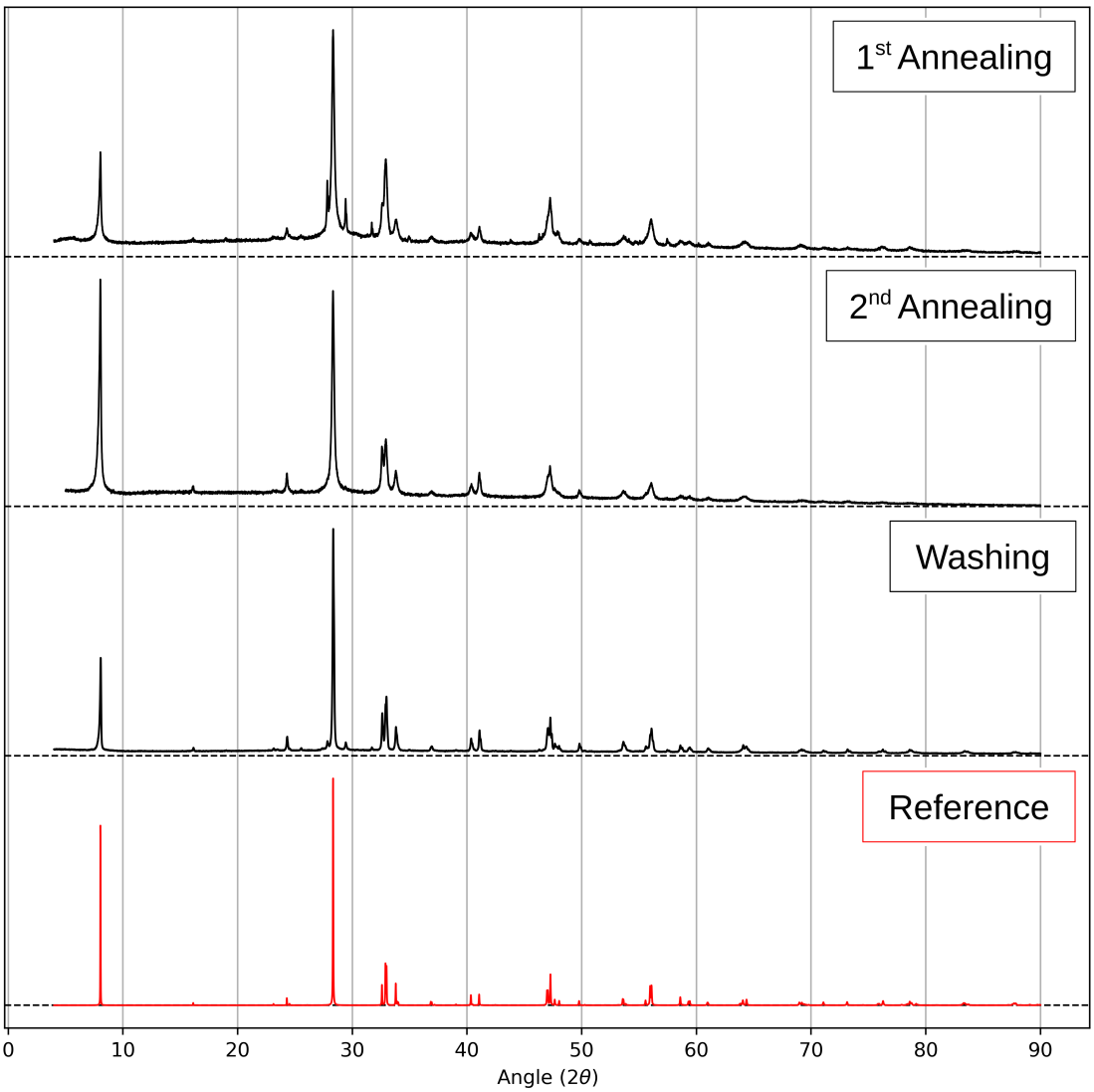

Figure 3.1: XRD patterns of each step of the $RbNdNb_2O_7$ synthesis process, starting with the 1st Annealing (top) and ending with the washing step. The reference spectra simulated from the CIF file in the supporting information of [18] is shown at the bottom.

the washing step. While the second annealing appeared to have eliminated the additional phases, XRD analysis of the washed sample using the PANanalytical X'Pert HighScore Plus software revealed the presence of a monoclinic $NdNbO_4$ phase (which explains the 27.8, 29.4 and 31.7^o angle reflections), and the possibility of RbO_3 (25.5^o peak). However, the major RNNO phase should be above 90%, considering the intensity of its sharpest peak and the ones from the $NdNbO_4$ impurity. Crystallinity also improved throughout, as the peaks became sharper and there was less background signal (reduced amorphous scattering), indicating longer-range ordering, larger crystalline domains and lower micro-strain. Hence, we determined to continue the studies with the resulting sample.

To get deeper information into the crystal structure, we performed structural refinement on the final XRD data collected for washed RNNO sample at room temperature. As previously mentioned, refinement was done using the Profex software [47]. Besides the diffraction pattern itself, the BGMN kernel performs the calculations taking in as input: an *instrument configuration* ($.geq$) file, related to the geometry and contribution of all optical elements utilized for the measurement, including the source and the detector; as well as a *structure* ($.str$) file for each crystal phase, where control over the refinement variables is provided. Structural refinement was performed considering the $I2cm$ symmetry of RNNO (its reported room temperature phase) and the monoclinic $NdNbO_4$ as the additional phase. The initial str file for each phase was created within Profex from the respective reference CIF file. The most important parameters to be adjusted within these files are the ones that refine the peak shapes, them being: B_1 associated with peak broadening due to small crystallites; k_2, associated with peak broadening due to microstrain; and k_1, related to crystallite size distribution. The resulting structurally refined plot

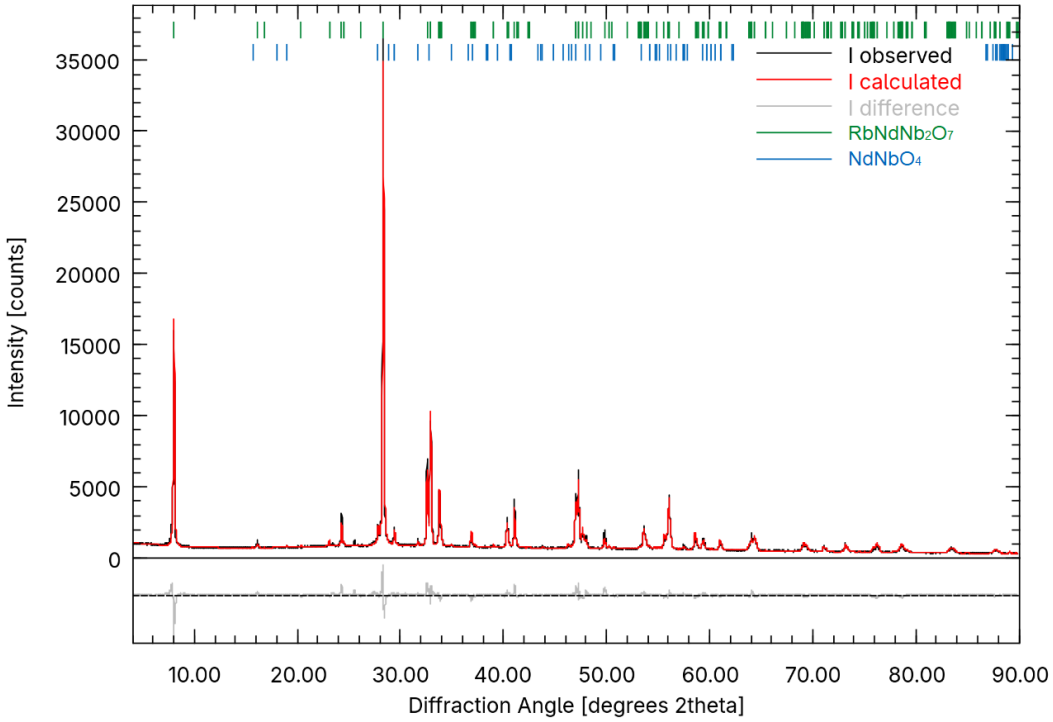

Figure 3.2: Plot of the observed XRD pattern I_{obs} (after sample washing), refined pattern I_{calc} and respective difference I_{diff} for the synthesized $RbNdNb_2O_7$.

is shown in Figure 3.2. For RNNO, $k1$ was set to 0 (crystallite size distribution is not accounted for) and $\{k_2, B_1\}$ were refined anisotropically, while for $NdNbO_4$ the k_1 was also set to 0 but k_2 and B_1 were refined isotropically. This yielded the values: $R_{wp} = 6.90$, $R_{exp} = 3.54$ and $\chi^2 = 3.80$; and phase quantity of $NdNbO_4$ was found to be $5.03\,\%$. The

value of χ^2 is relatively low (ideally it would be ≤ 1.5) and the profile of the spectrum seems properly described, so we assume the fit is appropriate. It could perhaps be further improved by including some other phase that wasn't accounted for (even though it should be at a very low percentage), as well as providing a more exact configuration of the geq file. The values obtained for the lattice parameters of the RNNO phase were: $a = 5.443(1)$, $b = 5.429(0)$ and $c = 21.958(2)$ $\AA$. This is in good accordance with our reference [18], with deviations bellow 0.6%.

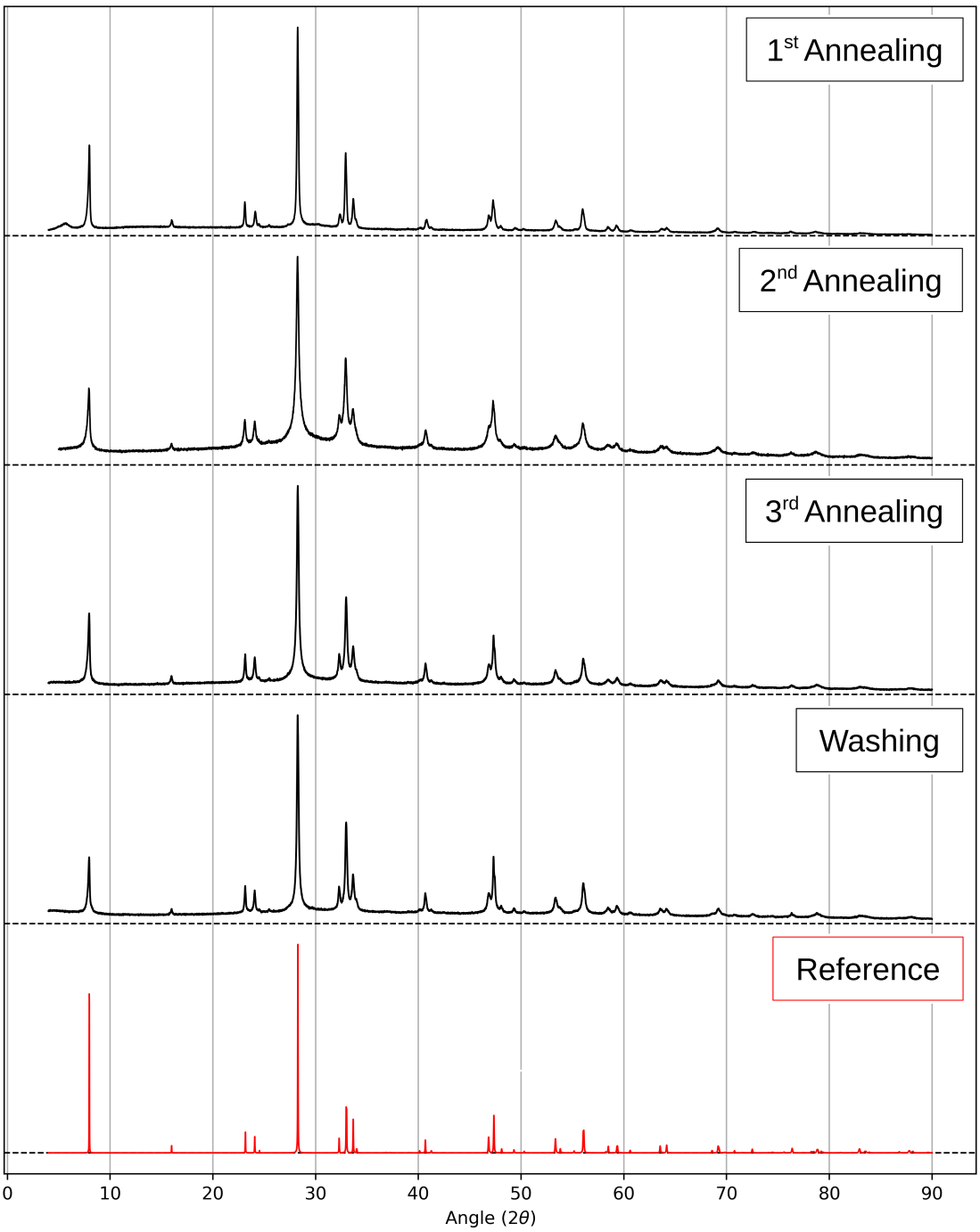

Figure 3.3: XRD patterns of each step of the $RbNdTa_2O_7$ synthesis process, starting with the 1st Annealing (top) and ending with the washing step. The reference spectra simulated from the CIF file in the supporting information of [18] is shown at the bottom.

Moving on to the RNTO compound, the progression of XRD patterns throughout the synthesis is displayed in Figure 3.3. The first annealing resulted in a very crystalline pattern right away, and with no distinct minor phases, but the sample was annealed further in order to make sure only the desired phase was formed. Oddly enough, the diffraction pattern from the second-annealing showed lower crystallinity than the first annealing, and

since the absence of extra phases could not be confirmed with certainty, we decided to perform one last annealing. As expected, crystallinity improved and the diffraction pattern showed no signatures apart from the RNTO phase, and thus the synthesis was finished with the washing step.

Structural refinement was then carried out on the XRD data collected for the washed sample at room temperature taking into consideration the $I2cm$ symmetry of RNTO, and the result is shown in Figure 3.4. Once again $k1$ was set to 0 and $\{k2, B1\}$ were refined

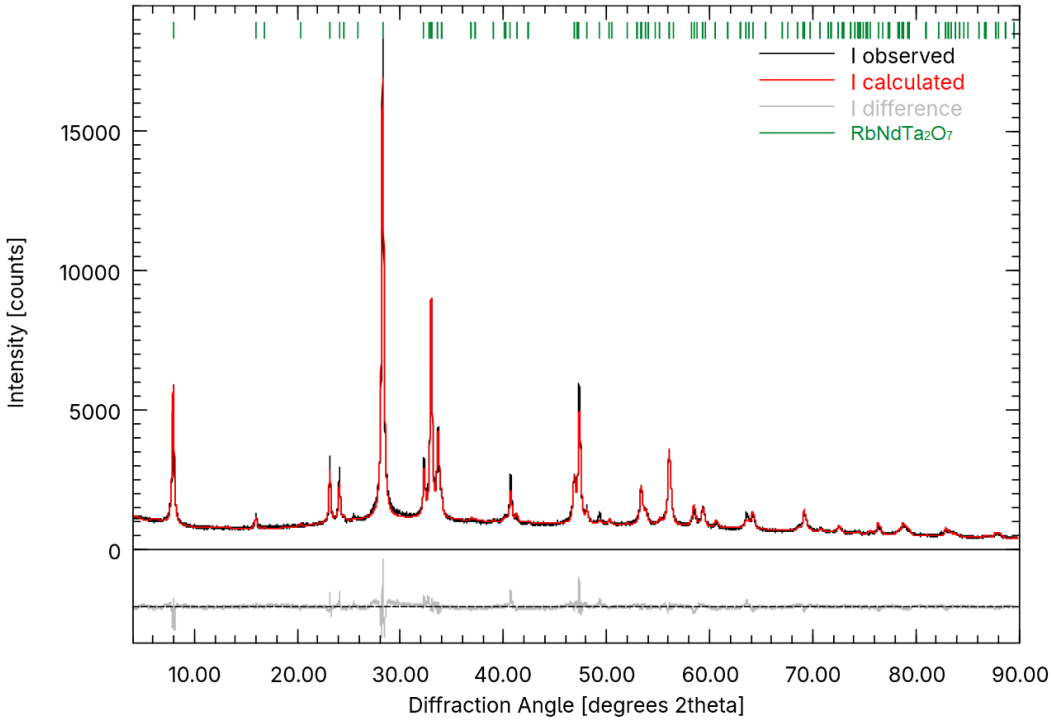

Figure 3.4: Plot of the observed XRD pattern I_{obs} (after sample washing), refined pattern I_{calc} and respective difference I_{diff} for the $I2cm$ phase of $RbNdTa_2O_7$.

anisotropically, yielding the values: $R_{wp} = 5.77$, $R_{exp} = 3.16$ and $\chi^2 = 3.33$. The χ^2 is also pretty good in this case, and the spectrum's profile seems properly fitted. For the lattice parameters, we obtained $a = 5.426(8)$, $b = 5.428(0)$ and $c = 22.158(9)$ $\AA$, which is is in reasonable agreement with our reference ($< 1.5\%$), with the b parameter deviating more significantly. The results for both samples are summarized in Figure 3.5, along with a representation of their corresponding crystal structure.

Furthermore, we performed a detailed analysis of the crystal structures of RNNO and RNTO considering lattice parameters obtained from our refinements, to interpret their structural distortions and the nature of chemical bonding. The crystal structure of both the compounds presented in Figure 3.5 clearly shows the tilted octahedral bilayer. Selected

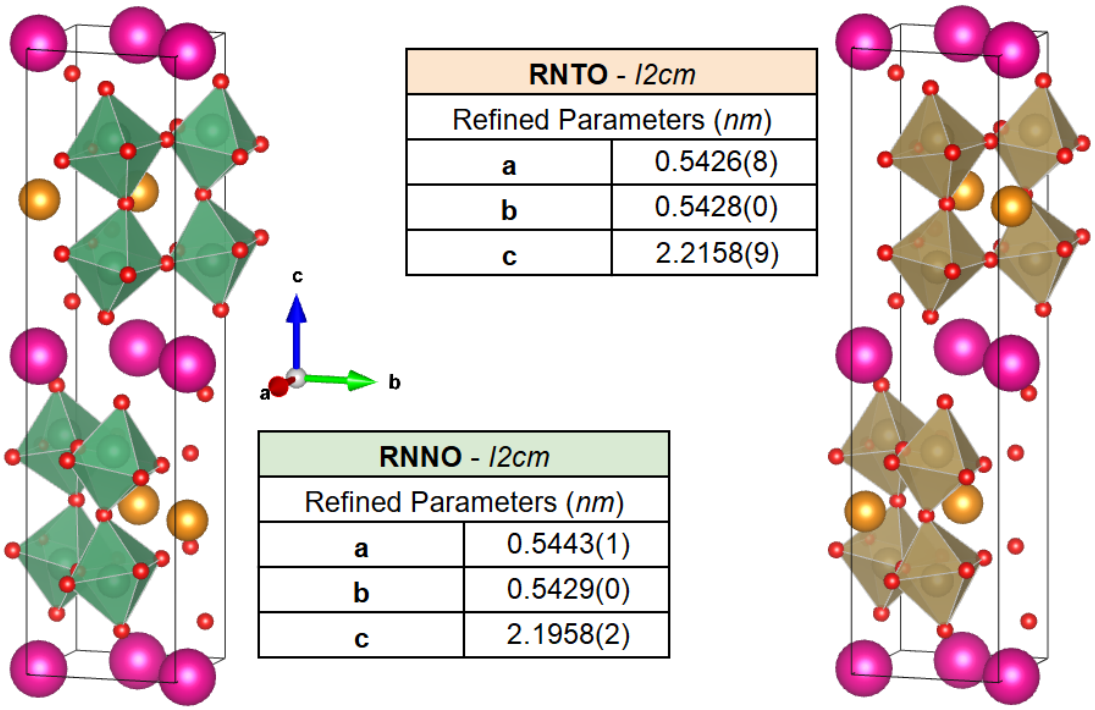

Figure 3.5: Representation of $RbNdNb_2O_7$ and $RbNdTa_2O_7$ crystal structures and their estimated lattice parameters, obtained from the Rietveld refinement of the XRD spectra. Solid lines describe the limits of each unit cell. Drawn with the VESTA software.

bond distances and polyhedral distortions obtained for both the compounds are compared in Table 3.1 and are consistent with the previous reports [18, 54]. The shorter $(Nb, Ta) - O_{Rb}$ distance compared to the average $(Nb, Ta) - O$ confirms a notable displacement of Nb/Ta ions towards the $Rb - O$ layers. This displacement of octahedral B-site ions from the equatorial plane towards the $Rb - O$ layers, could be attributed to the SOJT effect, typically associated with the d^0 ion (Nb^{5+}/Ta^{5+}) [54].

Table 3.1: Crystal Structure Analysis (B = Nb/Ta)

Distance (Å)	**RNNO**	**RNTO**
$\langle \mathrm{Nd} - B \rangle$	3.536	3.527
$\langle \mathrm{Rb} - B \rangle$	4.162	4.239
$\langle B - O \rangle$ (avg.)	2.011	2.012
$\langle B - O_{\mathrm{Rb}} \rangle$	1.746	1.779
$\langle \mathrm{Nd} - O \rangle$ (avg.)	2.534	2.516
$\langle \mathrm{Rb} - O \rangle$ (avg.)	3.110	3.110
Polyhedral distortion from bond lengths ($\times 10^{-2}$ Å)		
$\langle \mathrm{Nd} \rangle$	9.444	9.645
$\langle \mathrm{Rb} \rangle$	5.460	3.874
$\langle B \rangle$	6.836	5.570

On comparing the polyhedral distortions in both compounds, Nd polyhedra exhibit the highest distortion, followed by (Nb/Ta) octahedra, while Rb polyhedra display the lowest distortion. Overall, the B-site associated octahedral distortion is greater in RNNO $(6.836 \times 10^{-2}\,\mathring{A})$ than in RNTO $(5.570 \times 10^{-2}\,\mathring{A})$. Also, we observe a longer $Nd - Nb$ distance than $Nd - Ta$ and shorter $Rb - Nb$ distance than $Rb - Ta$. The observed enhanced octahedral distortion, together with large $Nd - Nb$ separation and shorter $Rb - Nb$, indicates a larger displacement of the Nb ion toward the Rb layer compared to Ta ion, which could be attributed to the stronger SOJT effect of Nb^{5+} arising from its greater covalence with oxygen versus that of Ta^{5+} [55]. This interpretation is further supported by the observation of shorter $Nb - O_{Rb}$ bond $(1.746\,\mathring{A})$ in RNNO compared with the corresponding $Ta - O_{Rb}$ $(0.779\,\mathring{A})$ bond in RNTO. These structural differences explain that the stronger SOJT effect of Nb^{5+} provides enhanced stability for the polar phase in RNNO, reported as having a higher structural phase transition temperature (polar $I2cm$ to anti-polar $Cmca$) at $790\,K$ (compared with RNTO at $500\,K$). Altogether, our findings indicate that the SOJT activity of the B-site metal ion plays a significant role in governing the overall structural distortions in the DJ family of perovskites, including octahedral rotations and deformations, as well as A-site displacements.

A different RNNO sample, previously synthesized by my research group peers, was used to conduct some of the studies reported in this thesis, including Raman and heat capacity measurements. Thus, I performed a structural refinement of its XRD pattern, and the corresponding fitted plot is presented in Figure 3.6. Since there was a lot of background noise, the lower end of the spectrum was cut up to $2\theta = 20^{o}$. The fit resulted in $R_{wp} = 3.52$, $R_{exp} = 1.85$ and $\chi^2 = 3.62$. Lattice parameters were obtained as $a = 5.441(8)$, $b = 5.428(0)$ and $c = 21.956(2)\,\mathring{A}$, in agreement within 0.4% with those of the RNNO sample containing 95% as the main phase.

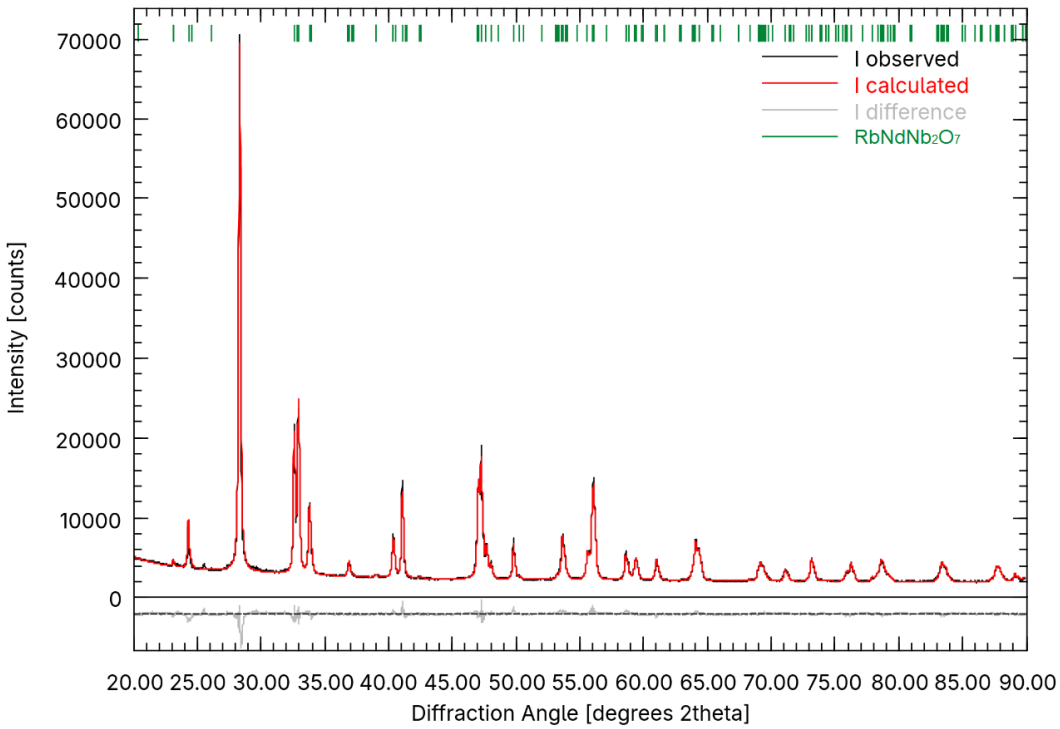

Figure 3.6: Plot of the observed XRD pattern I_{obs}, refined pattern I_{calc} and respective difference I_{diff} for a previously synthesized $RbNdNb_2O_7$ sample.

3.1.2 SEM Imaging

To complement the XRD data of RNNO and RNTO compounds, SEM images of their powdered forms were acquired, along with Energy-dispersive X-ray Spectroscopy (EDS) scan for elemental analysis. The powder samples were mounted on to the EDS sample holder using double-sided conductive carbon tape. From the images in Figure 3.7, we can see that RNNO exhibits a microstructure with a lamellar morphology. The sharp outlines of the thin plate-like particles suggest cleavage along crystallographic planes, with platelets averaging in lateral size between $1 - 3\,\mu m$. Their smooth surfaces and well-defined contours point toward high crystallinity, which is reflected by the peak sharpness of its XRD pattern (see Figure 3.1 - Washing). Moreover, their anisotropic shape also indicates a directional crystal growth that is characteristic of layered oxides, where in-plane bonds are stronger than inter-layer ones. Some of the smaller pieces ($0.5 - 1\,\mu m$) could perhaps be the $NdNbO_4$ impurity. Regarding the EDS spectrum, we can see that the estimated atomic percentages of the metallic elements roughly match the 1:1:2 stoichiometric ratio (1:0.98:2.18), however oxygen quantity is substantially undercounted. This is simply a result of measurement limitations, since O atoms produce a very low energy signal that is easily absorbed inside the material.

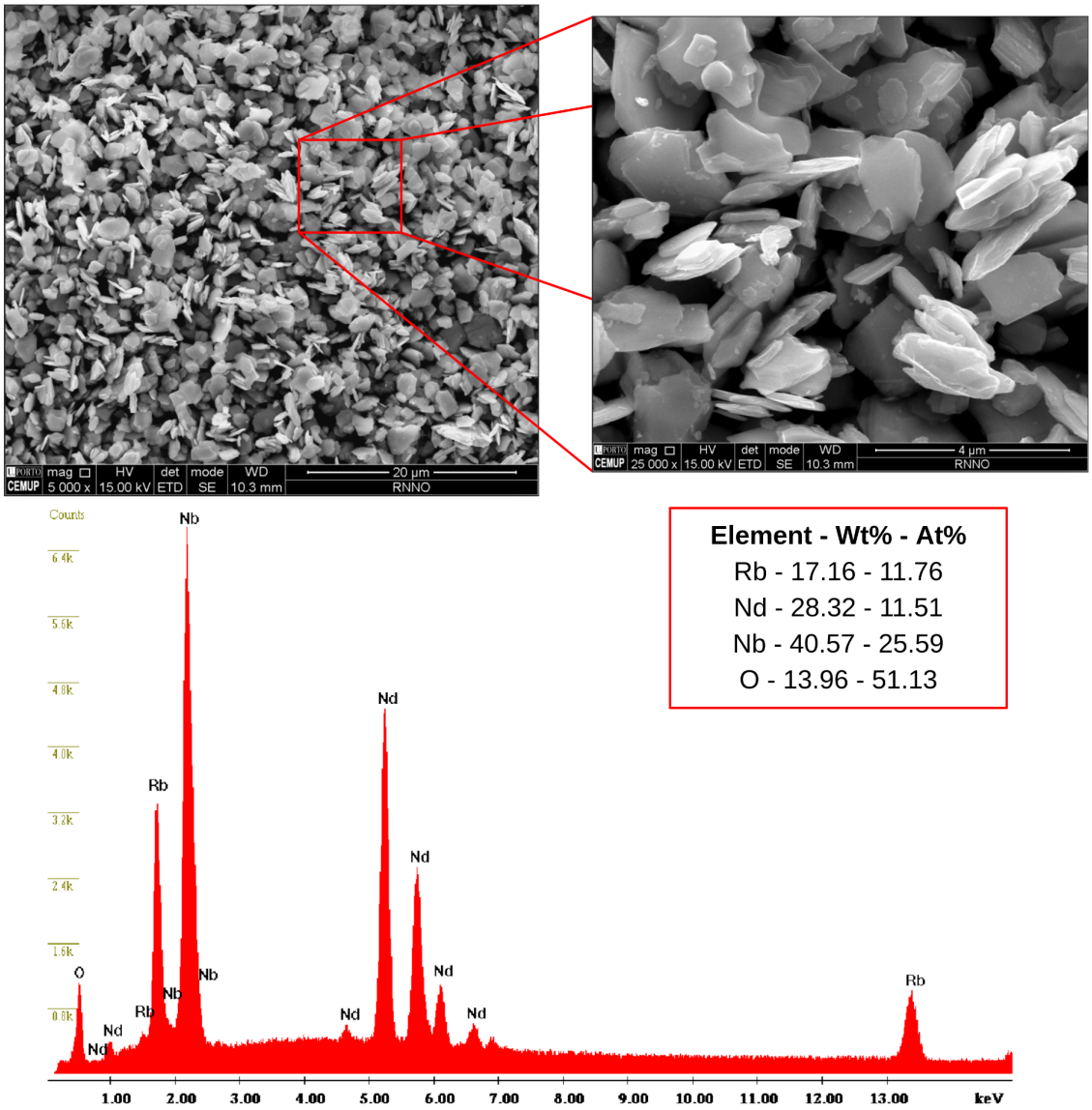

Figure 3.7: SEM images captured for $RbNdNb_2O_7$ in powder form (top), at a scale of 20 and $4\,\mu m$. EDS spectrum and measured chemical composition (bottom), including atomic and weight percentage.

Moving on to the RNTO sample (Figure 3.8), images showcase a more dense and granular powder, with rounder and more compacted particle aggregates in comparison to RNNO, making it less distinctly layered. This indicates that the Ta influences the structure in such a way that the nucleation process is more isotropic or cauliflower-like. The explanation for this difference might lie with the diffusion behavior of the heavier Ta^{5+} ions [56]. Moreover, the fact that it appears less crystalline is conducent with the broader XRD reflections (Figure 3.2 - Washing). Particle size is notably smaller in comparison to RNNO, with feature sizes ranging from a few hundreds of nm to $1\,\mu m$, so this material is already nano-scaled. In terms of elemental composition, it is pretty much analogous to the RNNO case, showcasing a 1:1.09:2.28 ratio of Rb:Nd:Ta.

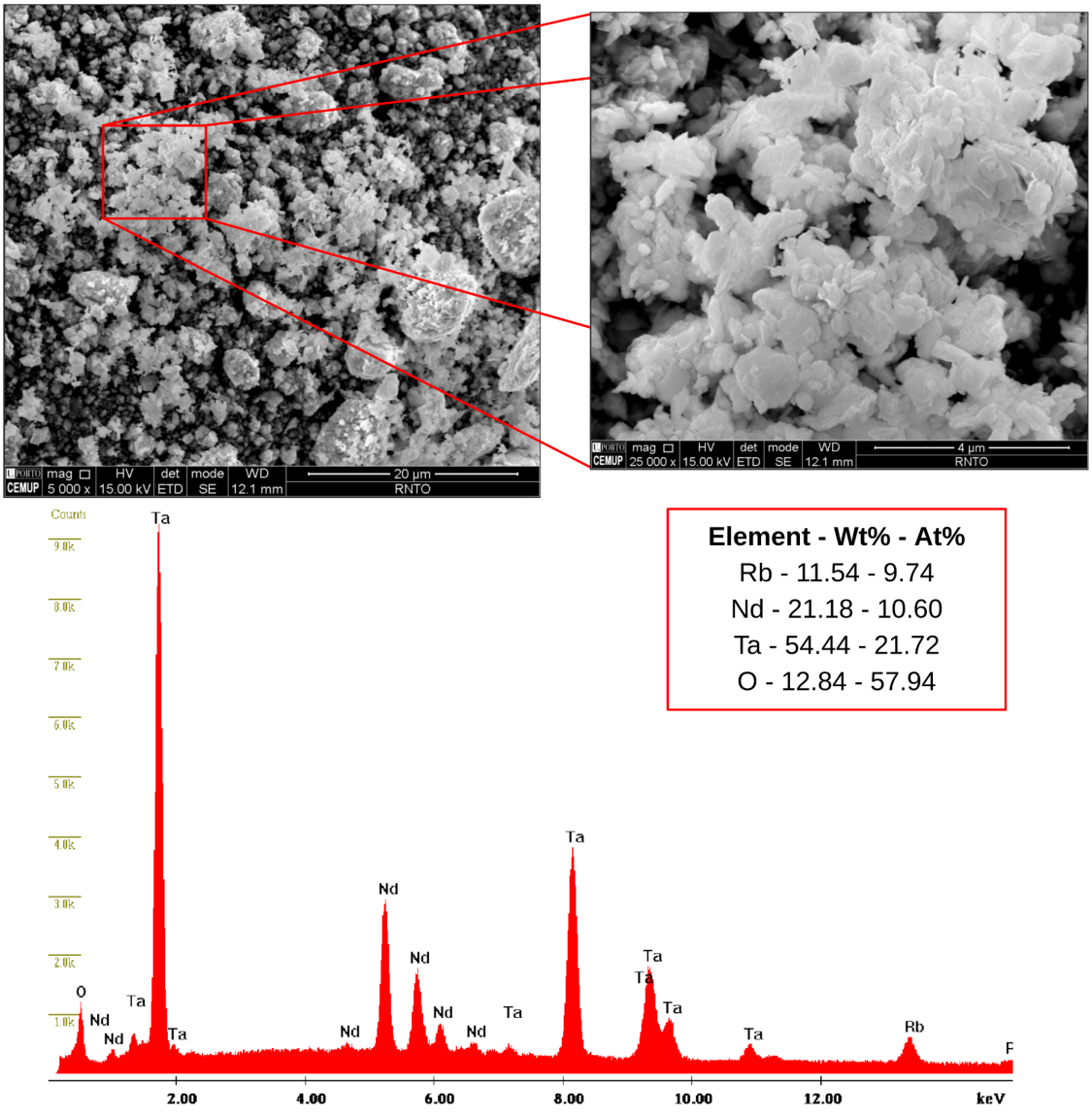

Figure 3.8: SEM images captured for $RbNdTa_2O_7$ in powder form (top), at a scale of 20 and $4\,\mu m$. EDS spectrum and measured chemical composition (bottom), including atomic and weight percentage.

3.1.3 Raman Spectral Studies

To complement the structural analysis from XRD and to investigate the crystal structure from the perspective of lattice vibrations, we carried out Raman spectral studies. This approach has not been much explored for these type of materials, although a very recent study on RNTO has been reported by our group [54]. Within the scope of this thesis, we performed a comparative investigation of RNNO, investigating its crystal structure, phase transition, and associated lattice dynamics using variable-temperature Raman spectra collected during heating sequence in the $[300\,;850]\,K$ range, particularly around its reported phase transition into the anti-polar $Cmca$ structure at $790\,K$ [18]. Measurements were performed around the same sample region, after the stabilization of temperature at each step.

Starting off with the ambient temperature spectrum ($300\,K$), the obtained normalized intensity profile is shown in Figure 3.9. A total of 18 modes were identified through the

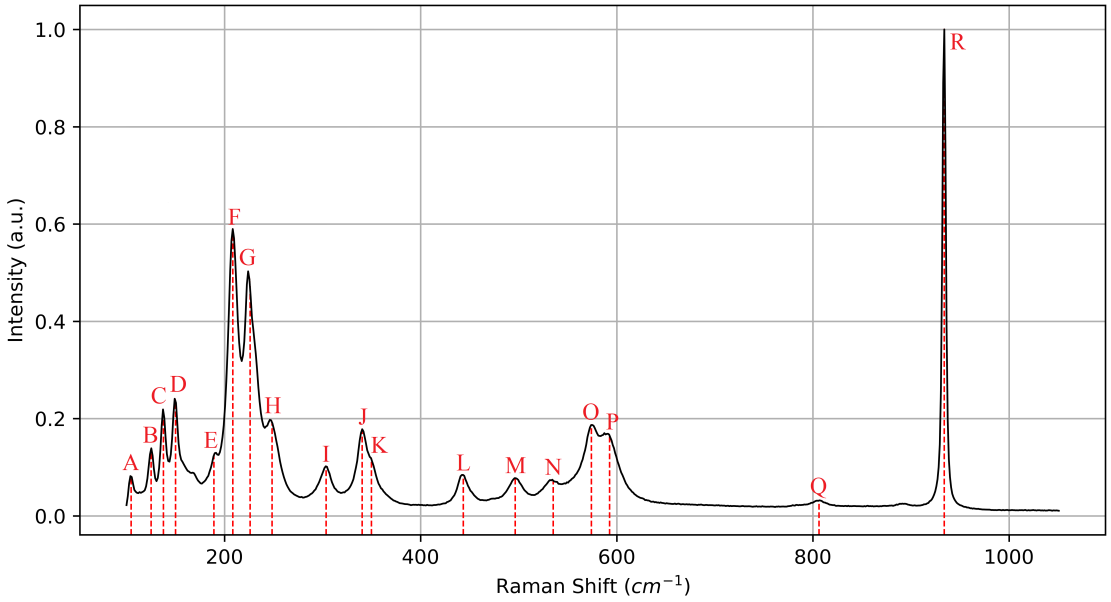

Figure 3.9: Normalized Raman spectrum of $RbNdNb_2O_7$ measured at ambient temperature. Red lines indicate the peak position of identified vibrational modes.

fitting method, each indexed with a letter from A to R. Their corresponding Raman shift is highlighted in the plot by the red dashed lines. Comparing with the recent work of RNTO reported from our group [54], some correspondence between vibrational modes and structural features can be assigned. Following the same approach, the spectral pattern of RNNO can be divided into two regions: higher frequency region, between 400 and $1000\,cm^{-1}$; and lower frequency region, bellow $400\,cm^{-1}$. Raman modes above $400\,cm^{-1}$

are related to NbO_6 octahedral vibrations, while the ones bellow that are associated with $Rb-O$ and $Nd-O$ layers, as well as displacements of Nb ions. The high intensity peak at $933.8\,cm^{-1}$ (Mode R) is attributed to the symmetric stretching mode of the NbO_6 octahedra, as its high frequency is consistent with the shorter bonds within the octahedra. In the 400 to $660\,cm^{-1}$ region (modes L, M, N, O and P), higher frequency modes are associated to asymmetrical stretching of the octahedra (in$-$plane octahedral vibrations), while the lower frequency ones are related to octahedral bending, although it's not possible for now to pinpoint exactly which of them are responsible for which of the two effects. Bellow $400\,cm^{-1}$, one can distinguish three main sections given the proximity of modes, and thus, considering bond lengths, some assumptions can be made regarding the vibrations they correlate to. The lower frequency section (modes A, B, C and D) is likely associated with the lengthier $Rb-O$ layer vibrations, while higher frequencies (modes I, J and K) might be linked to the octahedral librations due to the symmetric deformation or bending in the octahedron coupled to the displacement of Nd. Lastly, in the middle section (modes E, F, G and H), peaks may arise from the translational vibration of Nd ions.

A comparison of the Raman peak positions of RNNO and RNTO (Table 3.2), reveals a slight increase in the symmetric stretching mode for RNNO ($933\,cm^{-1}$) than that of RNTO ($928\,cm^{-1}$), indicating shorter axial octahedral bonds in RNNO. This observation corroborates with our findings from the structural analysis using XRD, which indicates a shorter axial bond for $Nb-O_{Rb}$ than that of $Ta-O_{Rb}$. This bond shortening is attributed to the stronger SOJT effect of the Nb ion compared to that of Ta, in agreement with our XRD-based crystal structure analysis.

The reduced octahedral asymmetric stretching frequency in RNNO also confirms the same, because the stronger Nb off-centering (SOJT distortion) produces significantly longer equatorial $Nb-O$ bonds compared with the corresponding $Ta-O$ bonds in $RNTO$. The octahedral bending ($O-B-O$) frequency seems a bit higher in RNNO, which might be associated with the higher distortion in RNNO (enhanced angular strain) compared to RNTO (for octahedral distortion ref Table 3.1). However, the octahedral libration frequencies are nearly identical in RNNO and RNTO. This might pe possible because librational modes depend mainly on the inter-octahedral connection $(B-O-B)$, which could remains very similar in both structures, whereas octahedral stretching and bending modes (both associated with intra-octahedral bonds) are strongly affected by the different SOJT distortions of Nb and Ta.

Table 3.2: Comparison of Raman shifts (cm^{-1}). Designated peaks and RNNO values are from this work, while RNTO values are from reference [54].

Designated peaks	Symmetry modes	RNTO	RNNO
$A-D$	$Rb-O$ layers	< 165	< 176
$E-H$	Nd-site displacement mode	209 - 239	189 - 248
$I-K$	Octahedral librations	284 - 349	303 - 349
$L-N$	Octahedral bending	446 - 501	443 - 535
$O-P$	Octahedral asymmetric stretching	586 - 651	574 - 592
R	Symmetric stretching mode of octahedra	928	934

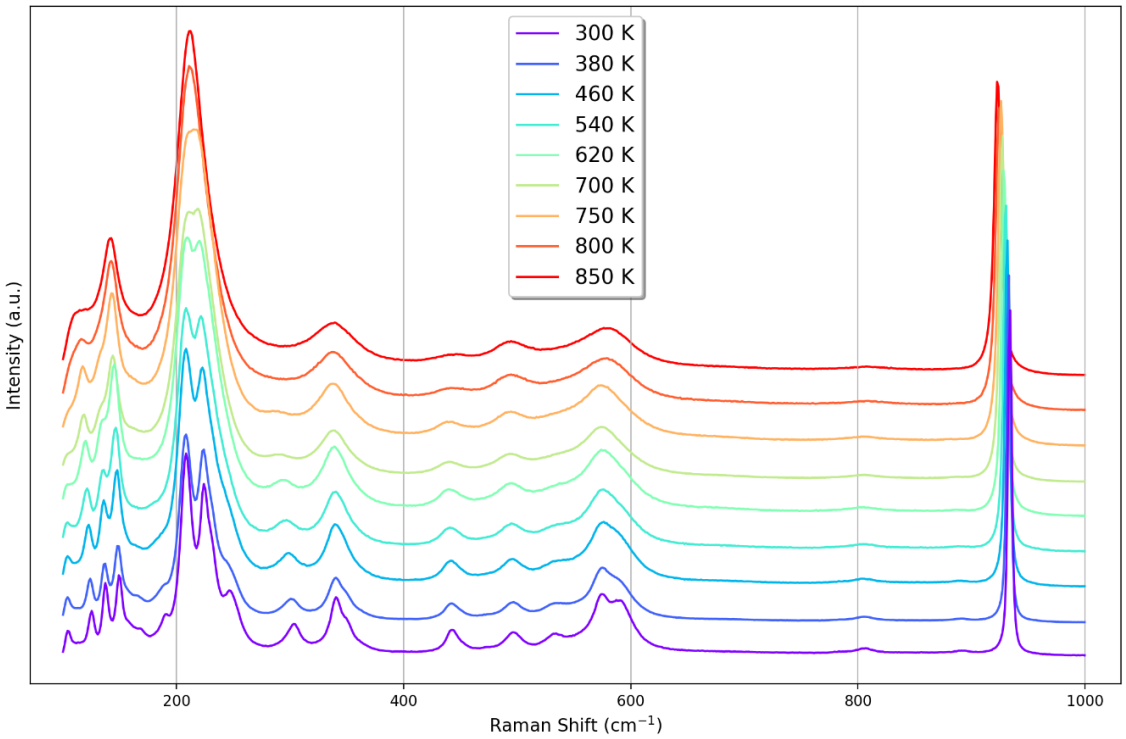

Figure 3.10: Temperature evolution of $RbNdNb_2O_7$ Raman spectra.

To provide a general picture, some of the measured spectra, spread across the whole range of T values, are displayed in Figure 3.10. In order to analyze the collected data, each spectrum was subdivided in regions of interest, which were fitted separately to extract information on the presence and frequency of the system's main vibrational modes, as well as their linewidth and amplitude. This was achieved by fitting each spectral window with up to five superimposed Lorentzian functions on a linear background, whose functional form is given by:

$$I(\omega) = m\omega + B + \sum_{i=1}^{N} \frac{\omega_i^2 \Gamma_i Q_i \omega}{\left(\omega^2 - \omega_i^2\right)^2 + \omega^2 \Gamma_i^2} \left(1 + \frac{1}{e^{\frac{\hbar c \omega}{k_B T}} - 1}\right) \tag{3.1}$$

where the term $m\omega + B$ corresponds to the linear background and ω_i is the resonance frequency of the i-th mode, while Γ_i and Q_i are the corresponding linewidth and amplitude. To ensure proper thermal occupation of the phonon modes, a Bose-Einstein correction (in parenthesis) is applied to the modal sum. Selected spectral regions for analysis were defined within the intervals: $[100\,;175]$, $[170\,;280]$, $[270\,;315]$, $[300\,;380]$, $[400\,;660]$, $[790\,;820]$ and $[900\,;955]\ cm^{-1}$. Along the fitting process, adjustments were made to the predefined regions if necessary to retain an appropriate fit of the available data.

Further, we evaluated the structural phase transition around 790 K reported for RNNO [18] and the related lattice dynamics by probing the evolution of the sample's Raman profile with temperature, a sequential plot of measured spectra is shown in Figure 3.11, separated in steps of $180\ K$. As the temperature increases, it is expected for modes to undergo

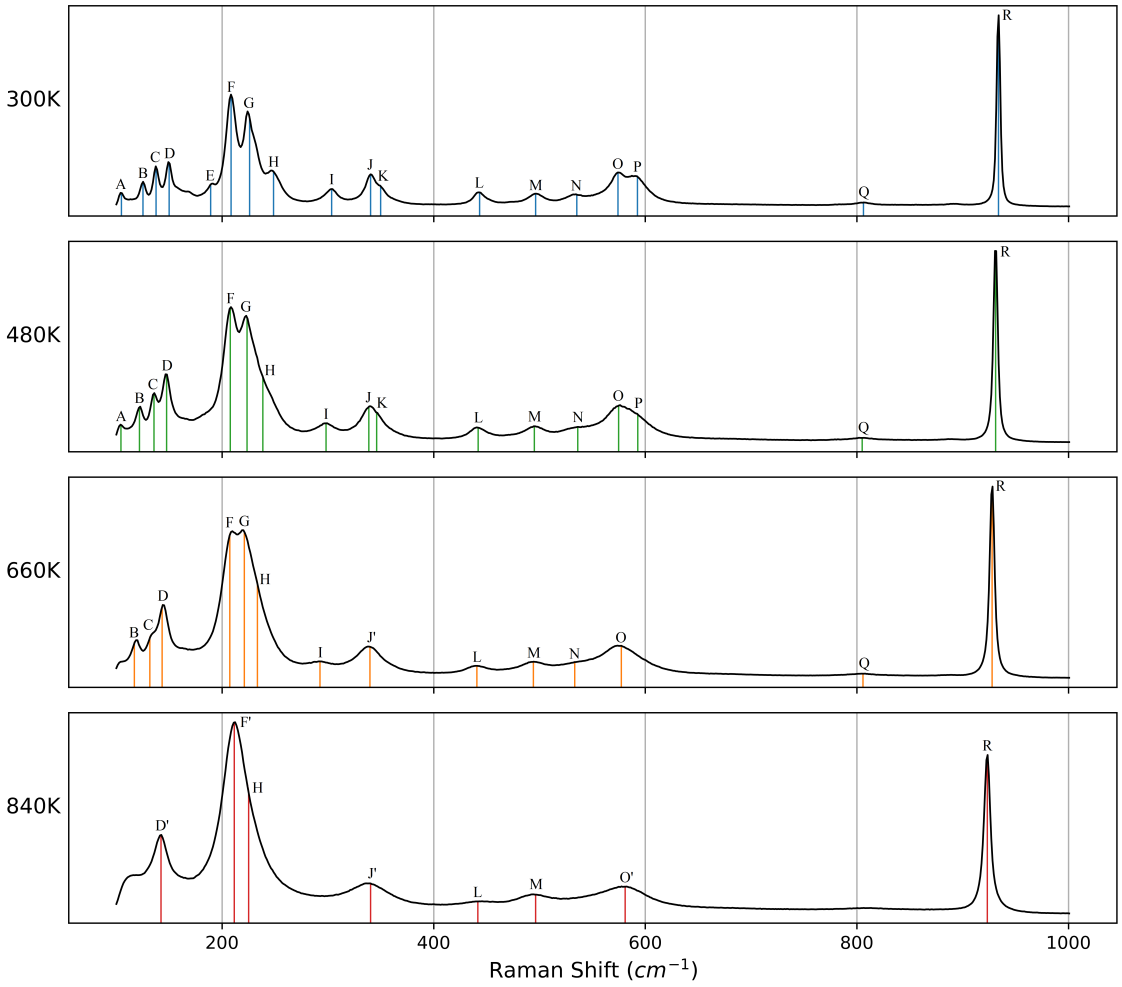

Figure 3.11: Normalized Raman spectrum of $RbNdNb_2O_7$ measured at $T = \{300\,;480\,;660\,;840\}\ K$. Modes identified for each spectrum are evidenced by the colored lines.

a decrease in frequency (red-shift) as a result of the atomic bonds becoming softer, coupled with a widening of their linewidth (peak broadening). This was observed for nearly

every peak, with the exception of modes N, O and P (see Figure A.6 in Appendix A). Up until $550\,K$, modes N and O appear to undergo an overall (but very slow) blue shift, while P red-shifts until $400\,K$ and then follows the same trend as mode O. At $500\,K$, O and P start blue-shifting rapidly before merging together into mode O' at $550\,K$, at which point N suffers a sharp decrease in frequency. From then on, N seems to retain its rigidity and O' follows the expected red-shift. These trends are unusual, but the shift of peak centers show some consistency between them, so it's unlikely (although still possible) they originate from a poor fitting of the data. Other significant occurrences along the temperature range are: modes A, E and I dissipate at around 500, 360 and $700\,K$, respectively; J and K merge together into J' at $500\,K$; C and D merge into D' at $765\,K$.

Once the reported transition temperature of $790\,K$ is reached, abrupt changes in the system's modes are observed. These consist of very accentuated shifts in peak position, merging of modes or both, and are expected for a material undergoing a structural phase transition. Modes G, M and R showcased a decrease in frequency (see Figure 3.12), while J', L, M, O' and Q experienced an increase. Moreover, modes B and N seem to

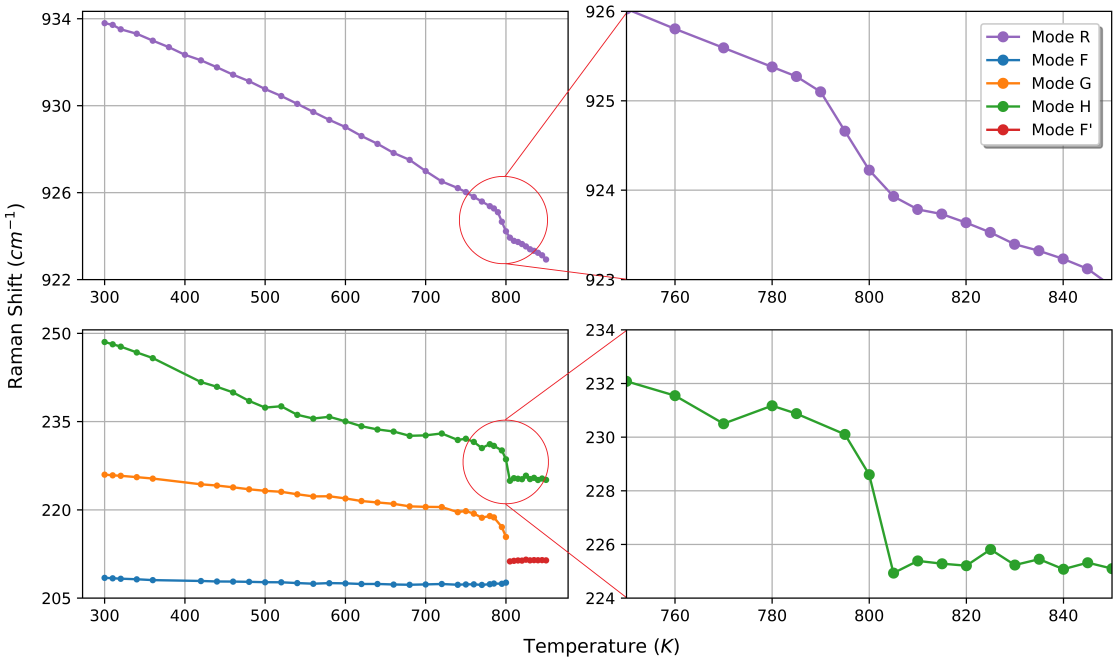

Figure 3.12: Peak position of modes F, G, H and R as a function of temperature. Abrupt changes between 790 and $805\,K$ evidence the $I2cm \rightarrow Cmca$ structural transition of $RbNdNb_2O_7$.

vanish at the transition point, which according to the movement of the peaks happens within the $[790\,;805]\,K$ range, while F and G merge into F'. Interestingly, mode D' shows

no movement at all during the phase change, which indicates that the metal oxide layers retain their rigidity throughout the phase transition.

The interesting changes, such as the increase in the frequencies associated with the J' and O' modes, can be related to the off−centering of Nb during the structural phase transition. The R mode, associated with octahedral symmetric stretching (mainly linked to axial $Nb - O_{Rb}$ bond), exhibits a sharp reduction in frequency around the phase transition, indicating an increase in $Nb - O_{Rb}$ bond length. If this behavior arises from a reduction in the degree of Nb off−centering within the octahedra, it would consequently shorten the equatorial $Nb - O$ bonds. This shortening would reflect an increase in the frequency of the asymmetric stretching around the phase transition, as the same behaviour is observed for O' mode. Additionally, such changes could induce Nd displacement, which might enhance the octahedral librations, as reflected in J' mode. Thus, our Raman spectra provide valuable insights into lattice dynamics as temperature changes and across the phase transition.

3.1.4 Heat Capacity Results

For the heat capacity measurements, small pieces were broken off from pellets of phase-pure RNNO and RNTO, and an appropriately sized one was selected for measurement in the PPMS system's heat capacity module. The RNNO sample was weighted at $(14.4 \pm 0.1)\,mg$ and the RNTO at $(16.0 \pm 0.1)\,mg$. For each sample measurement, an addenda scan was performed so that the contribution from the platform and the mounting grease could be subtracted by the PPMS software. Obtained results are presented in Figure 3.1.4, showcasing the molar heat capacity $C_{p,m}$ of the two compounds. Although the data

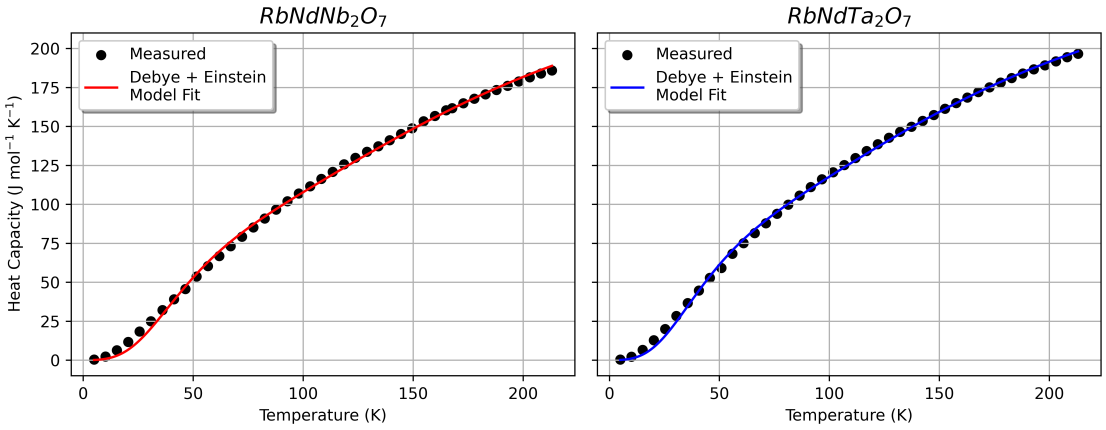

Figure 3.13: K$range, and respective fit with Equation 3.4.] Plots of the measured heat capacity for a$ RbNdNb$_2O_7$ sample (left) and a $RbNdTa_2O_7$ sample (right) in the $[5\,;215]\,K$ range, and respective fit with Equation 3.4.

were collected over the full range from 5 to $320\,K$, only values up to $\sim 215\,K$ were considered for analysis, as the grease used for mounting the samples has an optimal performance up to $200\,K$. The sample coupling factor remained above 95% for the whole temperature window, indicating the measured values are reliable. For both samples, the value of $C_{p,m}$ at $300\,K$ was bellow the isobaric Dulong-Petit limit of $R(3n+1) \sim 282.7\,J\,mol^{-1}K^{-1}$, where n is the number of atoms in the primitive cell ($=11$) and R is the molar gas constant. In the fitted $[5\,;215]\,K$ window, the heat capacity is slightly higher for the RNTO, which can be directly attributed to the higher atomic mass of Ta, in comparison to Nb.

In a first approach, the heat capacity profiles were fitted using a simple βT^3 Debye model, but it failed to describe the observed behavior in any appreciable temperature range. A more appropriate description was achieved by using a model consisting of a weighted

sum between a Debye term:

$$C_{Debye}(T,\Theta_D) \;=\; 9nR\left(\frac{T}{\Theta_D}\right)^3 \int_0^{T/\Theta_D} \frac{x^4 e^x}{(e^x-1)^2} dx \tag{3.2}$$

accounting for the contribution of acoustic modes, and an Einstein term:

$$C_{Einstein}(T,\Theta_E) \;=\; nR\left(\frac{\Theta_E}{T}\right)^2 \frac{e^{\frac{\Theta_E}{T}}}{(e^{\frac{\Theta_E}{T}}-1)^2} \tag{3.3}$$

accounting for optical modes, resulting in the expression:

$$C_{p,m}(T) \;=\; m\,C_{Debye}(T,\Theta_D) \;+\; (m-1)\,C_{Einstein}(T,\Theta_E) \tag{3.4}$$

where m is a weighting factor [57–59]. As seen in Figure 3.1.4, the fits capture the profile of the data reasonably well. Attempts to add an electronic heat capacity term γT [59], or a Schottky-like contribution (αT^{-2}) [57], to Equation 3.4 [59] did not improve the fit, indicating that neither electronic effects nor any Schottky anomalies significantly affect the heat capacity in the measured temperature range. The obtained parameters for RNNO were: $\Theta_D \sim 234\,K$, $\Theta_E \sim 674\,K$ and $m = 0.47$; while for RNTO: $\Theta_D \sim 217\,K$, $\Theta_E \sim 634\,K$ and $m = 0.49$. No direct comparison of these values could be made from the available literature.

Further studies of these samples performed at lower temperatures (possibly bellow $1\,K$), and with an externally applied magnetic field, could reveal the presence of Schottky anomalies in the heat capacity data at very low temperatures, given the splitting of the $4f$ electron states in Nd^{3+} by the Crystal Electric Field (CEF) and/or the magnetic field [58, 60]. These features can be very useful to investigate properties of these materials, providing direct insight into their low-temperature magnetic behavior, anisotropy, and lattice–magnetism coupling.

3.2. Hydrogen Ion Exchange

As detailed in the first Chapter of this thesis, a common feature of DJ-type perovskites is their ability to undergo ion exchange within the interlayer region. Owing to the wide range of possible ion-exchange reactions and intercalation processes between the quasi 2D-layers, a variety of hybrid materials as well as metastable phases can be synthesized. These characteristics also contribute to the pronounced swelling behavior of layered perovskites and enable exfoliation into 2D layers or nanosheets. In the scope of this work we carried out a soft-chemical exfoliation technique, which typically involves an initial protonation step ($H-$ion exchange), followed by exfoliation with an ultrasonication technique facilitated through the introduction of organic reagents. In the next section, we present a detailed report on the methodologies employed for the exfoliation procedures and discuss the results obtained from these experiments.

As previously mentioned, the ion-exchange process of RNNO was conducted via stirring $(99.0 \pm 0.1)\ mg$ of RNNO in a $6\ M$ solution of nitric acid ($100\ mL$), with the aim of substituting the Rb^+ ions in between the perovskite layers (octahedral bilayers) for much smaller sized protons (H^+). The XRD pattern obtained for the produced Hex-RNNO powder is shown in Figure 3.14 along with the corresponding parent sample, for comparison. The

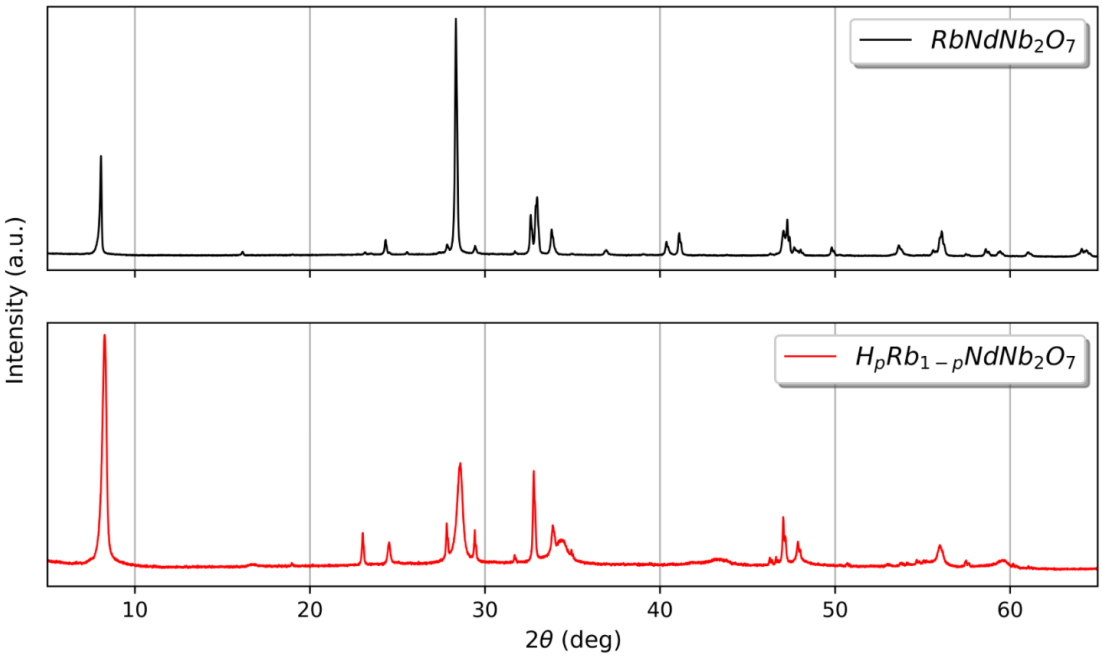

Figure 3.14: Comparison between the overall XRD spectrum (up to 70°) of $RbNdNb_2O_7$ and the one obtained from the powder of its protonated form (i.e. $HNdNb_2O_7$).

intensities are normalized with respect to the maximum value of each spectrum. At first

glance, the exchanged sample shows some good resemblance to the parent one, clearly showcasing a lot of its signature reflections. As expected however, the overall peak positions are slightly shifted and their relative intensities have varied greatly. If we start by assuming that the crystal structure doesn't change dramatically (which it appears not to) two main effects should be observed, both of them regarding diffraction peaks from reflections with a strong z-component (c axis direction in Figure 3.5): (i) a decrease in peak intensities associated with Rb^+ reflections, due to the H^+ ions being much lighter and thus having a much smaller scattering factor; (ii) a rightward shift in those peak positions as a result of a decrease in interlayer length, given the much smaller radius of H^+ ions.

If we take a closer look (see Figure 3.15), we find that some reflections have shifted rightwards and others leftwards, some increasing in intensity and others decreasing, and some even remaining practically unchanged. Although it is hard to make a direct connec-

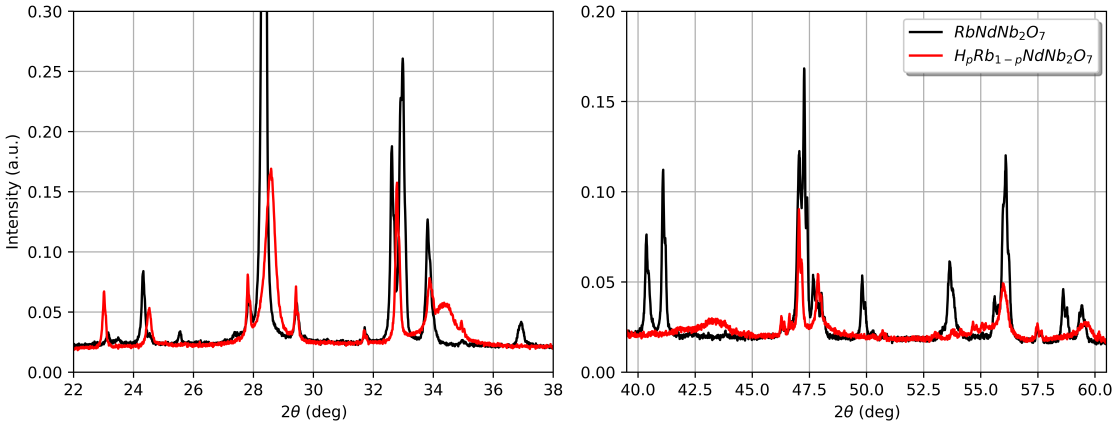

Figure 3.15: Comparison between the XRD spectrum of the $RbNdNb_2O_7$ sample and its protonated form in the 22 to 38° range (left) and 40 to 60° range (right).

tion between peaks of different spectra, we'll focus on the ones that seem more obvious. By using the VESTA software, we can simulate the pattern and see how the observed peak positions from the parent sample spectrum relate to the hkl families of planes, in order to get an understanding behind the displacement of the peaks after the ion exchange process. Reflections at $2\theta \sim \{27.8\,;29.4\,;31.7\,;57.5\}^o$ are the ones that didn't suffer any changes, which makes sense since these aren't associated with the RNNO phase but associated to the impurity phase observed the RNNO sample as mentioned in Subsection 3.1.1. The peaks that shifted to the right, indicating a decrease in interplanar spacing, also decreased in intensity, appears at $2\theta \sim \{24.5\,;28.6\,;32.8\}^o$. Peaks near 24.5^o are associated with the $[0\,0\,6]$, $[-1\,1\,2]$ and $[1\,1\,2]$ families of planes; the ones near 28.6^o with the $[1\,1\,4]$ and $[-1\,1\,4]$ planes; and near 32.8^o with the $[0\,0\,8]$ planes. Thus, it is evident that

the crystal structure of Hex-RNNO suffered a contraction along the c axis when compared with its parent counterpart. In contrast to that, a peak surged at $\sim 23^o$ that seems to have followed from a leftward shift. If such is the case, it means it's associated with the $[-1\,1\,0]$ and $[1\,1\,0]$ families of planes, which points to an increase in interplanar distance along the ab plane. Considering the decrease in interlayer distance and the closer proximity of the more intermediately sized ions (Nd and Nb), it would perhaps make sense for the structure to slightly expand in the perpendicular directions to maintain the stability of the lattice. Lastly, parent spectrum peaks near $2\theta \sim \{25.5\,;36.9\,;40.4\,;41.1\,;49.8\,;53.7\,;58.6\}$ seem to have vanished after the ion exchange. Except for the one at 25.5^o which comes from an unidentified phase (possibly RbO_3), the planes to which the remaining peaks relate to are as follows:

- $36.9^o \rightarrow [2\,0\,4]$, $[-2\,0\,4]$ and $[0\,2\,4]$ planes;
- $40.4^o \rightarrow [-1\,1\,8]$, $[1\,1\,8]$ and $[0\,1\,9]$ planes;
- $41.1^o \rightarrow [0\,0\,10]$ planes;
- 53.6 to $53.9^o \rightarrow [-2\,0\,10]$, $[2\,0\,10]$, $[0\,2\,10]$, $[-2\,2\,6]$, $[2\,2\,6]$, $[-3\,1\,2]$, and $[3\,1\,2]$ planes;
- $58.6^o \rightarrow [2\,2\,8]$, and $[-2\,2\,8]$ planes;

Since nearly all of them are attributed to lattice directions with a larger z-component, their disappearance might be explained by the expected reduction in peak intensity.

The most direct evidence for the contraction of the unit cell is, however, the very first peak of the spectra, as it is related to the $[0\,0\,2]$ family of planes, which are the ones that only contain Rb^+ ions within them (see Figure 3.5). A plot with these reflections, normalized to the highest intensity peak of RNNO's spectrum, is shown in Figure 3.16. In order to analyze the data, an asymmetrical pseudo-Voigt function was employed, coupled to a linear background. A Voigt function $V(x)$ consists of a convolution between a Gaussian and a Lorentzian curve, whereas a pseudo-Voigt is an approximation of $V(x)$ via a linear combination of the two. Thus, the function used to fit the diffraction peaks has the following expression:

$$I(x) \;=\; A\left[\,\eta\,L(x) \,+\, (1\,-\,\eta)\,G(x)\,\right] \,+\, mx \,+\, b \tag{3.5}$$

where the $mx + b$ term is the linear background, A is a scale factor, and $G(x)$ and $L(x)$ are the Gaussian and Lorentzian functions, respectively. The mixing parameter $\eta \in [0\,;1]$

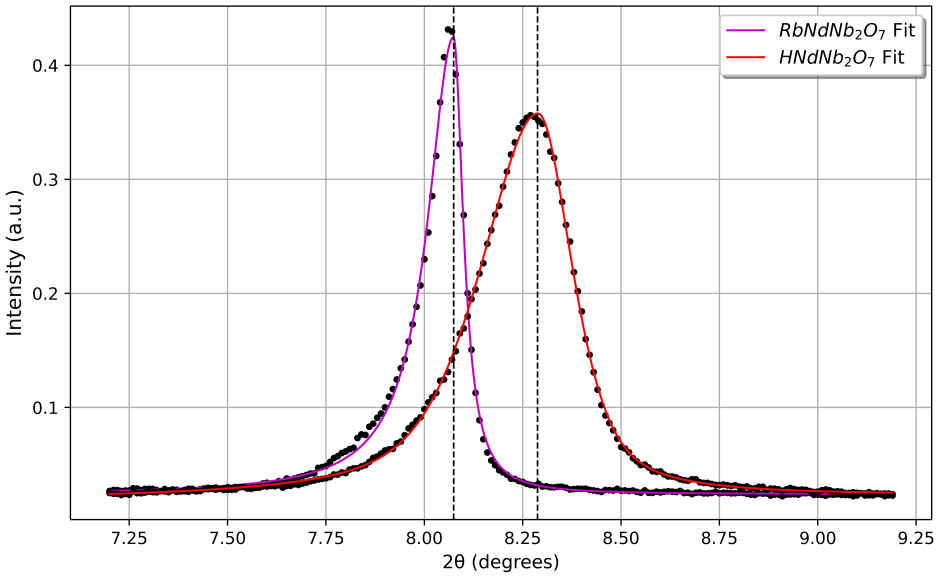

Figure 3.16: Shift of the 002 peak after protonation of the $RbNdNb_2O_7$ sample. For the parent fit $\eta = 1.0$ (full Lorentzian), $b = 0.02$ and $\delta \sim -0.45$. For the protonated sample fit $\eta = 0.6$, $b = 0.01$ and $\delta \sim -0.25$. $m = 0$ in both cases.

establishes the degree to which the fitted curve has more of a Gaussian or Lorentzian shape. Moreover, $G(x)$ was defined as:

$$G(x) = \exp\left[-\frac{1}{2\sigma^2}(x-\mu)^2\right] = \exp\left[-\frac{4\log(2)}{\omega^2}(x-\mu)^2\right] \tag{3.6}$$

while $L(x)$ was defined as:

$$L(x) = \frac{\gamma^2}{(x-\mu)^2+\gamma^2} = \frac{\omega^2}{4(x-\mu)^2+\omega^2} \tag{3.7}$$

Since we are only interested in capturing the shape of the peaks and the position of their center point μ, they do not need to be in their normalized forms. In order to account for the asymmetry in the peaks, a different full width at half maximum ω was used to fit the points left and right of center. This also enabled us to quantify how asymmetric the peaks were, by determining the quantity:

$$\delta = \frac{w_{left} - w_{right}}{w_{left} + w_{right}} \tag{3.8}$$

The $[0\,0\,2]$ peak position for RNNO was then estimated at $2\theta_{Rb} \sim 8.07^o$, while the one from Hex-RNNO was at $2\theta_H \sim 8.29^o$. This translates to a total shift of $\Delta(2\theta) \sim 0.22^o$, which considering Bragg's law from Equation 2.2, accounts for a $0.29\,\AA$ decrease in interlayer spacing. Zhang et al. reported a $\Delta\theta \sim 0.4^o$ shift for this peak [27], using the same operational wavelength ($\lambda = 1.54059\,\AA$).

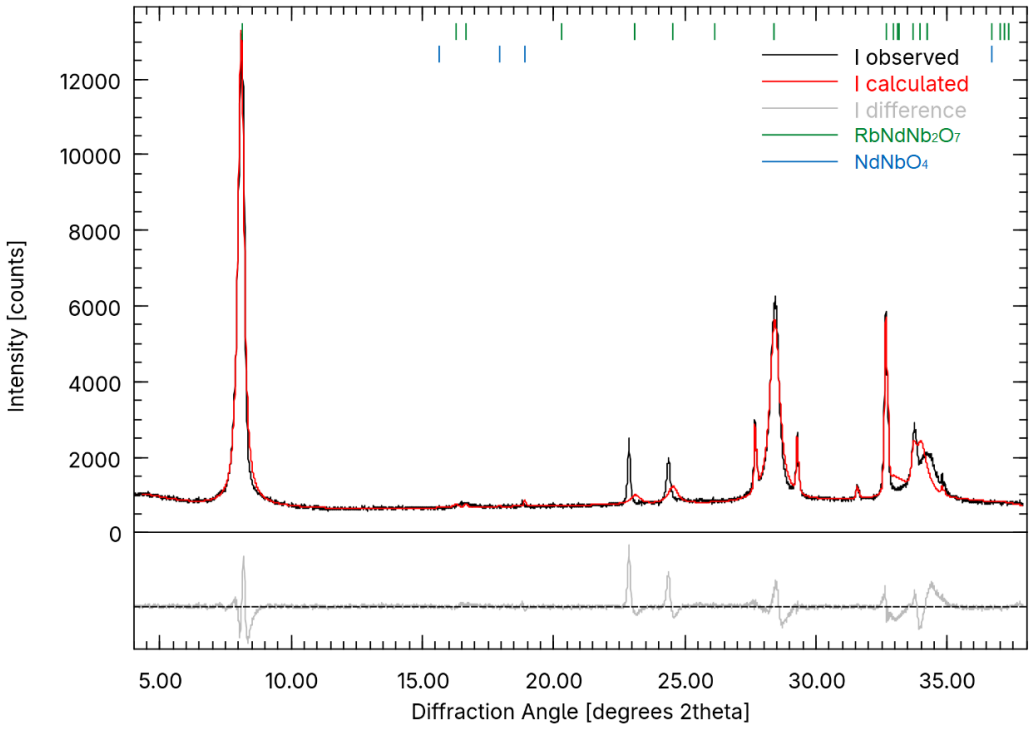

Figure 3.17: Rietveld refinement spectra of the protonated $RbNdNb_2O_7$ sample.

This discrepancy was later investigated further with a Rietveld refinement of the spectrum (see Figure 3.17), by computing a hydrogen exchange in the Rb site as $Rb_{1-p}H_p$. The phase quantity of the $NdNbO_4$ impurity was fixed at the previously found value of $\sim 5\%$, and the spectrum was refined up to $2\theta = 38^o$ to focus on the highest intensity peaks, since they should be the most influenced by the proton substitution. The best fit resulted in: $R_{wp} = 10.32$, $R_{exp} = 3.18$ and $\chi^2 = 10.53$. Naturally, the agreement is not particularly good due to the already discussed deviation of the sample's profile when compared with its parent compound, with peaks near $2\theta = \{22.8\,;24.4\,;34.4\}$ being poorly reproduced. The refinement returned a substitution parameter $p = (0.89 \pm 0.02)$, which would indicate that $\sim 90\%$ of the Rb^+ was replaced. This is slightly below our initial assumption of a nearly complete exchange. Moreover, this value should be treated with caution, as by varying the refinement strategy (parameters, constraints, fitting range, etc.), values of p as low as 0.7 were also obtained.

It should be emphasized that this analysis compares Hex-RNNO with its parent structure ($I2cm$) as the reference. However, given the substitution of larger Rb^+ ions for smaller H^+ ions, the actual crystal structure of Hex-RNNO may differ significantly from the parent compound. Definitive determination of the true structure would require DFT-based crystal structure prediction and confirmation via high-quality synchrotron or NPD, which were

beyond the scope and time frame of the present study and are reserved for future work. Nevertheless, the observed differences in the XRD patterns (also confirmation of unit cell contraction) provide clear evidence of successful protonation of the layered perovskite.

3.3. Exfoliation Attempts and Findings

In this section, the results of the exfoliation processes are presented and analyzed, including observations from all intermediate steps. Also, the ultrasonication based exfoliation was carried out following two distinct protocols. For RNTO, the samples were directly ultrasonicated using the organic solvent NMP. However, for RNNO, the protonated sample (Hex-RNNO) was considered for exfoliation using the organic reagents NMP and TBAOH. Exfoliation experiments and results from RNTO are addressed first, followed by those from RNNO. The characterization includes XRD, Raman spectroscopy, SEM and other relevant techniques.

3.3.1 $RbNdTa_2O_7$-based Samples

As mentioned earlier, the initial attempt of exfoliation was performed using RNTO. Following the ultrasonication technique, an ultrasonicator with a $12\,mm$ tip was employed, which requires a solution volume of $20 - 250\,mL$ (manufacturer specification). Accordingly, an $80\,mL$ NMP solution was prepared in a beaker, in which $(250.5 \pm 0.1)\,mg$ of RNTO powder was dispersed. The ultrasonicator was operated for $10\,min$ duration with a pulse sequence of $30/5\,s$ ON/OFF periods, at 50% of its maximum amplitude. During sonication, the solution temperature was monitored, reaching approximately $70\,^oC$ in $9\,min$. To reduce excessive heating, a second sonication run was performed under identical settings, with the beaker placed inside a larger water-filled container and stabilized using styrofoam. This modification resulted in a lower average temperature of $40\,^oC$, also the solution was allowed to cool between sonication runs. After a total of $20\,min$ of ultrasonication time, the solution was centrifuged at $10\,000\,rpm$ for $3\,min$, and the resulting supernatant was collected for further analysis.

Subsequently, three distinct samples were prepared on glass substrates for XRD measurements: The three sample depositions were (i) pure NMP; (ii) RNTO dispersed in NMP; (iii) and the collected supernatant. Prior to deposition, the glass substrates were thoroughly cleaned following a three step process: first a $10\,min$ ultrasonic bath in deionized water; then in 99% ethanol; and finally in acetone. After drying, the substrates were placed on a hot plate at $90\,^oC$ inside a hotte, and a few drops of each sample were cast onto the surface. The temperature was then increased to $110\,^oC$ and left overnight.

On the following day, samples were collected and XRD patterns were recorded. The resulting diffraction patterns are presented in Figure 3.18 along with the parent RNTO

diffraction pattern for comparison. Expectedly, the pure NMP exhibited an amorphous

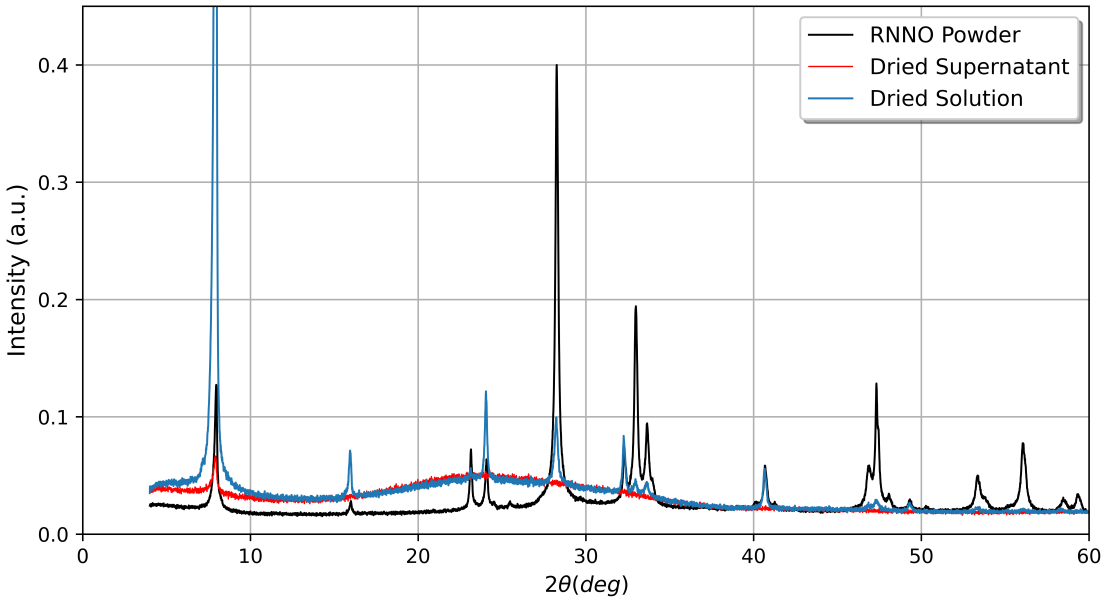

Figure 3.18: XRD spectra for a dried solution of $RbNdTa_2O_7$ in NMP, and the corresponding supernatant collected after centrifugation, in comparison to its powder form spectrum.

profile (not shown in the graph), most probably coming from the glass substrate. The same exact profile is found in the patterns of (ii) and (iii), corresponding to the RNTO in NMP and the supernatant, respectively. If we compare sample (ii) with the parent powder, we see that all the RNTO signature peaks are present, with changes only in their relative intensities. Sample (iii) on the other hand, showcases only the peak corresponding to $[0\,0\,2]$ lattice planes, while other characteristic peaks are significantly diminished or absent (mostly likely hidden by the amorphous scattering). Since there is no significant peak broadening nor peak shift for the $[0\,0\,2]$ lattice plane, no definitive conclusions can be drawn from this XRD analysis regarding the presence of exfoliated material in the supernatant.

From this point onwards, the Rigaku Smartlab diffractometer became unavailable due to a technical issue with one of its components. As such, we were mostly limited to Raman spectroscopy and SEM. New samples were produced from the RNTO solution, repeating the ultrasonication and centrifugation steps in a similar manner, although this time the supernatant was drop cast in both a glass and Si substrates. Furthermore, two sets of these were prepared, where half of them were immersed in an aqueous Polyethylenimine (PEI) solution for $\sim 30\,min$, akin to how Kurnosenko et al. [39] carried out the deposition of their nanosheets. The principle behind this is that, since PEI is a cationic polymer when

dissolved in water, it should behave like an adhesive to the exfoliated sheets, which are negatively charged. Developed samples were later taken for Raman measurements, with results shown in Figure 3.19. None of the exfoliation-related samples (derived from the

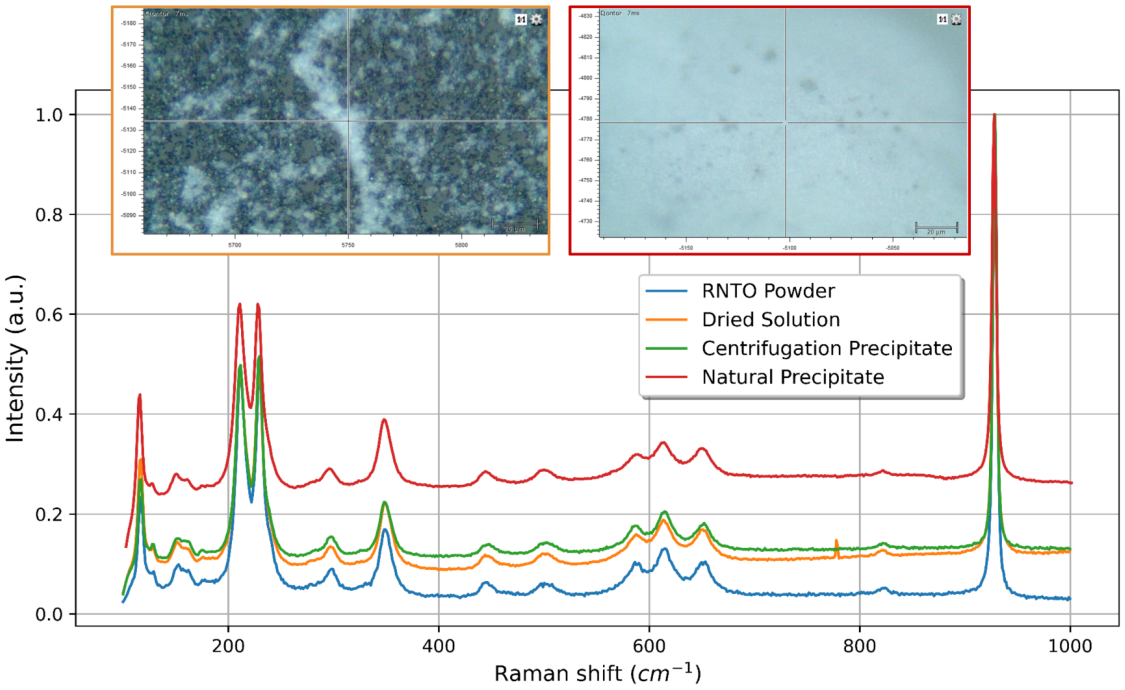

Figure 3.19: Measured Raman spectra of $RbNdTa_2O_7$-based samples: (i) Parent powder form (blue); (ii) Dried NMP solution (orange); (iii) Precipitant from centrifugation (green); and (iv) Precipitant from natural precipitation (red). Images display the spots were the measurement was performed.

supernatant solution after ultrasonication) exhibit any relevant signal, other than the peak stemming from the Si substrate at $\sim 520\,cm^{-1}$. On the other hand, we collected good spectra for other samples of RNTO derived at different stages of the exfoliation process, including: (i) Parent RNTO powder; (ii) dried RNTO in NMP solution, measured previously in XRD; (iii) precipitant residue collected after centrifugation of the ultrasonicated solution; and (iv) natural precipitant from the ultrasonicated solution. The natural precipitant was measured at much later time, since it was collected after the solution was left behind for a 1 to 2-month period for natural settling. Since the obtained spectra is pretty much identical between all of them, we can infer that the overall integrity of the RNTO crystal structure was maintained throughout the different processes.

Although we weren't able to measure their Raman spectra, one of the exfoliation samples was observed in SEM, specifically the one drop cast in a Si substrate without the PEI treatment. Obtained images are shown in Figure 3.20. EDS spectra was not collected for this sample, but we can see from the pictures that the general size of the observed

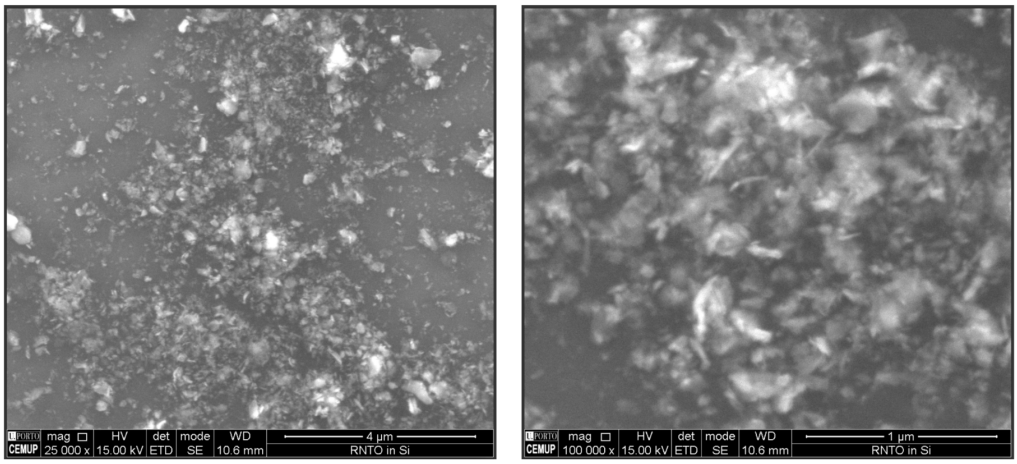

Figure 3.20: SEM images captured for the drop cast supernatant of a $RbNdTa_2O_7$ in NMP solution, dried in a Si substrate.

features is well under the micrometer range. It was also the case for the bulk powder (Figure 3.8), even though there appears to have been a reduction in feature size, likely resulting from the ultrasonication. This result is suggestive of a successful exfoliation, but other methods or higher resolution techniques like Tunneling Electron Microscopy (TEM) are required to confirm this, while Atomic Force Microscopy (AFM) should provide proper measurements of feature size. These characterizations are planned for future work.

To further access the presence of suspended exfoliated material in the supernatant solution, we carried out a light dispersion (Tyndall effect) test [61]. This consisted of simply aiming a collimated light source (a domestic laser, in this case) at the colloidal suspension and see if the light is dispersed by the medium. We can clearly see from Figure 3.21

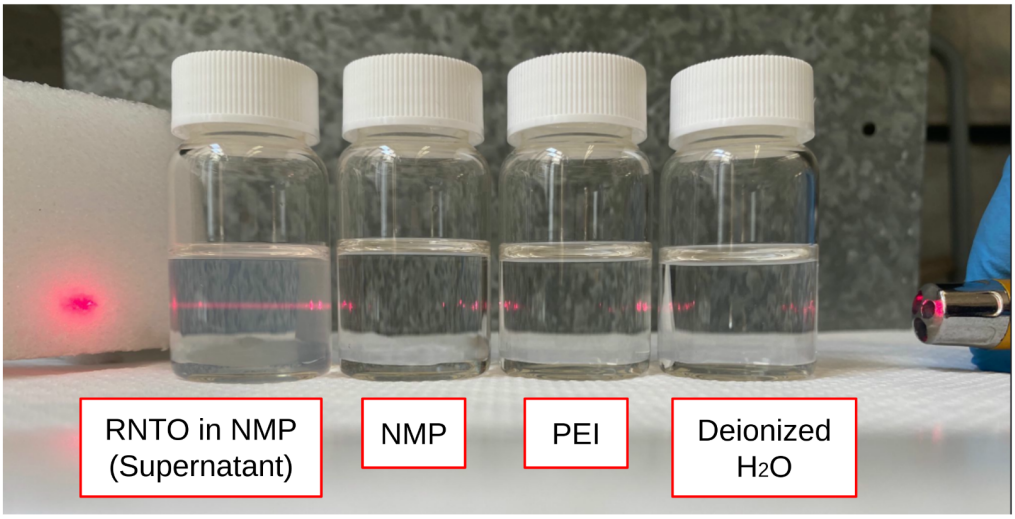

Figure 3.21: Laser dispersion test evidencing the presence of suspended exfoliated material in the $RbNdTa_2O_7$ NMP solution's supernatant.

that this dispersion only occurs for the supernatant solution, and not for any of the other

chemical solutions used. Assuming that any and all bulk pieces of RNTO compound were successfully separated during centrifugation, this test then provides a solid indication that suspended exfoliated material remains in the supernatant solution.

Later on, we had the opportunity to send some samples to the University of Minho for XRD measurements. Two of them were the parent powder and the dried precipitant (from natural precipitation), which we had measured with Raman. Results from Figure 3.23 solidify

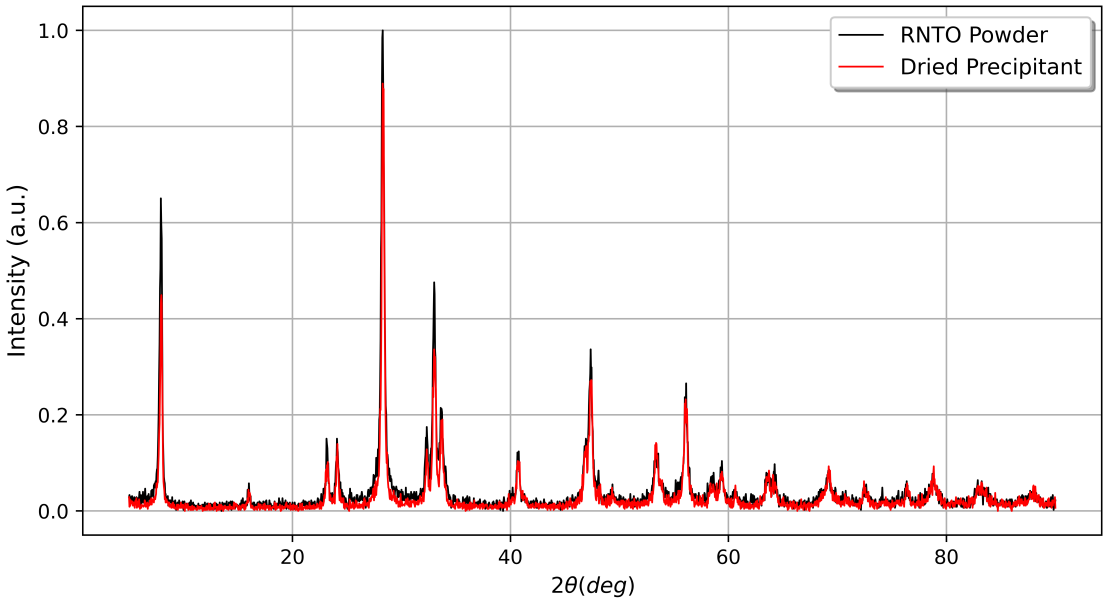

Figure 3.22: XRD spectra of $RbNdTa_2O_7$ parent powder and natural precipitant from the NMP solution, both measured at University of Minho.

what we had concluded from the Raman measurements, in that there is no evidence of structural changes or degradation of the RNTO material, even after several steps of stirring, ultrasonication and centrifugation.

The other two samples measured were from drop cast supernatant solution. To enhance the diffraction peaks and to minimize the amorphous scattering from the exfoliated material, we tried an alternative setup for the drop casting procedure. The aim was to confine the liquid in one region so that the exfoliated material would be dispersed in a smaller region, and thus more concentrated. This was achieved by placing the glass substrates under a structure with small cylindrical holes (referred to as ”Alumina setup”), $\sim 1\,cm$ in diameter, that kept the liquid within a confined space. O-rings were fitted at the interface between the structure and the substrates, to prevent leakage of the fluid. We also added a lot more drops, both for this setup and the regular drop casting one. For sample drying, the hot plate temperature was increased to $300\,^oC$ as well. As seen in Figure 3.23, this pro-

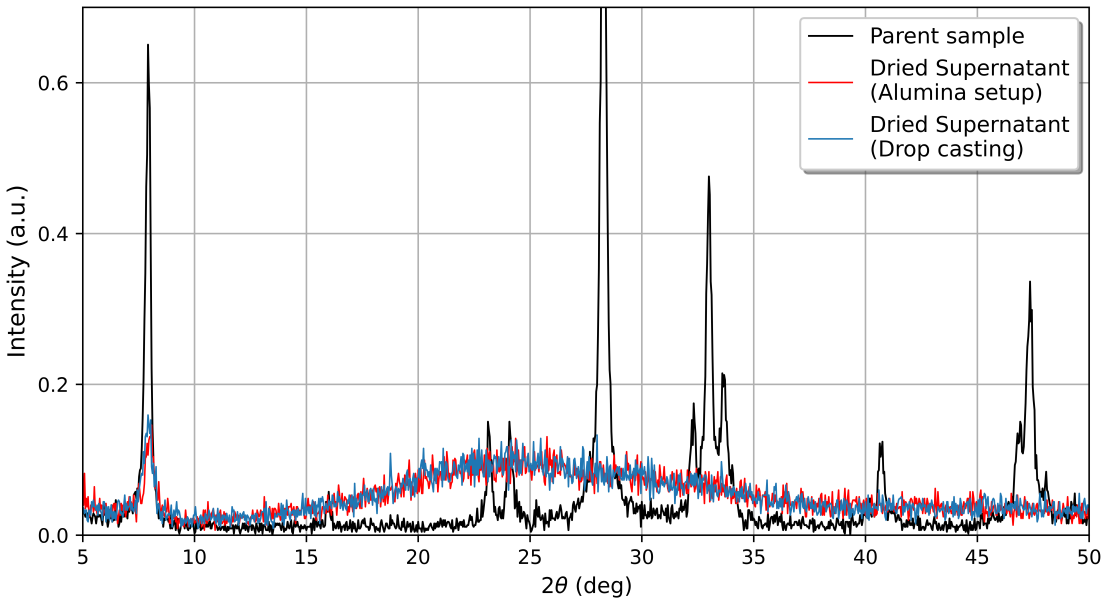

Figure 3.23: XRD spectra of dried supernatant samples from the $RbNdTa_2O_7$ NMP solution, one with the ”Alumina setup” (red) and the other with regular drop casting (blue). Parent sample spectrum is shown for comparison.

cedure did not make any difference in the measured spectra, and both methods yielding an identical result to the first attempt (Figure 3.18). It became apparent at this stage that, in order to get a proper XRD spectrum of the exfoliated material, a more sophisticated deposition process was required.

The regular drop cast sample was also viewed in SEM, with images and respective EDS spectra shown in Figure 3.24. Overall feature size is under $500\,nm$, indicating more clearly the effects of the ultrasonication process. The EDS spectra presents a lot of extra signatures, mostly coming from the glass substrate which is known to contain Na, Si, O and Ca. The C and some of the O signal is from the NMP, but we couldn't find an explanation for the extra Cl impurity. Considering the exfoliation of bulk particles of RNTO, we could perhaps expect a lower ratio of Rb, released from the separation of perovskite layers. However, the spectra shows approximately the same quantity of Rb and Nd (1:0.73, respectively), which is contrary to that. Nevertheless, the notable reduction in feature size presents a positive sign toward the exfoliation of RNTO into multilayer sheets. As mentioned earlier, only with TEM and AFM can we assess these results more clearly.

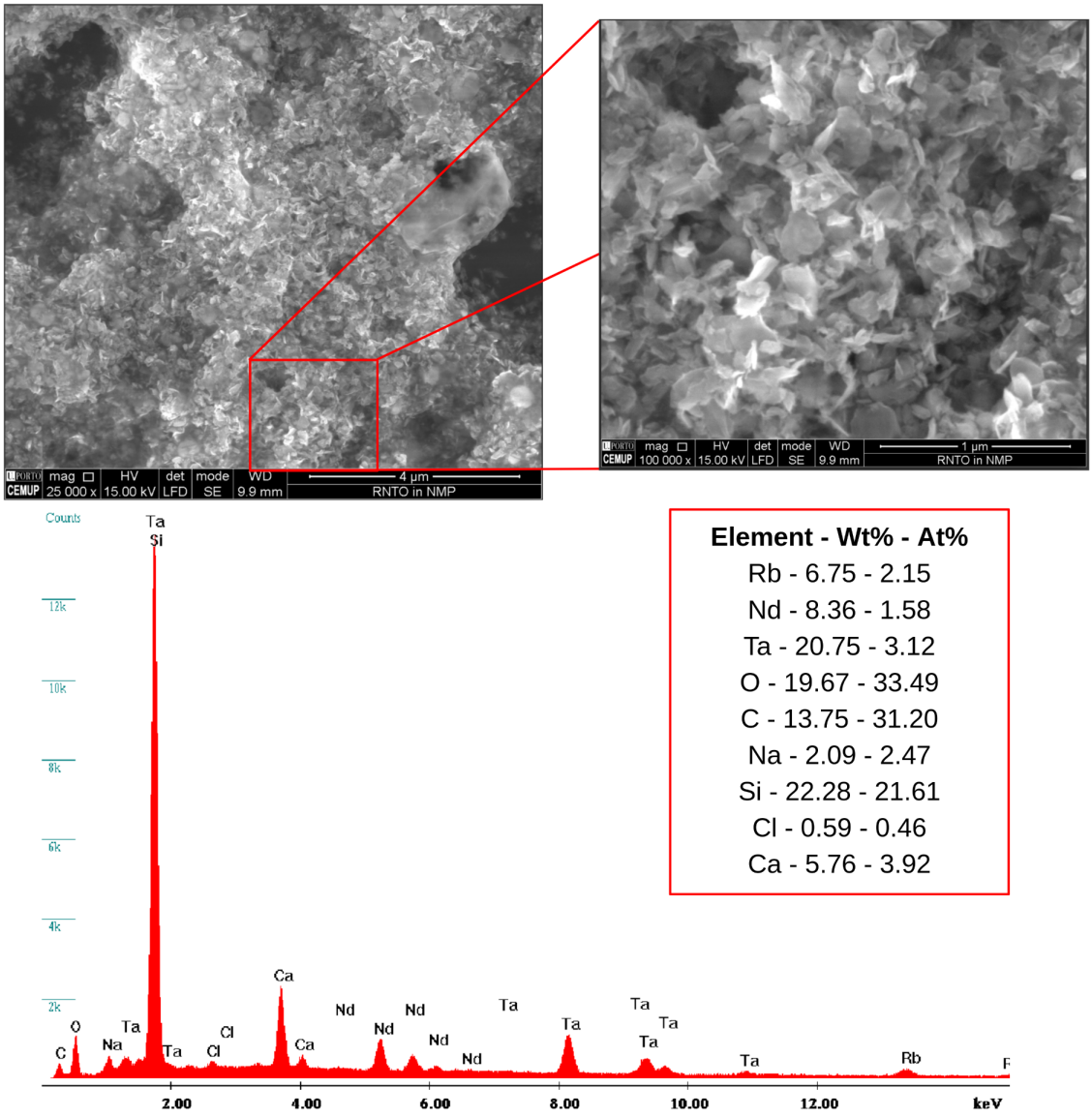

Figure 3.24: SEM images and EDS spectra of drop cast supernatant from a $RbNdTa_2O_7$ in NMP solution, dried in a glass substrate.

3.3.2 $RbNdNb_2O_7$-based Samples

Moving on to RNNO, the exfoliation attempts were first carried out in NMP using Hex-RNNO powder. $(0.011 \pm 0.001)\,g$ of the powder was added to $15\,mL$ of NMP solution, and stirred overnight using a magnetic stirrer at $300\,rpm$ (ambient temperature). For the exfoliation, the same procedure used for RNTO was followed, running two $10\,min$ ultrasonication programs (same settings) with cooling in between, followed by two centrifugation cycles of $3\,min$ at $10\,000\,rpm$. The supernatant became noticeably more transparent after the second cycle. Then, both PEI treated glass and Si substrates were dip coated with the supernatant. The SEM images obtained for the dried supernatant, dip coated on Si

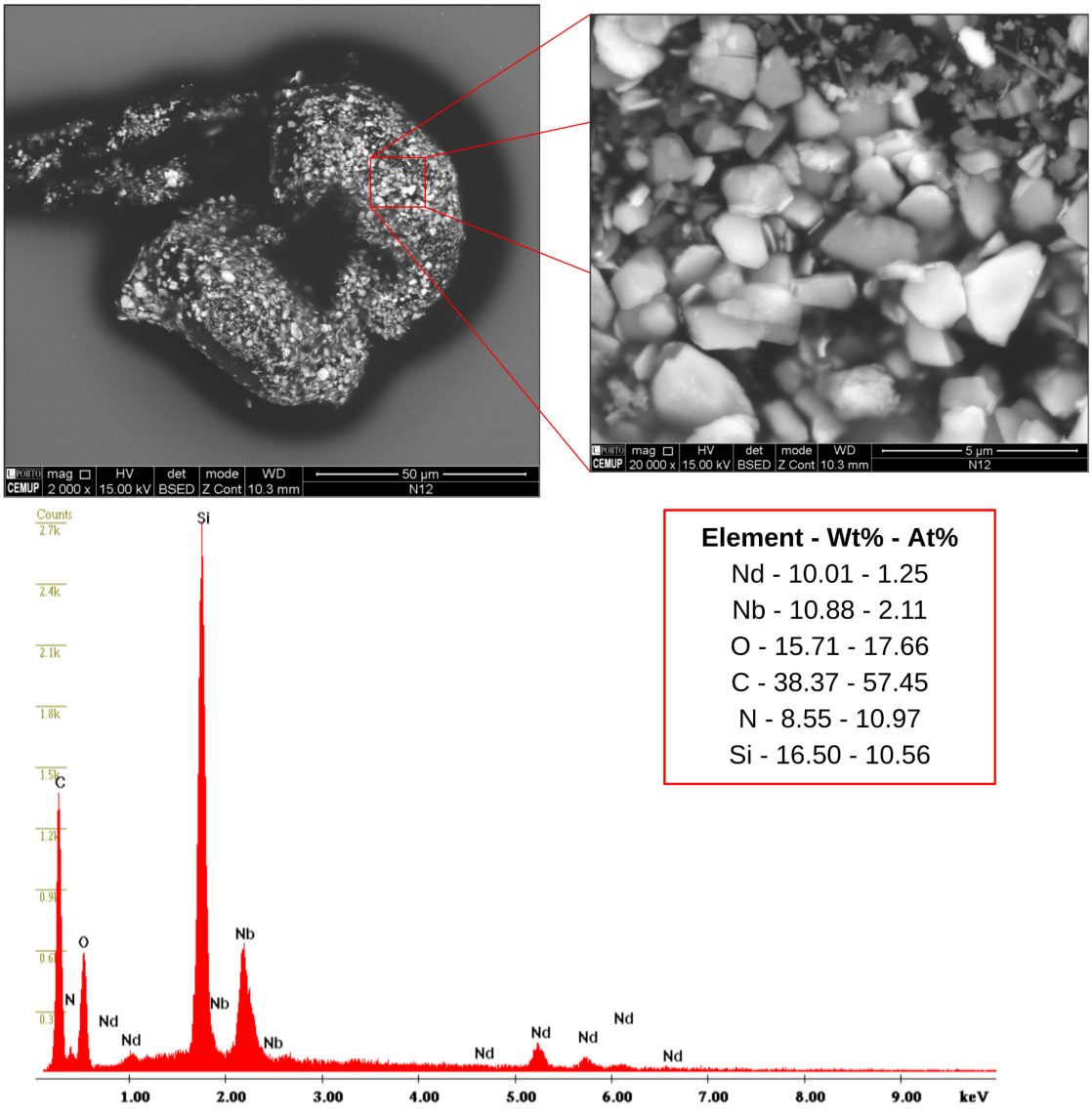

Figure 3.25: SEM images captured for the supernatant of protonated $RbNdNb_2O_7$ in NMP solution, deposited on a PEI treated Si substrate via dip coating. It showcases the large clusters observed, and a corresponding EDS spectrum.

substrate, exhibited: (i) large clusters of small platelets (similar to the ones observed for the parent powder, in Figure 3.7); and (ii) small isolated dots, consisting of a few flakes of material when seen up close. The SEM image corresponding to case (i), with the respective EDS spectrum, is shown in Figure 3.25. On the left side image we can see the large cluster with a dark contour around it, which corresponds to the PEI polymer. Looking at the EDS spectra, it shows the strongest peak from Si, which is expected considering the deposited material is only a very thin layer on top of the substrate. It shows the same Nd, Nb and O peaks observed for the parent sample, although less intense, and the new C and N peaks come from the NMP. Notably though, there is an absence of Rb signal, which is a strong evidence that the ion exchange (protonation) reaction was successful. Figure 3.26 shows an example for case (ii), representative of several observations across

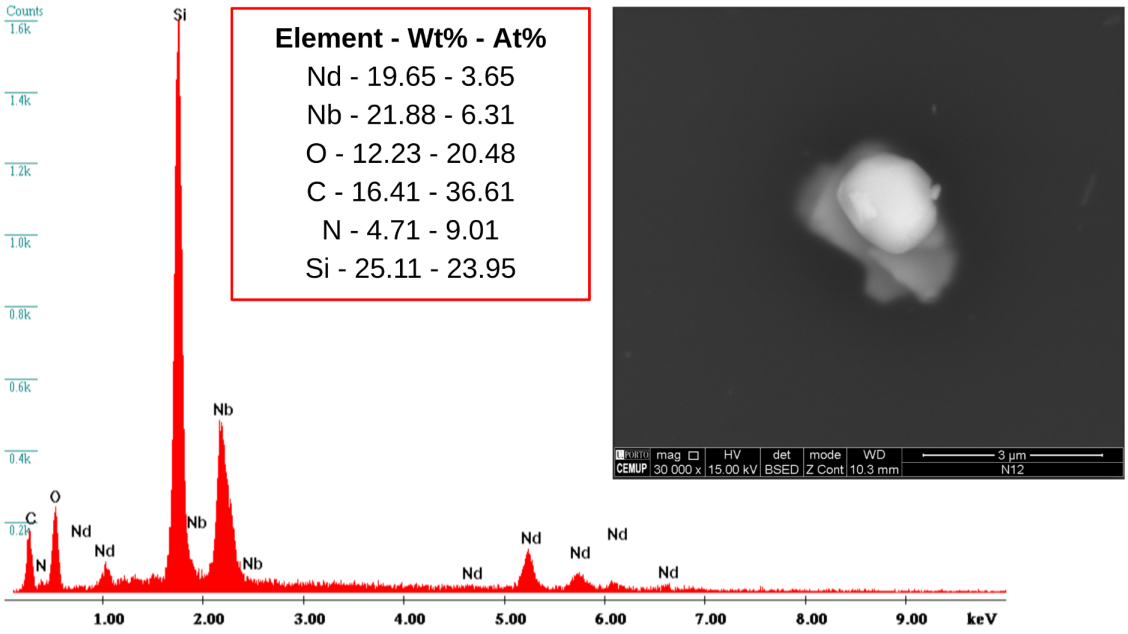

Figure 3.26: SEM images captured for the supernatant of protonated $RbNdNb_2O_7$ in NMP solution, deposited on a PEI treated Si substrate via dip coating. It showcases one of many isolated pieces of material found, and a corresponding EDS spectrum.

the scanned sample area. The observed flakes exhibit lateral dimensions comparable to those observed in the cluster. From multiple images viewed during the SEM scan, no clear correlation was observed between lateral size and the agglomeration of material. The feature appears to consist of a stack of few individual flakes, although no definitive conclusions can be drawn regarding their thickness, as that would require other methods or measurement techniques. Much like the previous example, the EDS spectrum shows no signs of Rb as well. In terms of exfoliation, these results do not allow us to conclude that nanosheets have been obtained, since we have no measure of the obtained structure's thickness. It might be unlikely, however, since the lateral size observed for nanosheet

examples is typically inferior to $1\,\mu m$. We later tried to analyze this sample with Raman, but we weren't able to collect an appropriate spectrum.

Next, we tried a different approach for the exfoliation of Hex-RNNO, using the organic salt TBAOH. For that we mixed $\sim\ 50\,mg$ of Hex-RNNO powder in $100\,mL$ of a $0.3\,M$ aqueous solution of TBAOH (Sasaki et. al [38] used concentrations between 0.02 and $0.5\,M$), and left it stirring overnight at $200\,rpm$. The following day, for the exfoliation, we used a $30\,min$ program with a $30/5\,s$ ON/OFF cycle at a 60% amplitude. Temperature after the first ultrasonication run was slightly above 40^oC. A total of four ultrasonication runs were performed prior to centrifugation and sample deposition. The second and third ultrasonications were conducted on separate days. Notably, before commencing the third run, it was observed that the Hex-RNNO in the solution had naturally precipitated, leaving a transparent supernatant. This behavior contrasts with the exfoliation process using NMP, where such spontaneous precipitation occurred only after a significantly longer time period. Another notable difference compared to the NMP solutions was the higher volatility of TBAOH. By the end of the fourth and final ultrasonication, the solution temperature was approximately $50\,^oC$ and roughly about $20\,mL$ of solvent had evaporated. For the centrifugation, two cycles of $10\,min$ runs at $10\,000\,rpm$ were performed. The supernatant became significantly more transparent after the second centrifugation.

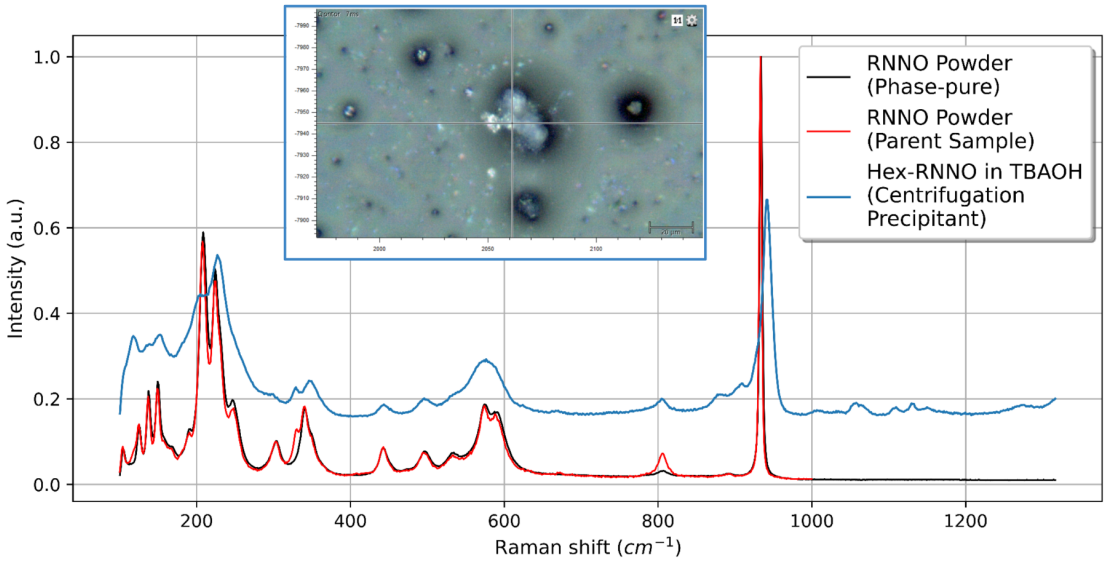

Figure 3.27: Raman spectra of the dried precipitant (from centrifugation) of a $HNdNb_2O_7$ in TBAOH solution, in comparison to the spectrum of the phase-pure $RbNdNb_2O_7$ sample.

The precipitant was analyzed using Raman, with results presented in Figure 3.27. As

shown in the spectra, most vibrational modes are preserved and appear at positions consistent with the parent material, although the peaks are noticeably broader in the precipitant case. Raman peaks associated with the TBAOH salt are above $1000\,cm^{-1}$, and the differences in spectra bellow that can have two possible explanations: (i) either they stem from the structural changes following the H exchange; or (ii) they stem from the intercalation of TBA^{+} radicals in the interlayer space, which is promoted during the initial stirring of the solution. To determine which phenomenon is more directly responsible for it, other measurement techniques have to be employed. In parallel, we can also see a very good agreement between the profile of the phase-pure RNNO and the impure one (parent powder), which further confirms the very high percentage of the main RNNO phase, while also affirming the suitability of its use for this work.

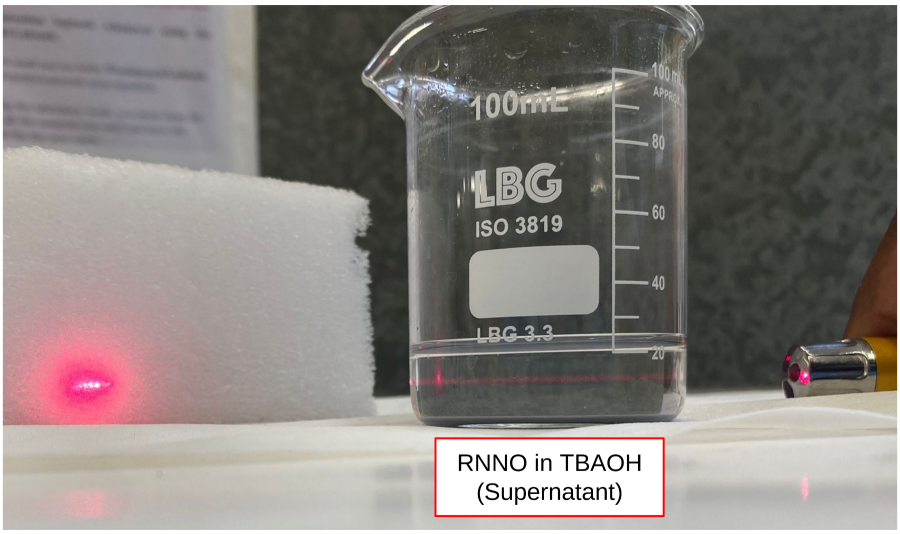

Figure 3.28: Light dispersion test (Tyndall effect) evidencing the presence of suspended exfoliated material in the $HNdNb_2O_7$ TBAOH solution's supernatant.

The light dispersion test for the presence of the Tyndall effect in the supernatant solution is shown in Figure 3.28. Although not very clear from the picture, there is actually dispersion of the laser's light, confirming that we had suspended exfoliated material. This was not observed for the TBAOH-only solution.

Further, we carried out some XRD measurements at the University of Minho for the parent RNNO and dried precipitant from TBAOH exfoliation (previously analyzed with Raman), shown in Figure 3.29. Comparing the two spectra, the diffraction pattern from the dried precipitant after exfoliation exhibits a similar signature to the parent RNNO, although with noticeable shifts in the diffraction peak positions. The peak shifts obtained for the dried precipitant differ from those observed for Hex-RNNO in comparison with parent RNNO

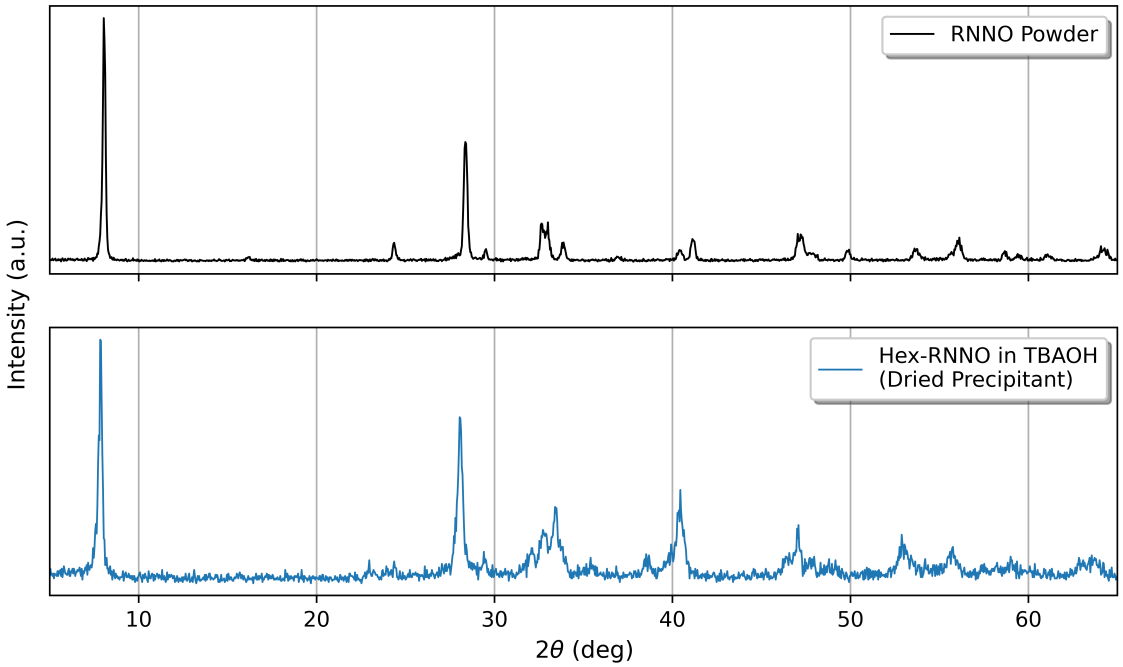

Figure 3.29: Comparison between the overall XRD spectrum (up to 70°) of $RbNdNb_2O_7$ and the one obtained from the dried precipitant of the centrifuged $HNdNb_2O_7$ in TBAOH solution (after exfoliation).

(Figure 3.14 and 3.15), as the overall shift in 2θ is in the opposite direction (toward lower angles) for the dried precipitant. A closer examination (see Figure 3.30) shows that, with the exception of the impurity peak at $2\theta \sim 29.4^o$, which remains unchanged, all the other diffraction peaks shifted towards lower angles to some degree. These observa-

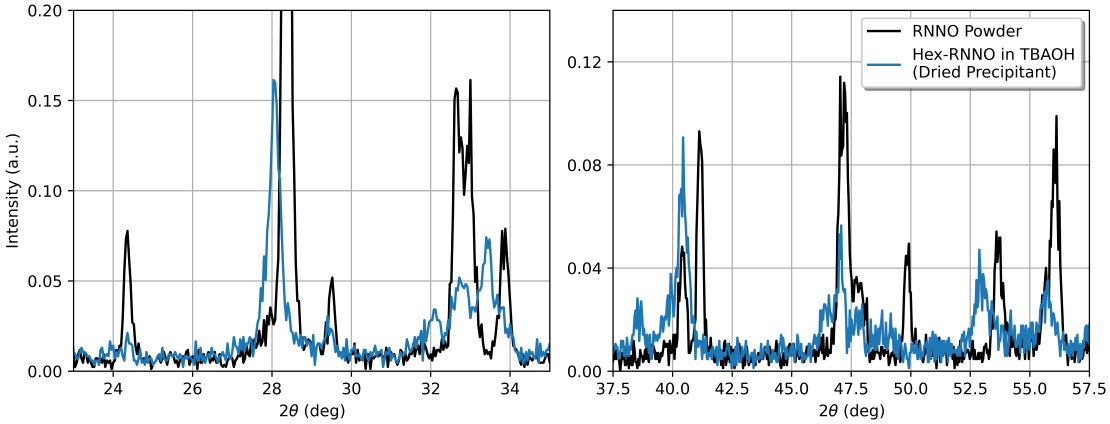

Figure 3.30: Comparison between the XRD spectrum of the $RbNdNb_2O_7$ sample and dried precipitant of the centrifuged $HNdNb_2O_7$ in TBAOH solution (after exfoliation), in the 23 to 35° range (left) and 37.5 to 57.5^o range (right).

tions strongly suggest that the structural changes, observed in the Raman spectra from Figure 3.27, are a consequence of TBA^+ intercalation.

Using the same approach we employed to find the change in interlayer spacing during the protonation step, we estimated the increase in interlayer spacing resulting from TBAOH intercalation into Hex-RNNO by tracking the shift of the $[0\,0\,2]$ diffraction peak. After fitting

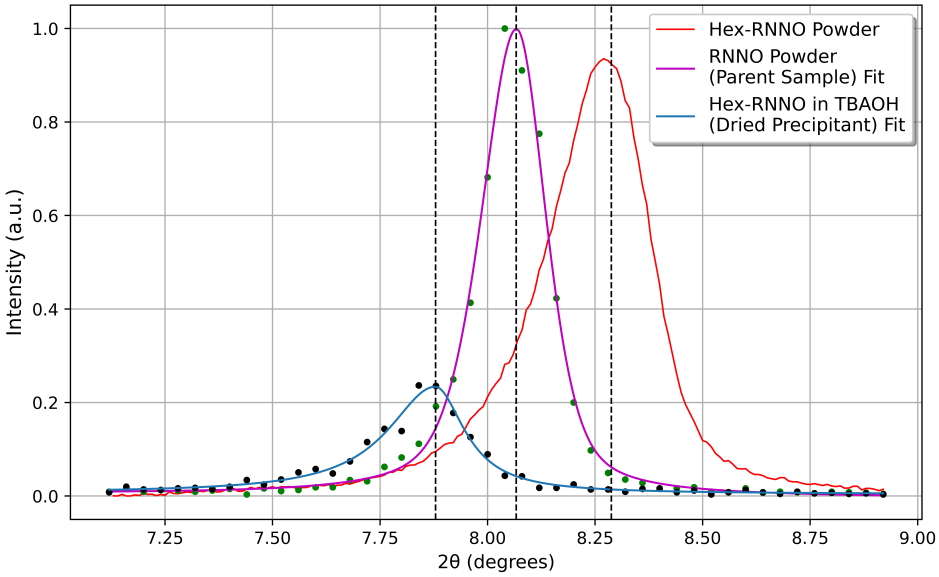

Figure 3.31: Shift of the [002] peak following from intercalation of TBA^+ radicals between the $NdNb_2O_7$ layers. For the parent fit: $\eta = 0.49$, $b = 0.03$ and $\delta \sim -0.09$. For the intercalated sample: $\eta = 1.0$ (full Lorentzian), $b = 0.01$ and $\delta \sim -0.23$. $m = 0$ in both cases. The same reflection from Hex-RNNO is also shown for comparison.

the corresponding reflection in each spectrum (Figure 3.31), peak positions were found at $2\theta_{Rb} \sim 8.07^o$ for the RNNO powder (consistent with the previous result) and at $2\theta_{TBA} \sim 7.88^o$ for the dried precipitant. This corresponds to a total shift of $\Delta(2\theta) \sim 0.19^o$, or a $\sim 0.26\,\mathring{A}$ increase in interlayer spacing. Reported values for this shift in literature are significantly larger, suggesting that the intercalation of the bulky TBA^+ radicals was very partial. Achieving a more extensive intercalation would likely require prolonged stirring in the TBAOH solution.

Finally, two additional samples from exfoliation attempts of this material were prepared, but their measured XRD spectra consisted solely of an amorphous background. Although it is possible that the Hex-RNNO was successfully exfoliated, these results once again imply that a more sophisticated deposition method is required to produce a sufficiently good sample for standard characterization techniques. In this regard, a study by Shi et al. [62] provides a path forward by presenting a single droplet assembly method for nanosheet production. Moreover, using higher concentrations of bulk powder, as well as centrifuging at lower rpms (since we might have precipitated some of the exfoliated material), are steps to be considered for future attempts.

4. Conclusions and Future Work

In this work, we were able to characterize and study structural properties of the $n = 2$ Dion-Jacobson layered oxide perovskites $RbNdNb_2O_7$ and $RbNdTa_2O_7$, employing a combination of experimental techniques such as X-ray Powder Diffraction, Raman Spectroscopy, Scanning Electron Microscopy and Heat Capacity Measurements. We confirmed that both compounds stabilize in the $I2cm$ space group at room temperature, and determined the corresponding lattice parameters. In SEM, we've observed the morphology of these two materials in their powder form, at the microscopic level. $RbNdNb_2O_7$ showcased a flake-like morphology with thin-shaped platelets averaging between 1 and $3\,\mu m$ in lateral size, while $RbNdTa_2O_7$ presented a more cauliflower-like nucleation and features with lateral sizes bellow $1\,\mu m$. With a Raman temperature study of the $RbNdNb_2O_7$, we were able to analyze the evolution of vibrational modes and confirm the $I2cm \rightarrow Cmca$ structural phase transition at $\sim 795\,K$.

In-depth structural analyses of bulk $RbNdNb_2O_7$ and $RbNdTa_2O_7$ indicate that the SOJT effect of B-site plays a critical role in governing octahedral distortions and A-site displacements. Nb^{5+} exhibits stronger SOJT effects than Ta^{5+}, leading to greater octahedral distortion and enhanced bond covalence, favoring a more stable polar phase evidenced by the higher polar to antipolar phase transition temperature in $RbNdNb_2O_7$. These structural differences were clearly identified by both XRD and Raman analyses, highlighting the interplay between local bonding environments and lattice dynamics.

The protonation of $RbNdNb_2O_7$ was successfully achieved, as the XRD pattern indicated a reduction in interlayer spacing, evaluated through the shift of the $[0\,0\,2]$ reflection peak. Although the exact fraction of Rb^+ replacement could not be quantified with absolute certainty, refinement results estimate an exchange of approximately 90%. In addition, no traces of Rb were found by the EDS scan, which further supports a successful ion exchange process. While the observed shift in the $[002]$ peak is smaller than those reported in literature, a more complete exchange should be achievable following a more rigorous process, namely with a more frequent acid renewal during the exchange reaction. Nevertheless, these results confirm the feasibility of protonation and provide a foundation for achieving H-ion exchange in related layered materials.

Finally, we explored the exfoliation possibility of the synthesized compounds following the ultrasonication technique, using the organic solvents N-Methyl-2-pyrrolidone and Tetrabutylammonium hydroxide. Raman and XRD measurements showed that N-Methyl-2-pyrrolidone does not intercalate into these materials (for $RbNdTa_2O_7$ at least), in contrast to Tetrabutylammonium hydroxide which exhibited intercalation behavior. The diffraction pattern obtained for the centrifugation residue from the ultrasonicated solution of Hex-$RbNdNb_2O_7$ in Tetrabutylammonium hydroxide, clearly indicates that stirring promotes the occupation of interlayer sites by TBA^+, thereby increasing the spacing between perovskite layers. SEM analysis showed that PEI treatment of the substrates had a surfactant effect on the exfoliated material. Lateral size of the exfoliated flakes identified from SEM was similar to what was observed for the parent powder, which is not expected for exfoliated forms of these materials. However, our light dispersion test showed a pronounced Tyndall effect, confirming the presence of exfoliated sheets in the supernatant solutions of both $RbNdTa_2O_7$ and $RbNdNb_2O_7$. Although our attempts did not yield fully conclusive evidence of successful exfoliation for both compounds, they provide several valuable insights for future optimization and also contribute meaningful observations to the existing literature about exfoliation studies on layered perovskites. Furthermore, the challenge still remains in this study to design and develop an efficient experimental strategy to catch or deposit the exfoliated sheets.

Overall, the experiments and findings from the exfoliation demonstrate the potential of chemical intercalation routes for exfoliating layered perovskites while identifying key challenges that must be addressed. A future approach for this work should follow a more rigorous approach with special focus on the deposition process, which appears to be the a key limiting factor. Our findings also highlighted several variables that strongly influence the exfoliation pathway. Factors such as the synthesis of the parent compounds, the selection of a suitable organic reagent, proper dispersion of the material, and the optimization of the ultrasonication procedure can all significantly affect the final outcome. Thus, it seems absolutely essential that all involved parameters are precisely controlled, and also that higher sensitivity techniques (such as Transmission Electron Microscopy) are necessary to provide more definitive assessments of exfoliation results.

References

[1] E. A. Katz, “Perovskite: Name puzzle and german-russian odyssey of discovery,” *Helvetica Chimica Acta*, vol. 103, no. 6, 2020. [Cited on page 1.]

[2] P. R. Rodrigues, “Functional lattice instabilities in naturally layered perovskites: from local probe studies to macroscopic cross-coupling effects,” PhD thesis, Faculdade de Ciências, Universidade do Porto, Porto, Portugal, 2021. [Cited on pages ix, 1, 2, 3, 8, 13, and 16.]

[3] N. Spaldin and R. Ramesh, “Advances in magnetoelectric multiferroics,” *Nature Materials*, vol. 18, no. 3, 2019. [Cited on pages 1 and 5.]

[4] N. Zhang, H. Yokota, Z. R. A.M. Glaze and, D. Keen, D. Keeble, P. Thomas, and Z. Ye, “The missing boundary in the phase diagram of $PbZr_{1-x}Ti_xO_3$,” *Nature Communications*, vol. 5, pp. 1–9, 2014. [Cited on page 1.]

[5] A. Lopes, J. Araújo, J. Ramasco, V. Amaral, R. Suryanarayananm, and J. Correia, “Percolative transition on ferromagnetic insulator manganites: Uncorrelated to correlated polaron clusters,” *Physical Review B*, vol. 73, no. 10, 2006. [Cited on page 1.]

[6] Y. Yang, Y. Sun, and Y. Jiang, “Structure and photocatalytic property of perovskite and perovskite-related compounds,” *Materials Chemistry and Physics*, vol. 96, no. 2, pp. 234–239, 2006. [Cited on page 1.]

[7] M. Lufaso and P. Woodward, “Prediction of the crystal structures of perovskites using the software program spuds,” *Acta Crystallographica Section B Structural Science*, vol. 57, no. 6, pp. 725–738, 2001. [Cited on page 1.]

[8] M. Johnsson and P. Lemmens, *Crystallography and Chemistry of Perovskites, in: Handbook of Magnetism and Advanced Magnetic Materials*. Chichester, UK: John Wiley Sons Ltd., 2007, vol. 262. [Cited on page 2.]

[9] V. M. Goldschmidt, “Die gesetze der krystallochemie,” *Die Naturwissenschaften*, vol. 14, no. 21, pp. 477–485, 1926. [Cited on page 2.]

[10] A. M. Glazer, “The classification of tilted octahedra in perovskites,” *Acta Crystallographica Section B: Structural Crystallography and Crystal Chemistry*, vol. 28, no. 11, pp. 3384–3392, 1972. [Cited on page 2.]

[11] P. A. Sousa, “Combined local probe and ab-initio study of dion-jacobson systems,” MSc thesis, Faculdade de Ciências, Universidade do Porto, Porto, Portugal, 2022. [Cited on pages ix, 3, 4, 6, and 18.]

[12] N. A. Benedek, J. Rondinelli, H. Djani, P. Ghosez, and P. Lightfoot, “Understanding ferroelectricity in layered perovskites: New idead and insights from theory and experiments,” *Dalton Transactions*, vol. 44, no. 23, 2015. [Cited on pages ix, 3, 4, and 5.]

[13] N. A. Benedek and C. J. Fennie, “Hybrid improper ferroelectricity: A mechanism for controllable polarization-magnetization switching,” *Physical Review Letters*, 2011. [Cited on page 3.]

[14] P. Ghosez and J. Triscone, “Coupling of three lattice instabiltities,” *Nature Materials*, vol. 10, no. 4, pp. 269–270, 2011. [Cited on pages ix and 4.]

[15] N. A. Benedek, “Origin of ferroelectricity in a family of polar oxides: The dion-jacobson phases,” *Inorganic Chemistry*, vol. 53, no. 7, pp. 3769–3777, 2014. [Cited on pages ix, 5, and 6.]

[16] V. Yadav, S. Pal, and S. Uma, “Dion-jacobson (n = 2) layered perovskites ($A'SmTa_2O_7$; A' = Rb, Cs) as potential ferroelectric materials,” *Journal of Physical Chemistry C*, vol. 129, pp. 5666–5673, 2025. [Cited on page 5.]

[17] B. Zhang, X. Liu, and X. Chen, “Review of experimental progress of hybrid improper ferroelectricity in layered perovskite oxides,” *Journal of Physics D: Applied Physics*, vol. 55, no. 11, 2022. [Cited on page 6.]

[18] T. Zhu, A. Gibbs, N. Benedek, and M. Hayward, “Complex structural phase transitions of the hybrid improper polar dion-jacobson oxides $RbNdM_2O_7$ and $CsNdM_2O_7$ ($M = Nb, Ta$),” *Chemistry of Materials*, vol. 32, no. 10, pp. 4340–4346, 2020. [Cited on pages ix, x, 6, 7, 10, 14, 18, 23, 24, 26, 27, 29, 34, and 37.]

[19] T. Zhu, T. Cohen, A. Gibbs, W. Zhang, and P. Halasyamani, “Theory and neutrons combine to reveal a family of layered perovskites without inversion symmetry,” *Chemistry of Materials*, vol. 29, no. 21, pp. 9489–9497, 2017. [Cited on pages ix, 6, and 8.]

[20] N. Benedek and M. Hayward, "Hybrid improper ferroelectricity: A theorectical, computational, aand synthetic perspective," *Annual Review of Materials Research*, vol. 52, pp. 331–355, 2022. [Cited on pages ix, 7, and 8.]

[21] Z.-T. Lu, S. Asaki, S. Yoshida, C. Moriyoshi, G. Hasegawa, K. Fujita, V. Gopalan, K. Hayashi, and H. Akamatsu, "Structural frustration effects by mixed alkali ions in ferroelectric dion–jacobson layered perovskites $(Cs, Rb)NdNb_2O_7$," *Journal of Materials Chemistry*, vol. 13, pp. 1812–1823, 2025. [Cited on page 7.]

[22] Z.-T. Lu, K. Nishioka, Y. Zhang, K. Fujita, K. Hayashi, and H. Akamatsu, "Suppression of ferroelectric transitions by symmetry trapping in dion-jacobson-layered perovskites $Cs(La, Nd)Nb_2O_7$," *Inorganic Chemistry*, vol. 63, p. 23914–23925, 2024. [Cited on page 7.]

[23] R. Hinterding and A. Feldhoff, "Two-dimensional oxides: Recent progress in nanosheets," *Zeitschrift für Physikalische Chemie*, vol. 233, no. 1, pp. 117–165, 2018. [Cited on page 8.]

[24] A. Takagaki, C. Tagusagawa, S. Hayashi, M. Hara, and K. Domen, "Nanosheets as highly active solid acid catalysts for green chemical synthesis," *Energy Environamental Science*, vol. 3, no. 1, pp. 82–93, 2010. [Cited on page 8.]

[25] B. Zhang, Y. Li, J. Luo, H. Zhao, J. Zhao, G. Dong, Y. Zhu, and C. Wang, "Synthesis and photocatalytic property for h2 production for $H_{1.78}Sr_{0.78}Bi_{0.22}Nb_2O_7$ nanosheets," *Applied Surface Science*, vol. 391, pp. 499–506, 2016.

[26] W. Xiong, H. Porwal, H. Luo, V. Araullo-Peters, J. Feng, M. Titirici, M. Reece, and J. Briscoe, "Photocatalytic activity of 2d nanosheets of ferroelectric dion-jacobson compounds," *Journal of Materials Chemistry A*, vol. 8, 2020. [Cited on pages 9, 10, and 15.]

[27] H. Zhang, Y. Wang, W. Niu, T. Yoskamtorn, M. Luo, R. Tayler, S. Day, and S. Tsang, "Tuning 2d perovskite-graphene layered composite for photocatalysis," *Sustainable Energy Fuels*, vol. 8, 2024. [Cited on pages 8, 14, 15, and 45.]

[28] T. Le, C. Chang, and Y. Su, "Hydrogen generation ability of b-site substituted two-dimensional $Ca_{n-1}Ti_{n-3}Nb_3O_{3n+1}$ perovskite nanosheets in photoelectrochemical cells," *Surfaces and Interfaces*, vol. 36, no. 17, 2023. [Cited on page 8.]

[29] A. Takagaki, C. Tagusagawa, S. Hayashi, M. Hara, and K. Domen, "Nanosheets as highly active solid acid catalysts for green chemical synthesis," *Journal of Materials Chemistry*, vol. 19, no. 17, pp. 2503–2511, 2009. [Cited on page 8.]

[30] T. Taniguchi, L. Nurdiwijayanto, and R. Ma, "Chemically exfoliated inorganic nanosheets for nanoelectronics," *Applied Physics Reviews*, vol. 9, 2022. [Cited on pages 8 and 9.]

[31] A. Burovikhina, I. Rodionov, M. Chislov, D. Porotnikov, and I. Zvereva, "Photocatalytic activity of layered niobates $ANdNb_2O_7$ (A = H, Li, Na, Rb, Cs)," *International Journal of Nanotechnology*, vol. 13, pp. 4813–4818, 2016. [Cited on pages 8 and 14.]

[32] M. S. Khan, "Layer-by-layer assembly of pervoskite nanosheets and its applications to electronic materials," PhD thesis, Graduate School of Advance Science and Engineering, Waseda University, Shinjuku, Japan, 2017. [Cited on page 8.]

[33] K. Maeda and T. Mallouk, "Two-dimensional metal oxide nanosheets as building blocks for artificial photosynthetic assemblies," *Bulletin of the Chemical Society of Japan*, vol. 92, 2018. [Cited on page 9.]

[34] E. Varrla, C. Backes, K. Paton, A. Harvey, Z. Gholamvand, J. McCauley, and J. Coleman, "Large-scale production of size-controlled MoS_2 nanosheets by sheer exfoliation," *Chemistry of Materials*, vol. 27, pp. 1129–1139, 2015. [Cited on pages ix and 9.]

[35] R. Uppuluri, A. Gupta, A. Rosas, and T. Mallouk, "Soft chemistry of ion-exchangeable layered metal oxides," *Chemical Society Reviews*, vol. 47, pp. 2401–2430, 2018. [Cited on pages 9, 10, and 14.]

[36] R. Ma and T. Sasaki, "Two-dimensional oxide and hydroxide nanosheets: Controllable high-quality exfoliation, molecular assembly, and exploration of functionality," *Accounts of Chemical Research*, vol. 48, pp. 136–143, 2015. [Cited on pages ix and 10.]

[37] T. Maluangnont, K. Matsuba, F. Geng, R. Ma, Y. Yamauchi, and T. Sasaki, "Osmotic swelling of layered compounds as a route to producing high-quality two-dimensional materials. a comparative study of tetramethylammonium versus tetrabutylammonium cation in a lepidocrocite-type titanate," *Chemistry of Materials*, vol. 25, pp. 3137–3146, 2013. [Cited on pages 9 and 10.]

[38] T. Sasaki and M. Watanabe, “Osmotic swelling to exfoliation. exceptionally high degrees of hydration of a layered titanate,” *Journal of the American Chemical Society*, vol. 120, pp. 4682–4689, 1998. [Cited on pages 10 and 57.]

[39] S. Kurnosenko, I. Minich, O. Silyukov, and I. Zvereva, “Highly efficient liquid-phase exfoliation of layered perovskite-like titanites $HLnTiO_4$ and $H_2Ln_2Ti_3O_10$ (Ln = La, Nd) into nanosheets,” *Nanomaterials*, vol. 13, 2023. [Cited on pages 10, 15, and 49.]

[40] I. Minich, O. Silyukov, S. Kurnosenko, V. Gak, V. Kalganov, P. Kolonitskiy, and I. Zvereva, “Physical–chemical exfoliation of n-alkylamine derivatives of layered perovskite-like oxide h2k0.5bi2.5ti4o13 into nanosheets,” *Nanomaterials*, vol. 11, 2021. [Cited on page 10.]

[41] A. R. West, *Solid State Chemistry and its Applications, 2nd Edition*. John Wiley & Sons Ltd., 2014. [Cited on page 13.]

[42] K. Maeda and T. E. Mallouk, “Comparison of two- and three-layer restacked dion-jacobson phase niobate nanosheets as catalyts for photochemical hydrogen evolution,” *Journal of Materials Chemistry*, vol. 19, pp. 4813–4818, 2009. [Cited on pages 14 and 15.]

[43] V. Pecharsky and P. Zavalij, *Fundamentals of Powder Diffraction and Structural Characterization of Materials, 2nd Edition*. New York, USA: Springer US, 2009. [Cited on pages 15 and 16.]

[44] H. Bragg and L. Bragg, “The reflection of x-rays by crystals,” *Proceedings of the Royal Society A: Mathematical, Physical and Engineering Sciences*, 1913. [Cited on page 15.]

[45] Rigaku Holdings Corporation and its Global Subsidiaries, “X-Ray Diffraction,” (booklet). [Cited on pages ix and 16.]

[46] H. Rietveld, “Line profiles of neutron powder-difffraction peaks for structure refinement,” *Acta Crystallographica*, vol. 22, pp. 151–152, 1967. [Cited on page 17.]

[47] N. Döbelin and R. Kleeberg, “Profex: a graphical user intefacer for the rietveld refinement program bgmn,” *Journal of Applied Crystallography*, vol. 48, pp. 1573–1580, 1967. [Cited on pages 18 and 25.]

[48] P. Vandenabeele, *Practical Raman Spectroscopy - An Introduction*. John Wiley & Sons, Ltd, 2013. [Cited on pages 18 and 19.]

[49] K. Krishnan and C. Raman, "The negative absorption of radiation," *Nature*, vol. 122, pp. 12–13, 1928. [Cited on page 18.]

[50] Hitcachi High-Tech Corporation, *The Scanning Electron Microscopy Guide: From sample preparation to imaging*, (manual). [Cited on page 19.]

[51] B. Inkson, *Materials Characterization Using Nondestructive Evaluation (NDE) Methods*. Woodhead Publishing, 2016. [Cited on pages ix and 20.]

[52] S. Stephen, S. Sherman, and R. Averiff, "Heat Capacity of Fe_3O_4 (Magnetite)," Quantum Design Educational Module. [Cited on pages ix, 20, and 21.]

[53] J. Hwang, K. Lin, and C. Tien, "Measuremnt of heat capacity by fitting the whole temperature response of a heat-pulse calorimeter," *Review of Scientific Instruments*, vol. 68, pp. 94–101, 1997. [Cited on page 20.]

[54] N. Lekshmi, E. Silva, P. Rodrigues, J. Evans, J. Belo, P. Sousa, A. Manjon-Sanz, A. Santos, A. Lopes, and J. Araújo, "Structural distortions and uniaxial negative thermal expansion in the polar dion−jacobson oxide $RbNdTa_2O_7$," *Chemistry of Materials*, vol. 37, pp. 5529–5546, 2025. [Cited on pages 29, 34, and 36.]

[55] G. Blasse, "Qualitative approach to the structural differences between some mixed metal oxides containing $Sb5+$, $Nb5+$ and $Ta5+$," *Journal of Inorganic and Nuclear Chemistry*, vol. 26, pp. 1191–1199, 1964. [Cited on page 30.]

[56] T. Grivois, T. Salkus, V. K. J. Yu, P. Janolin, S. Daugela, F. Goutenoire, A. Rousseau, and M. Barre, "Lanthanides disorder in tantalates and niobates perovskites: structure and electric properties," *Ceramics International*, vol. 51, p. 51790–51802, 2025. [Cited on page 32.]

[57] M. Drulis and K. Konieczny, "Low-temperature heat capacity of $NaNbO_3$ compound," *Materials Science and Engineering B*, vol. 72, pp. 19–22, 2000. [Cited on page 41.]

[58] V. Anand, D. Tennant, and B. Lake, "Investigations of the effect of nonmagnetic ca substitution for magnetic dy on spin-freezing in dy2ti2o7," *Journal of Physics: COndensed Matter*, vol. 27, pp. 19–22, 2015. [Cited on page 41.]

[59] S. Lal, K. Mukherjee, and C. Yadav, "Effect of crystalline electric field on heat capacity of $LnBaCuFeO5$ ($Ln = Gd, Ho, Yb$)," *Solid State Communications*, vol. 270, pp. 130–134, 2018. [Cited on page 41.]

[60] A. Scheie, M. Sanders, X. Gui, Y. Qiu, T. Prisk, R. Cava, and C. Broholm, "Beyond magnons in Nd_2ScNbO_7 : An ising pyrochlore antiferromagnet with all-in–all-out order and random fields," *Physical Review B*, vol. 104, 2021. [Cited on page 41.]

[61] W. Lee, H. Yeo, D. Kim, S. Paek, and Y. Kim, "Exfoliation of dion-jacobson layered perovskite into macromolecular nanoplatelet," *Bulletin of the Korean Chemical Society*, vol. 34, 2013. [Cited on page 51.]

[62] Y. Shi, M. Osada, Y. Ebina, and T. Sasaki, "Single droplet assembly for two-dimensional nanosheet tiling," *ACS Nano*, vol. 14, pp. 15 216–15 226, 2020. [Cited on page 60.]

A. Supporting Information

A.1. Raman Temperature Study

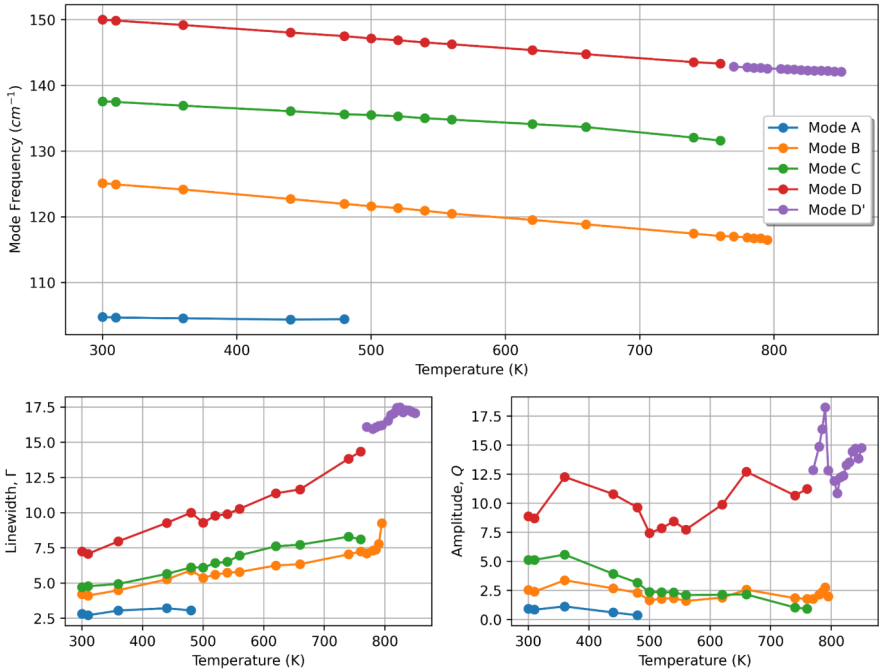

Figure A.1: Fit parameters (frequency, linewidth and amplitude) of selected peaks in the $[100\,;175]\ cm^{-1}$ region.

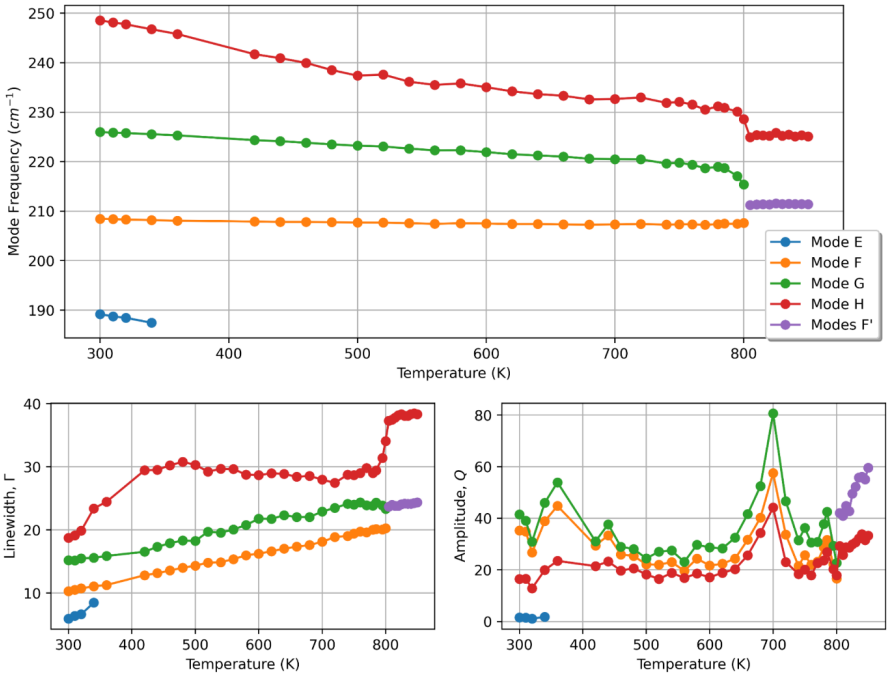

Figure A.2: Fit parameters (frequency, linewidth and amplitude) of selected peaks in the $[170\,;280]\ cm^{-1}$ region.

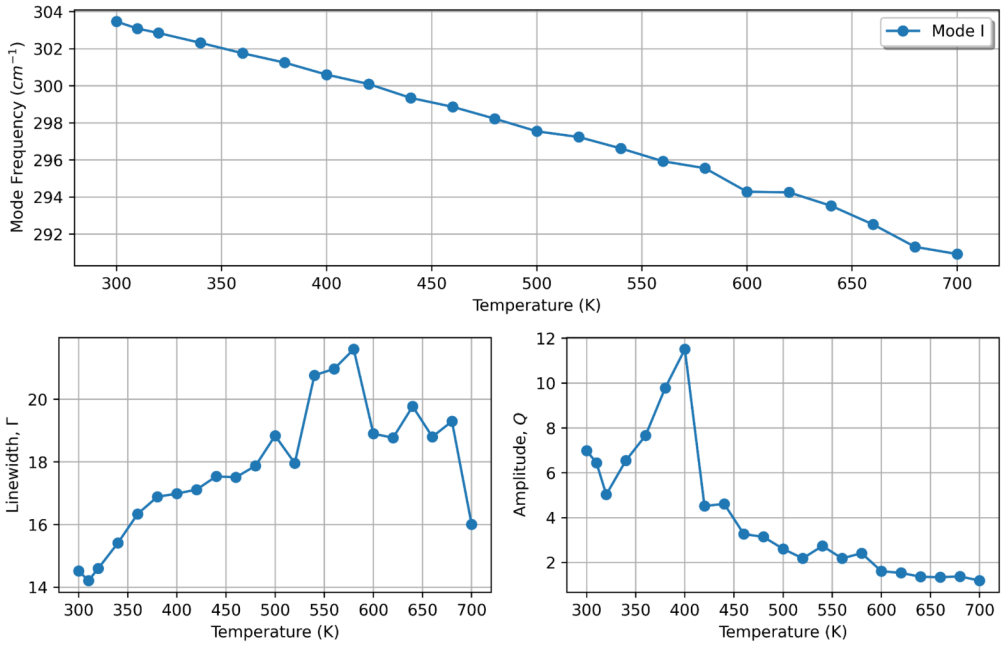

Figure A.3: Fit parameters (frequency, linewidth and amplitude) of selected peaks in the $[270\,;315]\ cm^{-1}$ region.

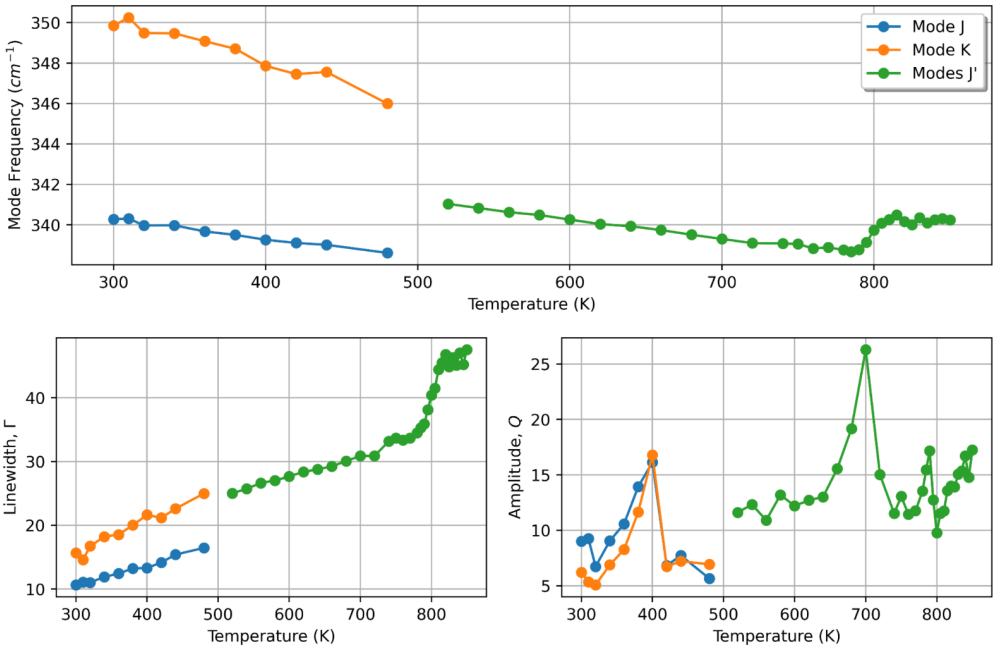

Figure A.4: Fit parameters (frequency, linewidth and amplitude) of selected peaks in the $[300\,;380]\ cm^{-1}$ region.

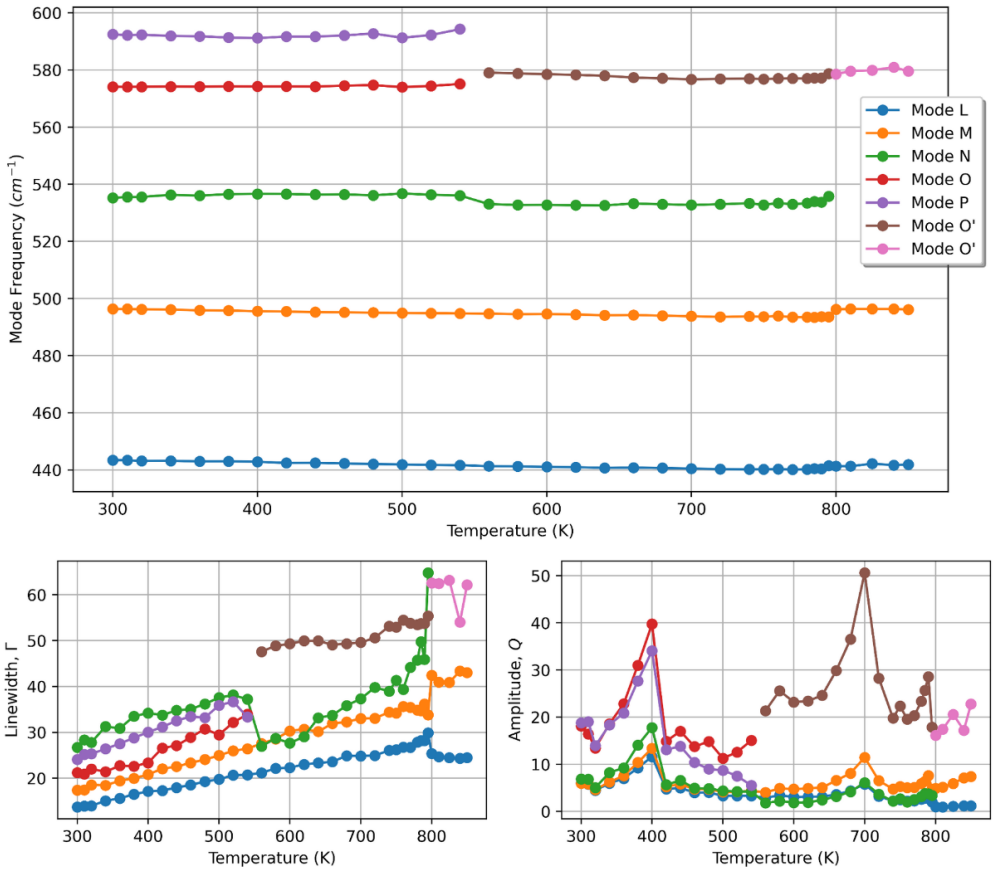

Figure A.5: Fit parameters (frequency, linewidth and amplitude) of selected peaks in the $[400\,;660]\ cm^{-1}$ region.

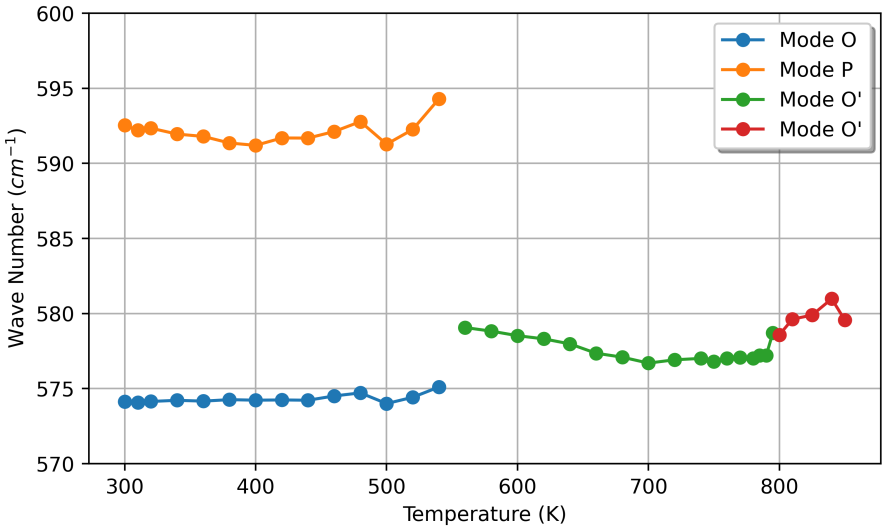

Figure A.6: Drift of the O, P and O' vibrational mode frequencies across the temperature range.

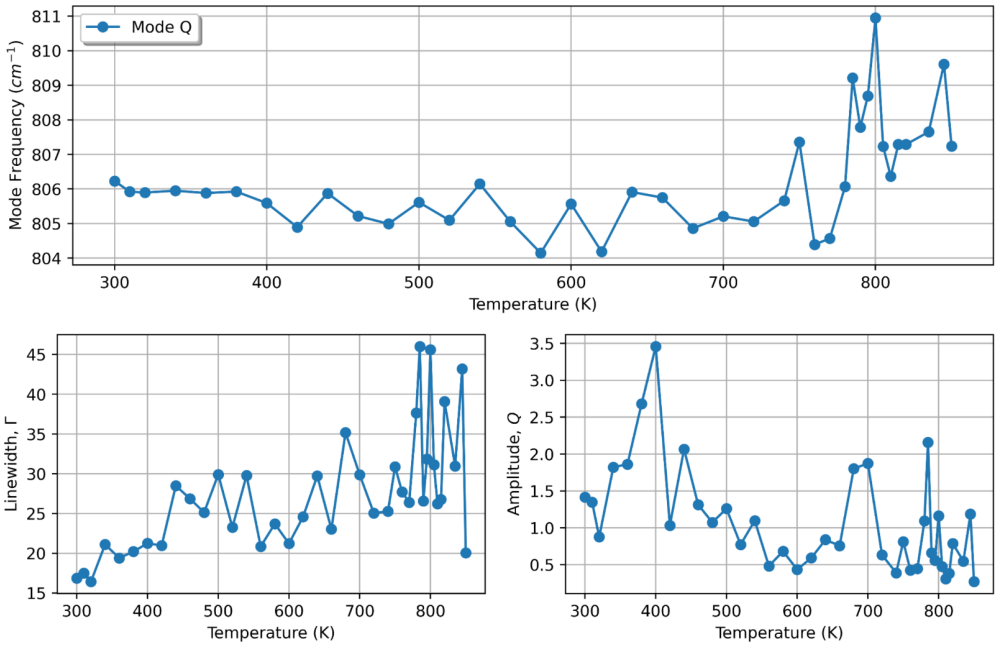

Figure A.7: Fit parameters (frequency, linewidth and amplitude) of selected peaks in the $[790\,;820]\ cm^{-1}$ region.

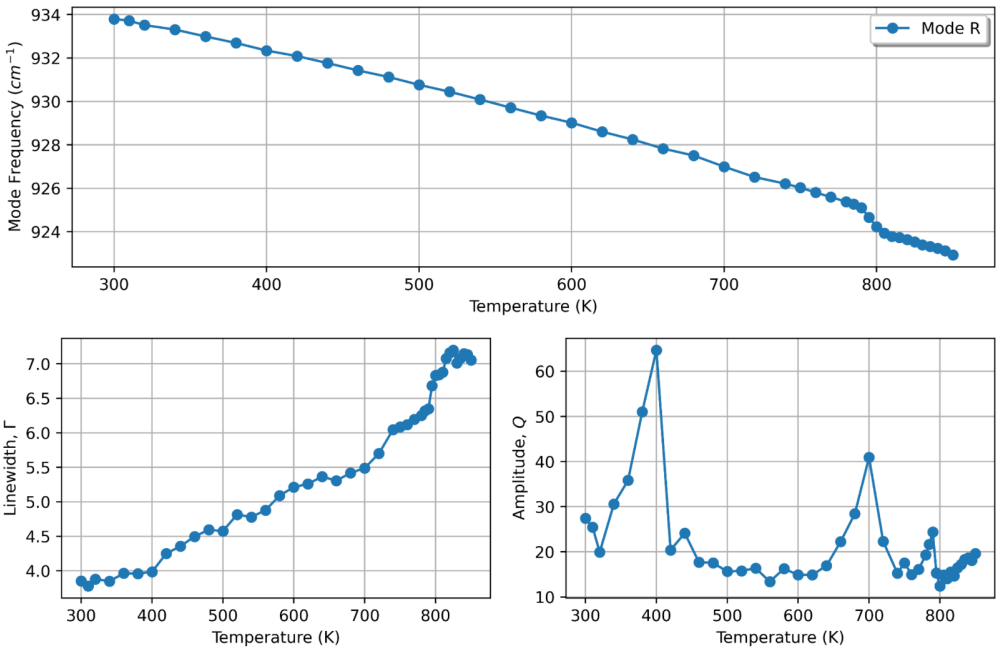

Figure A.8: Fit parameters (frequency, linewidth and amplitude) of selected peaks in the $[900\,;955]\ cm^{-1}$ region.